Compressed Sensing for Open-ended Waveguide Non-Destructive Testing and Evaluation

A thesis submitted for the degree of Doctor of Philosophy

Chaoqing Tang

Intelligent Sensing and Communications Research Group (ISC)
School of Engineering, Newcastle University

October 2019

Abstract

Non-destructive testing and evaluation (NDT&E) systems using open-ended waveguide (OEW) suffer from critical challenges. In the sensing stage, data acquisition is time-consuming by raster scan, which is difficult for on-line detection. Sensing stage also disregards demand for the latter feature extraction process, leading to an excessive amount of data and processing overhead for feature extraction. In the feature extraction stage, efficient and robust defect region segmentation in the obtained image is challenging for a complex image background. Compressed sensing (CS) demonstrates impressive data compression ability in various applications using sparse models. How to develop CS models in OEW NDT&E that jointly consider sensing & processing for fast data acquisition, data compression, efficient and robust feature extraction is remaining challenges.

This thesis develops integrated sensing-processing CS models to address the drawbacks in OEW NDT systems and carries out their case studies in low-energy impact damage detection for carbon fibre reinforced plastics (CFRP) materials. The major contributions are:

(1) For the challenge of fast data acquisition, an online CS model is developed to offer faster data acquisition and reduce data amount without any hardware modification. The images obtained with OEW are usually smooth which can be sparsely represented with discrete cosine transform (DCT) basis. Based on this information, a customised 0/1 Bernoulli matrix for CS measurement is designed for downsampling. The full data is reconstructed with orthogonal matching pursuit algorithm using the downsampling data, DCT basis, and the customised 0/1 Bernoulli matrix. It is hard to determine the sampling pixel numbers for sparse reconstruction when lacking training data, to address this issue, an accumulated sampling and recovery process is developed in this CS model. The defect region can be extracted with the proposed histogram threshold edge detection (HTED) algorithm after each recovery, which forms an online process. A case study in impact damage detection on CFRP materials is carried out for validation. The results show that the data acquisition time is reduced by one order of magnitude while maintaining equivalent image quality and defect region as raster scan.

(2) For the challenge of efficient data compression that considers the later feature extraction, a feature-supervised CS data acquisition method is proposed and evaluated. It reserves interested

features while reducing the data amount. The frequencies which reveal the feature only occupy a small part of the frequency band, this method finds these sparse frequency range firstly to supervise the later sampling process. Subsequently, based on joint sparsity of neighbour frame and the extracted frequency band, an aligned spatial-spectrum sampling scheme is proposed. The scheme only samples interested frequency range for required features by using a customised 0/1 Bernoulli measurement matrix. The interested spectral-spatial data are reconstructed jointly, which has much faster speed than frame-by-frame methods. The proposed feature-supervised CS data acquisition is implemented and compared with raster scan and the traditional CS reconstruction in impact damage detection on CFRP materials. The results show that the data amount is reduced greatly without compromising feature quality, and the gain in reconstruction speed is improved linearly with the number of measurements.

(3) Based on the above CS-based data acquisition methods, CS models are developed to directly detect defect from CS data rather than using the reconstructed full spatial data. This method is robust to texture background and more time-efficient that HTED algorithm. Firstly, based on the histogram is invariant to down-sampling using the customised 0/1 Bernoulli measurement matrix, a qualitative method which only gives binary judgement of defect is developed. High probability of detection and accuracy is achieved compared to other methods. Secondly, a new greedy algorithm of sparse orthogonal matching pursuit (spOMP)-based defect region segmentation method is developed to quantitatively extract the defect region, because the conventional sparse reconstruction algorithms cannot properly use the sparse character of correlation between the measurement matrix and CS data. The proposed algorithms are faster and more robust to interference than other algorithms.

CERTIFICATE OF ORIGINALITY

This is to certify that all the works submitted in this thesis are my own works except as specified in acknowledgements. Neither the work nor the thesis has been submitted to any other institution for another degree. I am responsible for all the works in this thesis.

Chaoqing Tang .(Signed)

Chaoqing Tang .(Candidate)

Acknowledgements

It is a truly life-changing experience for me to pursuit this PhD degree, and it would not have been possible without the support and guidance that I received from many people.

Firstly, I would like to express my sincere gratitude to my supervisors, Prof. Gui Yun Tian, Prof. Said Boussakta, and Dr Martin Johnston for the continuous support of my PhD study. I learnt a lot from Prof. Gui Yun Tian, who puts substantial efforts in inspiring my thinking. He plants a seed of philosophy for problem-solving in me and shapes my value to academic research. Research is not about publishing how many papers, but about solving scientific and engineering challenges that lead to a better living standard. A good ecosystem between academic research and industry is of mutual benefits for both sides. He shows me an attitude of persisting in high-quality works and never compromising it to other constraints. I believe these characters will drive me to a fruitful future.

My sincere thanks also goes to my colleagues who stimulate my research idea and helps me improve presentation skills during discussion, including academic visitors Dr. Jianbo Wu, Mr. Huadong Song, Dr. Mengbao Fan, Dr. Shaohua Hong, Dr. Song Ding, research associates Dr. Jun Zhang, Dr. Malindar, Dr. Feng Liu and PhD students Dr. Kongjing Li, Dr. Ali Sunny, Mr. Ruslee Sutthaweekul， Mr. Mohammed Buhari, Mr. Junzhen Zhu, Mr. Quiji Yi, Mr. Denis Ona, et al. I would also like to thank all the staff and the technicians of Newcastle University for their support. Thanks to all the friends I met during my PhD study who give me a happy memory and help me release my study pressure.

I must express my gratitude to my beloved parents and my girlfriend Lin Lin who stand with me in whatever cases and give me motivation, encouragement and care. My sincerely thanks also go to friends who help with proofreading, and examiners who give comments to help improving the quality of this thesis.

Last but not least, I would like to thank my PhD sponsor China Scholarship Council to partially support my PhD study financially.

Table of Contents

List of Figures

List of Tables

List of Publications

Journal papers:

[1] **C. Tang**, G. Y. Tian, K. Li, R. Sutthaweekul, and J. Wu, "Smart Compressed Sensing for Online Evaluation of CFRP Structure Integrity," *IEEE Transactions on Industrial Electronics,* vol. 64, no. 12, pp. 9608-9617, 2017.

[2] **C. Tang**, G. Y. Tian, S. Boussakta, J. Wu, "Feature-supervised Compressed Sensing for Microwave Imaging Systems," submitted to *IEEE Transactions on Instrumentation and Measurement.*

[3] **C. Tang**, H. F. Rashvand, G. Y. Tian, *et al.*, *Structural Health Monitoring with WSNs*. In *Wireless Sensor Systems for Extreme Environments,* 1st ed.; Habibi F. Rashvand, Ali Abedi; Wiley: 2017.

[4] **C. Tang**, G. Y. Tian, X. Chen, J. Wu, K. Li and H. Meng, "Infrared and Visible Images Registration with Adaptable Local-Global Feature Integration for Rail Inspection," *Infrared Physics & Technology* 87 (2017): 31-39.

[5] **C Tang**, G. Y. Tian, J. Wu, and Y. Ran, "Concurrent Physical Layer Encryption and Authentication using Compressed Sensing," submitted to *IEEE Transactions on Information Forensics and Security*.

[6] K. Li, G. Y. Tian, X. Chen, **C. Tang**, *et al.*, "AR aided Smart Sensing for In-line Condition Monitoring of IGBT Power Semiconductor Wafer," *IEEE Transactions on Industrial Electronics*, vol. 66, no. 10, 8197-8204, 2019.

[7] A. I. Sunny, J. Zhang, G. Y. Tian, **C. Tang**, *et al.*, "Temperature Independent Defect Monitoring using RFID Sensing System," *IEEE Sensor Journal*, vol. 19, no. 4, pp. 1525-1532, 2019.

Conference presentations:

[8] **C Tang**, G. Y. Tian, "Feature Extraction from Compressed Measurement in Waveguide Imaging Systems," the 23rd International Workshop on Electromagnetic Nondestructive Evaluation, Michigan, USA, 2018.

[9] **C Tang**, G. Y. Tian, "Metallic crack diagnostics with compressed sensing-based metamaterials," 2018 Far East NDT New Technology & Application Forum (FENDT), Xiamen, China, 2018.

Abbreviations

ADM	Alternating Direction Method
AI	Artificial Intelligence
ASSS	Aligned Spatial-Spectral Sensing
BCS	Bayesian Compressed Sensing
BP	Belief Propagation
CBM	Condition Based Maintenance
CFRP	Carbon Fibre Reinforced Plastics
CoSaOMP	Compressed Sensing Orthogonal Matching Pursuit
CS	Compressed Sensing
DCT	Discrete Cosine Transform
DDFS	Direct Digital Frequency Synthesizer
DNN	Deep Neural Network
DWT	Discrete Wavelet Transform
EEG	Electroencephalogram
ELC	Electric-Field-Coupled
FDTD	Finite-Difference Time-Domain
FsCS	Feature-Supervised Compressed Sensing
gOMP	Generalised Orthogonal Matching Pursuit
HTED	Histogram Threshold Edge Detection
HTP	Hard Thresholding Pursuit
IHT	Iterative Hard Thresholding
MAP	Maximum A Posteriori
MIP	Mutual Incoherence Property
MLE	Maximum Likelihood Estimate
MP	Matching Pursuit
MRI	Magnetic Resonance Imaging
NDT	Non-Destructive Testing
NDT&E	Non-Destructive Testing And Evaluation
NRMSE	Normalised Root Mean Square Error
OMP	Orthogonal Matching Pursuit

OEW	Open-ended Waveguide
ORWG	Open-Ended Rectangular Waveguide
PCA	Principal Component Analysis
RC	Random Convolution
RD	Random Demodulator
RF	Radio Frequency
RIP	Restricted Isometry Property
RLS-DLA	Recursive Least Squares Dictionary Learning Algorithm
RVM	Relevance Vector Machine
SAR	Synthetic Aperture Radar
SLM	Spatial Light Modulator
SP	Subspace Pursuit
spOMP	Sparse Orthogonal Matching Pursuit
SRM	Structurally Random Matrices
stOMP	Stagewise Orthogonal Matching Pursuit
SUT	Specimen Under Test
SVD	Singular-Value Decomposition
VNA	Vector Network Analyser

Key Notations

$\|\mathbf{x}\|_{\ell p}$	ℓ_p -norm for $\mathbf{x}$
$\|\mathbf{X}\|_{\ell p,q}$	Imposing ℓ_p -norm on each column of **X**, then ℓ_q -norm on each row of **X**
$\lvert x \rvert$	Absolute value of x
$\lfloor x \rfloor$	Flooring to get integer
$[x]$	Rounding to get integer
$[\mathbf{x}_i]_{i=1}^{N}$	Concatenating $\mathbf{x}_i$, where i = 1, 2, 3, …, N.
$\{x_i\}_{i=1}^{N}$	x_i, where i = 1, 2, 3, …, N.
$\langle \mathbf{x}, \mathbf{y} \rangle$	Inner product of **x** and **y**.
$\mathbf{X}^T$	Transpose of matrix **X**
$A \cup B$	Union of set A and B

Chapter 1. Introduction

This chapter briefly introduces the research background and motivations, defines the research scope, and highlighting the main contributions of this thesis. The thesis layout is also summarised.

1.1 Background and Motivation

Sensing technologies convert the physical world into a computable digitalised world. The digitalised data is convenient for storage, transmission and processing. However, the excessive scale of data from sensors brings challenges to extracting information that supporting decision-making. It also brings a heavy burden to transmission and storage. For example, 26 sensor arrays were used on the monitoring of Vincent Thomas Bridge in San Pedro California, generating 3TB of data per year [1]. 720P HD video camera at one engineering quality supervision site generates more than 2TB data per month. Extracting information for decision-making from such amount of data is challenging for ordinary computers. Extracting information from data is an important supporting technique for the Internet of Things and Industry 4.0 era. Despite the computation ability keeps improving with technologies like Cloud Computing and supercomputers, the more critical points are to understand first, what information is necessary to operate and compete; and second, how this information is sensed and applied, as mentioned in a workshop report 'The Future Directions Workshop on Compressed Sensing and the Integration of Sensing and Processing' in 2016 [2].

As an important enabling technology to give quality or health information in the quality management of Industry 4.0 era, non-destructive testing (NDT) technology also needs to efficiently manipulate between data and information. NDT is the process of inspecting, testing, or evaluating materials, components or assemblies for discontinuities, or differences in characteristics without destroying the serviceability of the part or system. Modern NDTs are used in manufacturing, fabrication and in-service inspections to ensure product integrity and reliability, to control manufacturing processes, lower production costs and to maintain a uniform quality level. During construction, NDT is used to ensure the quality of materials and joining processes during the fabrication and erection phases, and in-service NDT inspections are used to ensure that the products in use continue to have the integrity necessary to ensure their usefulness and the safety of the public.

Today, most NDT technologies are in an on-platform test model. On-platform means the object under test is forced to stop service and been tested on professional testing platforms. For example, periodically, some power plants are shut down for inspection. Inspectors feed eddy current probes into heat exchanger tubes to check for corrosion damage. The current business model for NDT inspection services is increasingly coming under threat. Shifting from the on-platform test model into in-service condition-based maintenance (CBM) is more economically efficient in the value chain of the maintenance-as-a-service business ecosystem [3, 4]. As shown in Figure 1.1, the next generation of NDT services needs to transition from just on-platform inspection to predictive maintenance advice delivered from a remotely located office. The office is supported by technologies like edge computing, cloud computing, big data, artificial intelligence, etc. Continuous and time-efficient measurements are made from deployed on-site inspection devices, the monitoring data are delivered to the monitoring centre with support such as 5G. Maintenance teams carry out maintenance service following the guidance of monitoring centre. One major realm of CBM is finding features that reflect the current health state of the asset or component under observation. Most of the existing NDT approaches are accompanied by high data volume and high computational costs during the different feature processing phases, making them infeasible in an on-site CBM scenario. Developing smart sensing technologies that efficiently support the information-based decision by integrating sensing and processing as one unit is increasingly important for current NDT technologies [2].

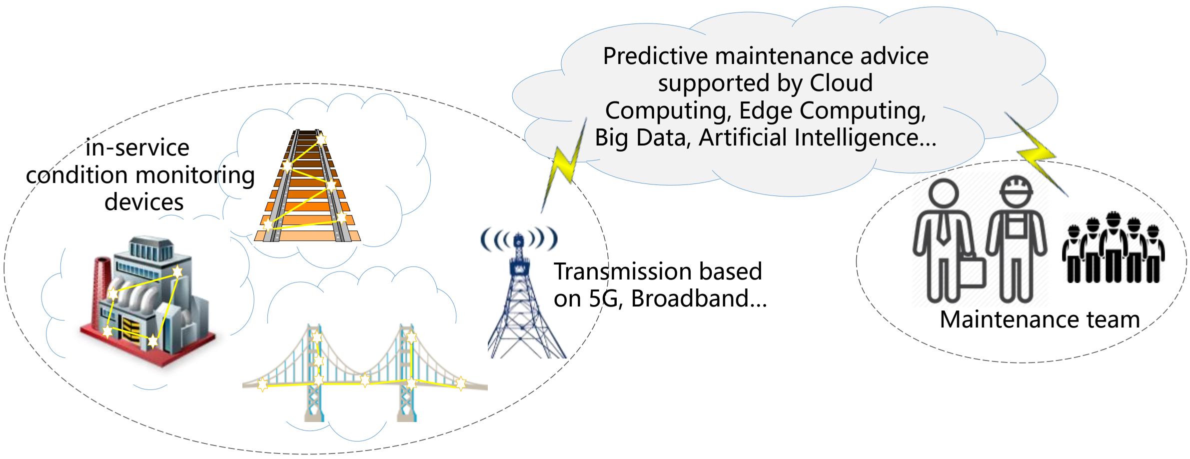

Figure 1.1 Maintenance-as-a-service in Industry 4.0

Sensing techniques is the front-end of NDT. Various physical parameters can be used for NDT. NDT techniques that based on sound and vibration are: acoustic emission testing (AE), guided wave testing (GW), ultrasonic testing (UT), vibration analysis (VA); visible light such as visual testing (VT); electromagnetic wave such as electromagnetic testing (ET), ground penetrating radar (GPR), microwave testing, radiographic testing (RT); magnetics such as magnetic flux leakage (MFL), magnetic particle testing (MT); and laser testing methods (LM) for laser, thermal/infrared testing (IR) for temperature, etc. Due to their basic principles, these NDT techniques show various characters in suitable testing materials, detection depth and resolution. The table below [5] presents a brief summary of the characters of some commonly used techniques.

Table 1.1 Character of commonly used NDT techniques

Techniques	Capabilities	Limitations
Visual inspection	Macroscopic surface flaws	small flaws are difficult to detect, no subsurface flaws
Microscopy	Small surface flaws	not applicable to large structures, no subsurface flaws
Radiography	subsurface flaws	Smallest detectable defect is 2% of the thickness, radiation protection. No subsurface flaws not for porous materials
Dye penetrate	surface flaws	No subsurface flaws not for porous materials
Ultrasonic	subsurface flaws	material must be a good conductor of sound
Magnetic particle	surface/near surface and layer flaws	limited subsurface capability, only for ferromagnetic materials
Eddy current	subsurface and near subsurface flaws	difficult to interpret in some application, only for metals
Acoustic emission	entire structure	difficult to interpret, expensive equipments

Open-ended Waveguide (OEW) testing is using open-ended waveguide to emit and receive microwaves based on near-field radio frequency (RF) reflectivity. It has advantages over others like contactless measurement, high resolution, and safe for human. Figure 1.2 shows the overall principle. The specimen under test (SUT) is illuminated by microwave or millimetre wave with a waveguide probe. The scanner carries a waveguide probe to scan the SUT using a raster scan of a spatial area with a step size. When the step size for raster scan in X and Y direction becomes small, there is no much difference between nearby measurement results while the measurement time is increasing significantly. A sub-millimetre level step size is enough for defect detection as recommended in [6]. The complex reflection coefficient (S11 parameter) is measured by microwave sensors [7] or vector network analyser with frequency sweep. This reflection coefficients carry the material property information such as magnetic permeability (μ), electric permittivity (ε) and electrical conductivity (σ) of SUT. Since defects change the local material property which results in the change of local reflectivity, the whole spatial reflection image of the S11 parameter will reveal the defect pattern caused by the defect. From the frequency point of view, the spatial image for different frequency frames is usually different due to the complex internal structure of SUT such as composite materials and skin effect. The complex internal structure interacts with the excitation signal in the form of reflection, transmission, scattering, and absorption etc. The skin effect constrains deep defect detection capability for all electromagnetic wave-based techniques. Estimation of skin depth is necessary to access how deep a sub-surface defect can reveal in theory. For a given frequency (f), the skin depth (δ) is determined by:

$$\delta = \frac{1}{\sqrt{\pi f \mu \sigma}} \tag{1.1}$$

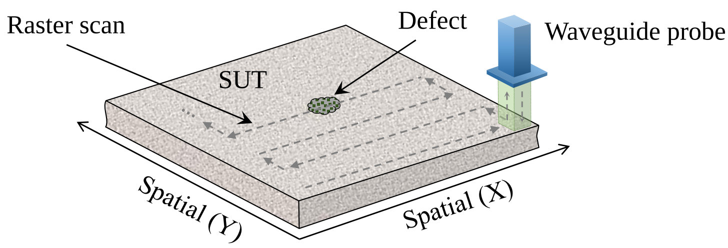

Figure 1.2 Open-ended Waveguide NDT

OEW NDT systems also meet challenges to thrive in the new CBM business ecosystem. Figure 1.3 summarises some challenges. The most significant drawback is the time-consuming data acquisition by raster scan. For example, scanning a 30*mm*×30*mm* area with 0.3*mm* of step size and 1601 frequency sweep points takes around 3 hours, leading to more than 300MB of data. Smaller stepsize greatly increases the scanning time as the sampling data and time increase linearly with the number of sampling points. The massive data amount is challenging for transmission and storage; it is also challenging for processing because feature extraction is performed in post-processing steps on the bulky data. The feature extraction calls for much expert knowledge to deal with the background pattern and noise, efficient and robust feature extraction methods are also one challenge. Given that the defect information is what matters for decision-making, the post-processing should feed data acquisition, i.e., developing integrated sensing-processing models is necessary.

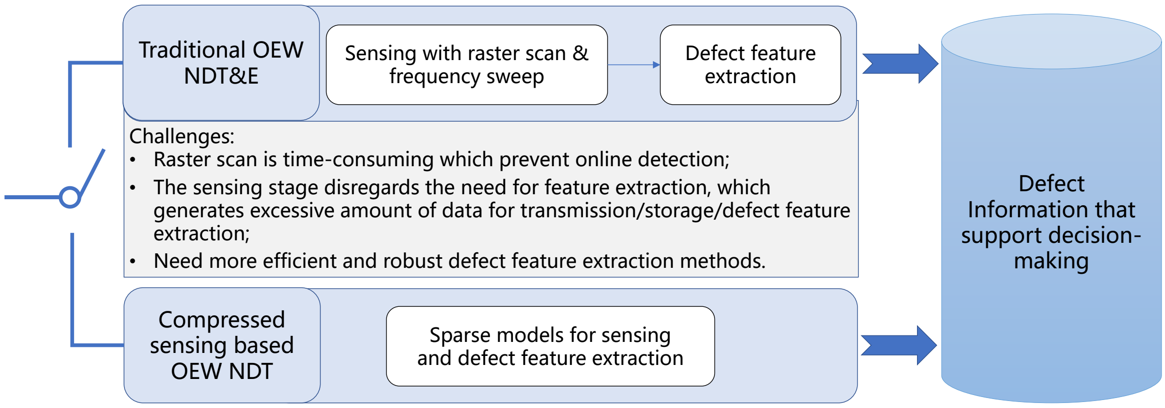

Figure 1.3 Diagram for research motivations

As one potential solution for the above challenges, compressed sensing (CS) provides a new sensing and signal processing framework which demonstrates impressive data compression ability in various applications. It thrives from 2006 by E. Candés, J. Romberg, and T. Tao [8] who demonstrated the rationale of CS theory from the mathematical perspective. Different from Shanon-Nyquist sampling theorem, CS can reconstruct signals from far fewer samples than that of Nyquist sampling rate by finding sparse solutions to underdetermined linear systems. Sparse, which serves as the prior information to CS, means only a small number of components in a signal are non-zero. The number of non-zero elements is called sparsity. This prior information in CS is in analogy with the prior bandwidth information in Shanon-Nyquist sampling theorem. Since then, CS has witnessed an increasing interest in many fields [9, 10]. One pioneer application for CS is the single-pixel camera [11], which sets a classic example of compressing image while taking. This single-pixel idea still inspires industrial designs [12-14]. Down-sampling capability makes CS attractive in medical fields. Application in magnetic resonance imaging (MRI) [15, 16] requires less scanning time, which incurs less radiation exposure to patients. Other fields like synthetic aperture radar tomography [17] and localisation [18] also witness the value of CS. Beyond downsampling ability of CS, integrated sensing-processing is a future direction for CS as indicated in the workshop report of ‘The Future Directions

Workshop on Compressed Sensing and the Integration of Sensing and Processing' in 2016 [2]. How CS adapts to the open-end waveguide NDT&E systems and contributes to extracting defect information to support decision-making is a remaining challenge.

1.2 Aims and Objectives

Based on the CS future direction of integrated sensing-processing and the challenges for open-ended waveguide NDT systems in Figure 1.3, this thesis aims to develop integrated sparse sensing-processing models for OEW NDT systems to address the challenges.

The objectives of this thesis are summarised below.

(1) Undertake a literature survey on the state-of-the-art CS technology and application instances in NDT&E systems to identify challenges and key issues of applying CS to solve the problem in traditional OEW NDT systems in Figure 1.3.

(2) Develop CS solutions to address the challenges of

  — time-consuming data acquisition using raster scan in traditional OEW NDT systems, which prevents online detection.

  — large data amount and processing overhead for the feature extraction process due to the front compressed sensing process did not consider the needs for the later feature extraction process in traditional OEW NDT systems.

  — robust and time-efficient feature extraction, such as defect region segmentation from texture background.

(3) Undertake case studies of low-energy impact damage detection for carbon fibre reinforced plastics (CFRP) materials for validation of the proposed CS solutions.

(4) Evaluate the proposed CS solutions and gives recommendation for future researches.

1.3 Overall methodology

The following overall methodology is adopted for the above aims and objectives. Firstly, conduct a literature review on sparse representation, measurement matrix design, sparse reconstruction of CS theory and its applications in NDT filed. Find out the state-of-the-art of CS and its application in the NDT field. Secondly, build up case study system for the aims and objective. Based on the case study system, investigate CS solutions for the challenges and objectives in the literature review. Finally, validate the proposed solution in the case study system. The process of design measurement matrix starts from sparse representation, i.e., build sparse models for the case study objectives. Then design measurement matrix that can be physically implemented. Followed by performing the proposed CS measurement in the case study system and extract the defect information. Reconstruct the whole data is not compulsory, because the ultimate goal is to extract defect information rather than get the full data. Finally, design defect region segmentation methods to give quantitative defect information.

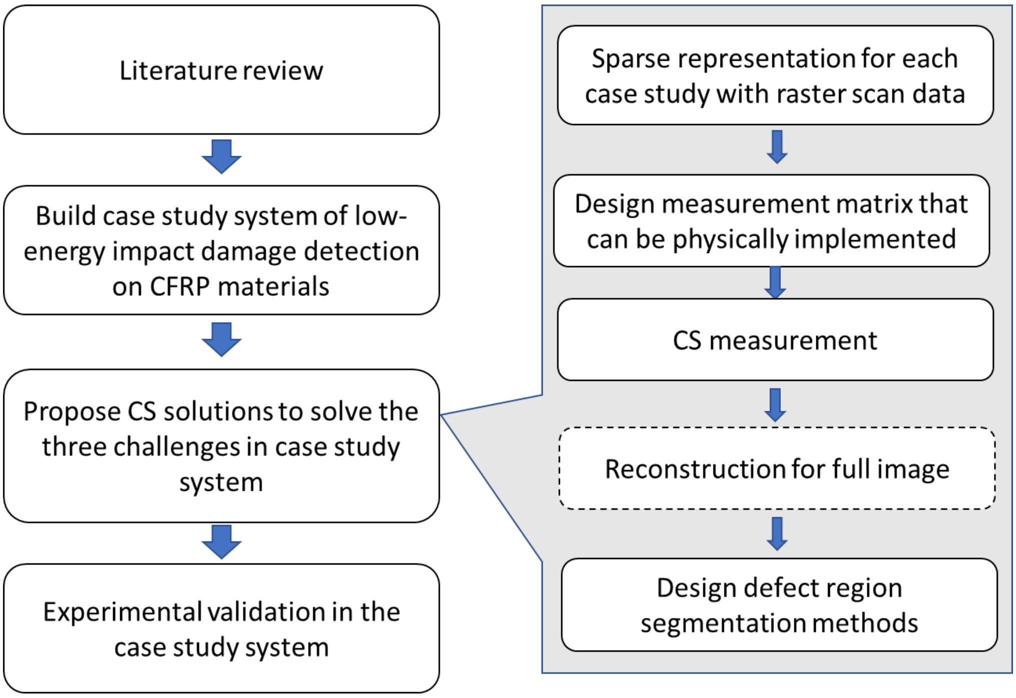

Figure 1.4 Overall methodology

1.4 Major contributions

This thesis develops CS sensing-processing models to address the three challenges in traditional open-ended waveguide NDT&E systems, the key issues and major contributions as briefly summarised in Figure 1.5 regarding the aims and objectives. More specifically, the major contributions are summarised hereunder:

(1) A review of CS theory regarding its sparse representation, measurement matrix design and sparse reconstruction is carried out to give a state-of-the-art of CS. Subsequently, review on NDT systems that use CS in their sensing, feature extraction, and classification stage is carried out to guide the CS solution design for OEW NDT systems. The key issues in using CS and different applications in Figure 1.3 are identified in section 2.5.4. Related works

including CS methods to address corresponding issues are reviewed to highlight the advantage of the proposed solutions.

(2) For the challenge of time-consuming data acquisition by raster scan that prevents on-line detection, an on-line compressed sensing model is developed to offer faster data acquisition and reduce sampling data amount without any hardware modification. The method explores the sparsity of spatial OEW NDT images. Instead of scanning the whole image as a raster scan, only a small part of pixels is scanned according to a customised 0/1 Bernoulli measurement matrix. The missing pixels are reconstructed with orthogonal matching pursuit algorithm. To address the issue of hard to determine the sampling pixel numbers that required for sparse reconstruction when lacking training data, an accumulated sampling process is developed. Compared to traditional raster scan designs which require complete spatial scanning for defect evaluation, this method achieves defect extraction in the data acquisition process without any hardware modification. Thus forming an on-line process. The case study in impact damage detection on CFRP materials shows the data acquisition time is reduced by one order of magnitude while maintaining comparable spatial image quality as traditional raster scan process.

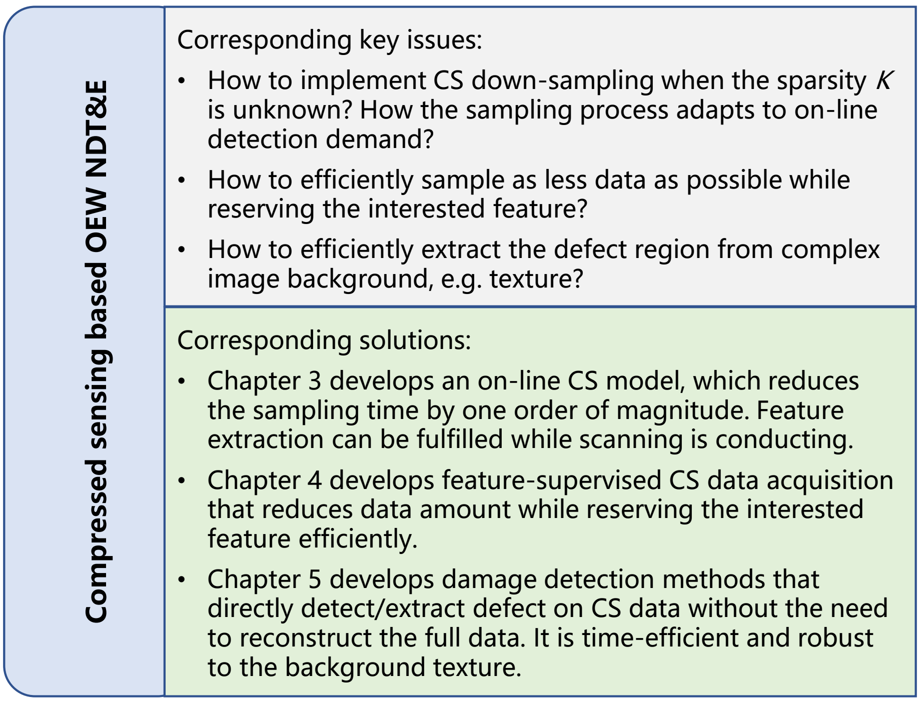

Figure 1.5 Diagram for research scope and main contributions

(3) In the on-line CS model, a histogram threshold edge detection (HTED) algorithm for damage region segmentation is proposed for low energy impact damage detection on CFRP

materials. The algorithm makes use of the histogram of spatial images to roughly segment the defect pattern first; then a clustering process is used to refine the segmentation. It is robust to background texture comparing to other image segmentation methods.

(4) To reduce the large data amount while researving the interested feature efficiently, a feature-supervised CS data acquisition method is developed. The frequencies which reveal the feature only occupy a small part of the frequency band, this method finds the sparse frequency range with CS sampling and sparse reconstruction. Subsequently, based on joint sparsity of neighbour frame, an aligned spatial-spectrum sampling scheme is proposed. The scheme only samples interested frequency range by using a customised 0/1 Bernoulli measurement matrix. The interested spectral-spatial data are reconstructed jointly which has much faster speed than frame-by-frame methods. The case study in impact damage detection on CFRP materials shows that the data amount is reduced greatly without compromising feature quality, and the gain in reconstruction speed is improved linearly with the number of measurements.

(5) Based on the above CS data acquisition methods, CS models are developed to directly detect defect from CS data rather than the reconstructed full spatial data as HTED. Firstly, based on the histogram is invariant to down-sampling using the customised 0/1 Bernoulli measurement matrix, a qualitative method which only gives binary judgement of the defect is developed. High probability of detection and accuracy is achieved compared to other methods. Secondly, a new greedy algorithm of spOMP-based defect pattern extraction method is developed to quantitatively extract the defect pattern, because the conventional sparse reconstruction algorithms cannot properly use the sparse character of correlation between the measurement matrix and CS data. The proposed algorithms show a fast detection speed and robustness than other algorithms in damage detection on CFRP materials.

(6) For research delivery during my PhD study, I have 5 peer-reviewed journal publications as first author, two international conference presentations, and more than 3 papers as co-author for the joint works with others. My google scholar citation reaches 215 in total, with h-index 9 and i10-index 9 for all my publications.

1.5 Thesis Layout

The layout for this thesis is summarised hereunder:

Chapter 2 gives an overview of compressed sensing. The state-of-the-art of CS in sparse representation, measurement matrix design and sparse reconstruction algorithms are reviewed. NDT applications that use CS in their sensing and feature extraction stage are reviewed. The key issues of applying CS in OEW NDT systems are highlighted.

Chapter 3 presents the CS-based on-line detection model for OEW NDT systems. The basic theory of OEW NDT for impact damage detection on CFRP and related works to address the time-consuming problem of raster scan are introduced firstly, followed by presenting each block of the proposed on-line detection framework. A case study in low-energy impact damage detection is carried out to compare the performance of the proposed method and raster scan method. The results of each block of the proposed method are evaluated before the chapter summary.

Chapter 4 elaborates feature-supervised CS data acquisition model. Based on the model in the last chapter, it begins with summarising the remaining problem of low reconstruction speed and large data amount for feature extraction due to independent sensing and processing. The related works are reviewed, followed by introducing the diagram of the proposed CS model, which consists of spatial-spectral sparsity representation, feature constraint for CS and joint reconstruction. Experimental implementation of the proposed feature-supervised CS model in impact damage detection for CFRP materials is introduced. The evaluation results for each stage of the algorithms are evaluated.

Chapter 5 presents the proposed qualitative and quantitative damage detection model using the obtained CS data with two subsections. Related qualitative and quantitative detection method from downsampling data with or without reconstruction are discussed. Their overall diagram, validation schemes and evaluation results with other methods are presented.

Chapter 6 summarises the overall project, derives conclusions and points out possible future work based on these investigations.

Chapter 2. Overview of Compressed Sensing

This chapter gives an overview of compressed sensing. The state-of-the-art of CS theory in sparse representation, measurement matrix design and sparse reconstruction algorithm are reviewed. NDT applications that use CS in their sensing and feature extraction stage are reviewed to get a state-of-the-art of how CS solves NDT problems. The key issues of applying CS in OEW NDT systems are highlighted from the review.

2.1 Introduction to Compressed Sensing

According to Nyquist–Shannon sampling theorem, the original information is perfectly reserved if the sampling rate is higher than two times of the highest signal frequency in a signal. However, compressed sensing (or compressive sampling, CS) enables a much lower sampling rate with sparse representation. A signal $\mathbf{x}$ is sparse if there are few (*K*) non-zero elements, the rest of the elements are zero or with very small absolute value, which are called *K*-sparsity. It is mathematically denoted as

$$\|\mathbf{x}\|_{\ell 0} \le K \tag{2.1}$$

where *K* is much smaller than the length of the signal **x**. Donoho [19] first proposed the original concept of CS. Candès, J. Romberg, and T. Tao [8], from the mathematical perspective, demonstrated the rationale of CS theory. Compressed sensing samples signals from different perspective comparing to Shanon-Nyquist sampling theorem. Sparse information is used in the former as prior information instead of bandwidth information in the latter. A signal may not be sparse in the time domain but some other transform domains, e.g. frequency domain, wavelet domain. The overall principle of CS is mathematically stated here.

Consider a signal $\mathbf{x} \in \mathbb{R}^{n\times 1}$, if $\mathbf{x}$ can be represented on a basis $\boldsymbol{\Psi} \in \mathbb{R}^{n\times n}$ as $\mathbf{x} = \boldsymbol{\Psi}\mathbf{s}$, and $\mathbf{s}$ has only K non-zero values ($K \ll n$), the signal can be measured using a measurement matrix $\boldsymbol{\Phi} \in \mathbb{R}^{m\times n}$ as:

$$\mathbf{y} = \boldsymbol{\Phi}\mathbf{x} + \boldsymbol{\xi} = \boldsymbol{\Phi}\boldsymbol{\Psi}\mathbf{s} + \boldsymbol{\xi} = \mathbf{A}\mathbf{s} + \boldsymbol{\xi} \tag{2.2}$$

where $\mathbf{y} \in \mathbb{R}^{m\times 1}$ and $m \ll n$; $\mathbf{A} \in \mathbb{R}^{m\times n}$, and the i-th column of $\mathbf{A}$ is denoted as $\mathbf{A}_i$; $\boldsymbol{\xi} \in \mathbb{R}^{m\times 1}$ is the noise term.

To recover $\mathbf{s}$ using $\mathbf{y}$ and $\mathbf{A}$ is to solve the following optimisation problem:

$$\min_{\mathbf{s}} \quad \|\mathbf{s}\|_{\ell_0} \text{ s.t.} \quad H(\mathbf{y}, \mathbf{As}) \leq \gamma \tag{2.3}$$

where $\|\cdot\|_{\ell_0}$ is the ℓ_0 -norm, which means the number of non-zero elements in a vector; $H(\cdot,\cdot)$ is a cost function that penalises the distance between the vectors $\mathbf{As}$ and $\mathbf{y}$, and γ is a tolerance. Note that Equation (2.3) is an NP-hard problem. A popular solution is to substitute ℓ_0 -norm by the closest ℓ_1-norm.

$$\min_{\mathbf{s}} \quad \|\mathbf{s}\|_{\ell_1} \text{ s.t.} \quad H(\mathbf{y}, \mathbf{As}) \leq \gamma \tag{2.4}$$

When $\ell_0 = \ell_1$ holding is a key to CS, which leads to many conditions like the restricted isometry property (RIP) condition [20]. Matrix $\mathbf{A}$ satisfies the RIP of order K if there exists a $\delta \in (0,1)$ such that

$$(1-\delta)\|\mathbf{x}\|_{\ell 2} \leq \|\mathbf{Ax}\|_{\ell 2} \leq (1+\delta)\|\mathbf{x}\|_{\ell 2} \tag{2.5}$$

holds for all $x \in \{x : \|x\|_{\ell 0} \leq K\}$. However, RIP is not computationally feasible to verify for a given matrix [21], and RIP is proved to be too restrict [22]. So mutual incoherence property (MIP) [23] is preferable in an industrial process:

$$K < \frac{1}{\mu(\mathbf{A})} \tag{2.6}$$

where $\mu(A) = \max_{i\neq j} |\langle \mathbf{A}_i, \mathbf{A}_j \rangle|$, $\langle \cdot,\cdot \rangle$ is the inner product and $|\cdot|$ is the absolute value function. Mutual incoherence measures the greatest correlation coefficient between any two columns; this is also not an easy task to calculate. Fortunately, it usually automatically satisfied by choosing $\mathbf{\Phi}$ from some random matrix like 0/1-Bernoulli matrixes [24] and independent identically distributed Gaussian matrixes [20] in most cases. The constraint for sample numbers for reconstruction guarantee is

$$\alpha\mu^2 K \log n \leq m \tag{2.7}$$

where α is a factor corresponding to different instances. So, smaller mutual incoherence leads to fewer required samples.

Based on these conditions, the optimisation problem can be solved by recovery algorithms. Finally, $\mathbf{x}$ is obtained using $\mathbf{x} = \mathbf{\Psi s}$. Interestingly, the measured signal is far smaller than the original signal since $m \ll n$, which means the original signal is compressed when it is sampled.

Diagram representation of the compressive sensing theory is given out in Figure 2.1. Among all the operation process, there are three key elements: sparse representation, design measurement matrix and sparse reconstruction algorithm.

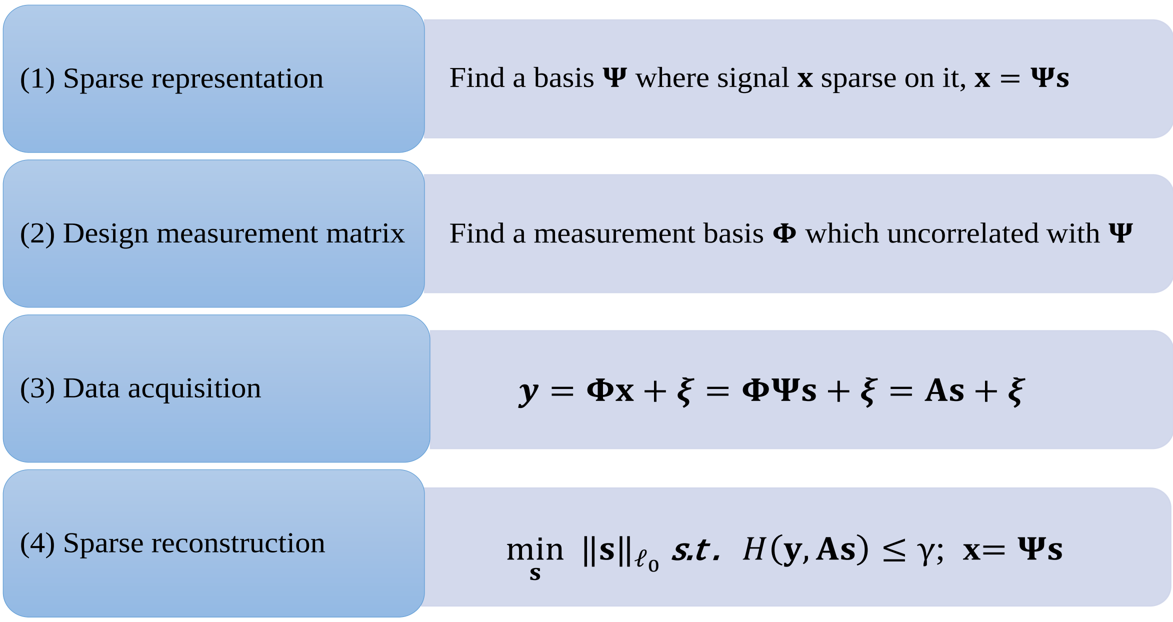

Figure 2.1 Diagram of compressed sensing

The above signal model is a one-dimension vector, but lots of signals are in multi-dimension such as images and videos. Some signal even consists of multi-domain information, e.g. frequency sweep measurement of a spatial area. Although these high-dimensional signals can be reshaped into one-dimension signals, the size of the measurement matrix will grow rapidly and results in rapid growth in reconstruction time as well. Fortunately, if these high dimension signals (denote as $\mathbf{X}$) share the same sparsity pattern on the same basis, i.e., all one-dimensional signal for each column share similar non-zeros positions, but with different values, they can be reconstructed jointly. This is called group sparsity or joint sparsity [25]. Using the same notation in the previous discussion and substitute with matrix form, reconstruction of group sparsity signal can be modelled as:

$$\min_{\mathbf{S}} \quad \|\mathbf{S}\|_{\ell 2,0} \ \text{ s.t. } \ H\left(\mathbf{Y}, \mathbf{AS}\right) \leq \gamma \qquad (2.8)$$

where $\|\mathbf{S}\|_{\ell x,y}$ means imposing ℓ_x -norm on columns then ℓ_y -norm on rows to the matrix $\mathbf{S}$. This problem can be solved using the same reconstruction algorithm as solving Equation (2.3) by adapting to matrix forms like ADM [26], CoSaOMP [27]. The reconstruction time for group sparsity signals can be reduced greatly than sequential reconstruction.

2.2 Sparse Representation in Compressed Sensing

In practical applications, sparse representation (i.e. find the sparse basis $\mathbf{\Psi}$) is the first and foremost step of CS. The goal is decomposing the original signal $\mathbf{x} \in \mathbb{R}^{n \times 1}$ in a small number of terms or a series with significantly decaying coefficients as Equation (2.9), where $K \ll n$.

$$\mathbf{x} = \mathbf{\Psi s} \ \text{ s.t. } \ \|\mathbf{s}\|_{\ell 0} \leq K \qquad (2.9)$$

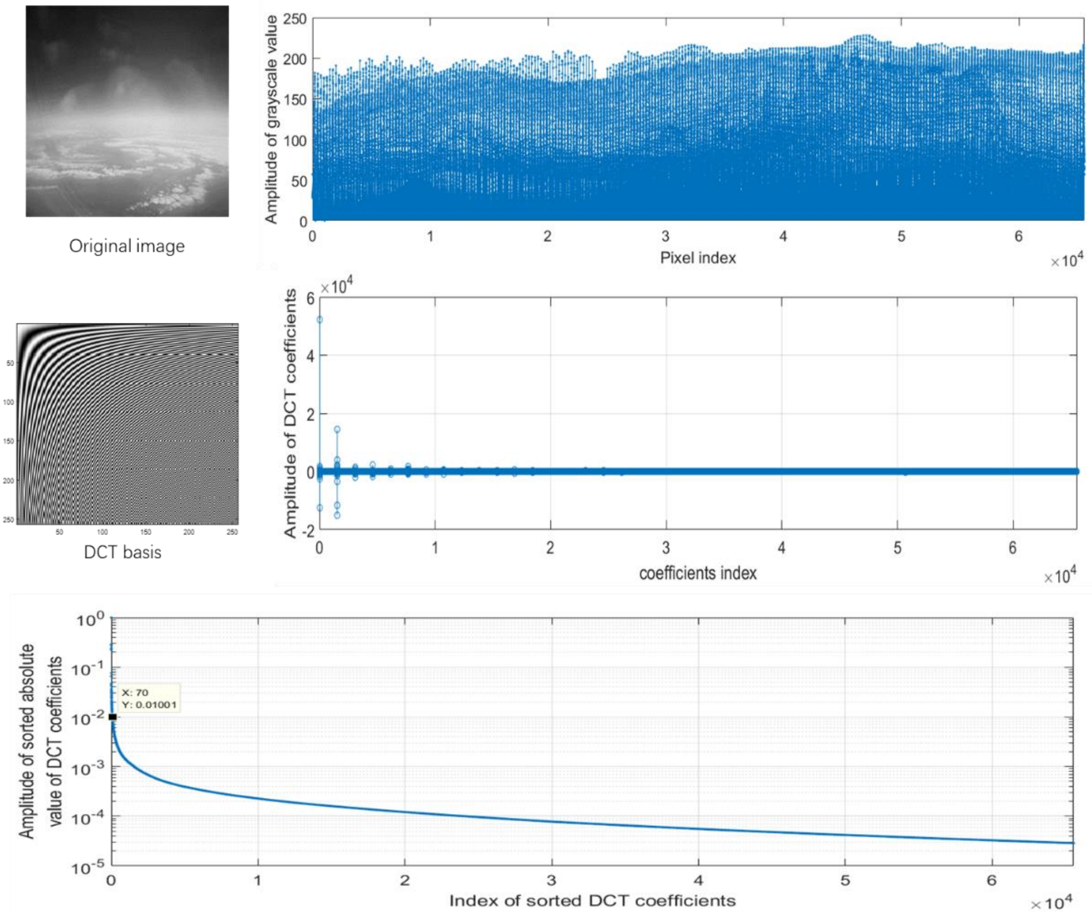

Figure 2.2 A demo for sparse representation. The original image is decomposed onto DCT basis, and sparse property is observed for the DCT coefficients.

Figure 2.2 gives a demo for sparse representation. The example signal (**x**) is the grayscale of a cloud image in size 256×256. The discrete cosine transform (DCT) of the original signal shows only a small part of the dominant components, most of the DCT coefficients ($\mathbf{s}$) are close to 0. The sparse basis is the DCT basis ($\mathbf{\Psi}$) in this example. When sorting the absolute value of the DCT coefficients in descend order, a rapid decay is observed, which illustrates the sparse of **s**. The K value can be found by thresholding the sorted absolute value of DCT coefficients. For example, the 70th sorted coefficient decays to around 0.01 of the max coefficient. The rest of the coefficients contribute little to the overall image, thus can be discarded. So, K is 70 in this case.

There are two main categories of sparse representation method, i.e., decompose on a fixed dictionary [28, 29] and the dictionary learning approach [30-32].

Fixed dictionary are some known transform basis based on the prior knowledge of specific applications, such as [28] Fourier dictionary, wavelets, complex wavelets, Gabor dictionary, wavelet-packs and cosine-packets. For some one-dimension signals, the wavelet transform may be the best choice, while for images curvelet or contourlet may be the best. It is also possible that a combination of several bases is most suitable for some applications [29].

Dictionary learning approaches suggest inferring the dictionary from a set of examples by machine learning techniques when the prior sparse knowledge is difficult or impossible to obtain. Enough training data is necessary. Dictionary learning algorithms range from the well-known and simple principal component analysis (PCA), to the K-SVD [33], the Sparse K-SVD [34], ℓ_1-K-SVD [35], the multi-scale dictionary learning [36, 37], the online dictionary learning [38], the RLS-DLA [39], etc.

2.3 Design Measurement Matrix in Compressed Sensing

Sparse representation gives a new perspective to understand signals beyond frequency, it also leads to new data acquisition model that differs from Shannon-Nyquist sampling theorem. This data acquisition is mathematically supported by the measurement matrix $\mathbf{\Phi}$. As introduced in section 2.1, the multiplication of measurement matrix and sparse basis need to meets some constraints like RIP and MIP to guarantee sparse reconstruction. According to the MIP condition, random matrix usually has a low correlation with sparse basis, which leads to low

$\mu(A)$. So random matrix can be adopted as measurement matrixes for most cases [40], e.g. independent identical Gaussian matrix, random Bernoulli matrix, partially orthogonal matrix, cyclic matrix, etc.

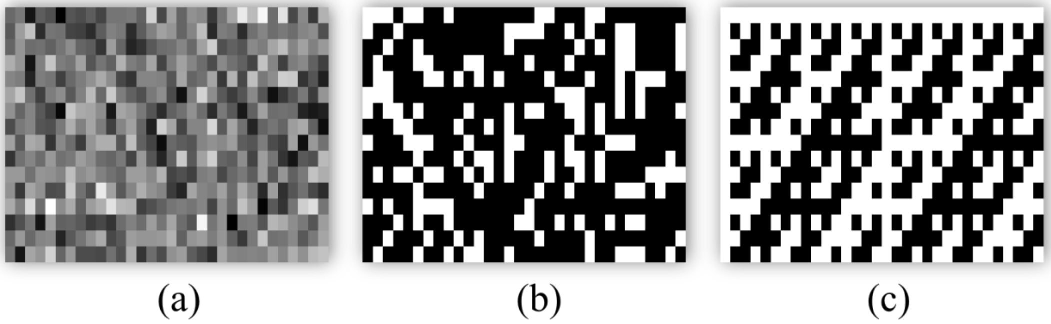

Figure 2.3 Demo measurement matrices with size 16×32 for (a) random Gaussian matrix; (b) random 0/1 Bernoulli matrix; (c) Hadamard matrix

Random measurement matrices have wide applicability, but they are not convenient to generate in some cases. Structured measurement matrix is proposed for this reason [41, 42]. Examples are random Hadamard matrices, Toeplitz matrices, random demodulator (RD) matrices, random convolution (RC) matrices, structurally random matrices (SRM). Structured measurement matrices normally have less storage requirement, reproducibility and reduced transmission overhead. However, structured measurement matrices usually require a higher number of measurements than random matrices [41, 42].

Measurement matrix will influence the physical implementation of data acquisition. The random Bernoulli matrix and Hadamard matrix [43] can be implemented by individually control the on/off status of each element, examples are spatial light modulator (SLM) [11], digital micromirror devices [12, 44, 45], 2-bit programmable metasurface [46]. As a representative method to implement on/off status control, digital micromirror devices have a mechanical structure that switches the two tilt angles of the individual pixel as shown in Figure 2.4(a) [47]. Only one of the tilt angles can reflect the corresponding light intensity into a sensor that measures the summation of all reflected light intensity. A single row denotes the tilt angle status of all mirrors for a measurement, the measurement number is decided by the number of rows in the measurement matrix. Random Gaussian matrix is implemented with elements that have random signal gain, examples are metasurface [13, 48, 49], external-cavity semiconductor lasers [50]. Metamaterials/metasurface is a typical way to implement random matrices that have multi-value elements. Metamaterials are man-made metal or dielectric structures that show properties that not found in nature, such as a negative index of refraction [51, 52]. This class of artificial material can be fabricated into nanoscale and 3D structures [53], which attracts wide application interest in microwave [13, 54], Terahertz [55, 56], acoustic [57], and optical [58, 59] systems. Meta-surfaces are planar metamaterials with subwavelength thickness, this 2D structure can greatly suppress the undesirable losses in the wave propagation direction. One field of application of metamaterials is the imaging system [13, 46, 48, 60]. Figure 2.4(b) [48] shows a metasurface structure. The metasurface consists of an array of electric-field-coupled (ELC) resonator, which has a different frequency response curve for an individual element. The measured frequency response in the far-field is the superposition of frequency response for individual elements. The measurement matrix is usually calibrated in an element-wise manner, which makes each rows corresponding to a unique element in the array.

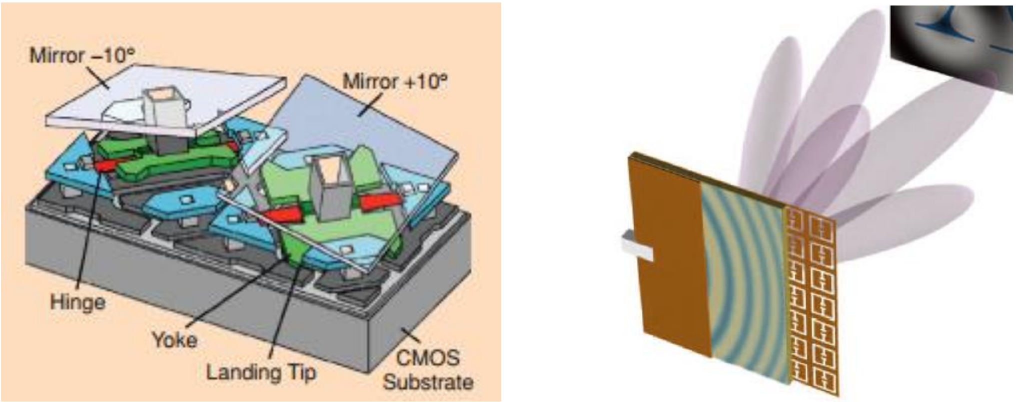

(a) (b)

Figure 2.4 Measurement matrix implementation demo of (a) Bernoulli matrix [47] and (b) Gaussian matrix [48].

2.4 Sparse Reconstruction Algorithms in Compressed Sensing

From a mathematical point of view, reconstruction is solving undetermined equations under sparse constraints. From an implementation point of view, it is using as less weighted atom (the column of $\mathbf{A}$) as possible to represent the measurement results $\mathbf{y}$. Concerning the analytical solution and optimisation viewpoints, the available sparse reconstruction methods are categorized into four groups, i.e. the convex optimisation-based methods, greedy algorithms, combinatorial algorithms and Bayesian methods [10, 25, 61-63]. The reconstruction problem is same as many machine learning problem [64-66], which indicates some interesting link between CS and artificial intelligence (AI).

Convex optimisation-based methods: The core optimisation problem for CS reconstruction in Equation (2.3) is equivalent to the unconstrained problems for an appropriate penalty parameter λ

$$\arg\min_{\mathbf{s}} \quad \|\mathbf{s}\|_{\ell_0} + \lambda H(\mathbf{y}, \mathbf{A}\mathbf{s}) \tag{2.10}$$

For convex programming algorithms, the most common choices of $H(\cdot,\cdot)$ is $H(\mathbf{y},\mathbf{A}\mathbf{s}) = \frac{1}{2}\|\mathbf{y}-\mathbf{A}\mathbf{x}\|_{\ell 2}$, and $\|\mathbf{s}\|_{\ell_0}$ is relaxed to convex form $\|\mathbf{s}\|_{\ell 1}$. This is a typical Lasso problem. For more general cases, $\|\mathbf{s}\|_{\ell_0}$ can be substitute by $\|\mathbf{s}\|_{\ell p}$ with proper $H(\cdot,\cdot)$. Figure 2.5 presents the solution of substituting by $\|\mathbf{s}\|_{\ell p}$ in Equation (2.10) for a tilted hyperplane (serving as the constraint-set) with various *p*. It becomes non-convex for 0<*p*<1, which is difficult to solve. When $p \geq 1$, it is a convex optimisation problem, which means the standard convex analysis methods can be applied. Some example algorithms are gradient projection [67], interior-point based methods [68], alternating direction method [69], proximal algorithms [70], Bregman iteration methods [71].

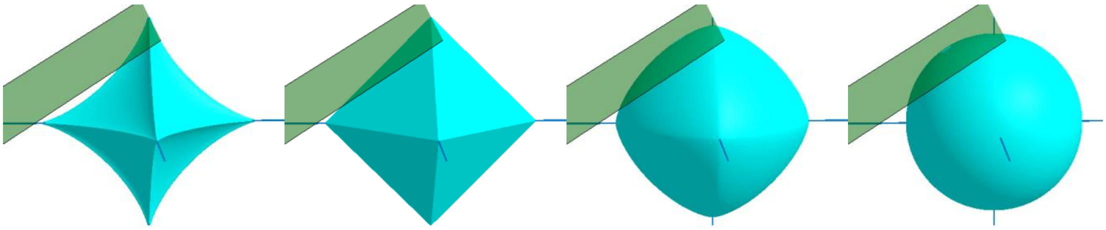

Figure 2.5 The intersection between the p-ball and the set $\mathbf{Ax} = \mathbf{y}$ *defines the solution of* $\|\mathbf{s}\|_{\ell p}$.

Greedy algorithms: Greedy algorithms deal with $\|\mathbf{s}\|_{\ell_0}$ minimisation directly. Recall that the goal of sparse recovery is to recover the sparsest vector **s** which explains the linear measurements **y**. Greedy algorithms pursuit this goal by greedily selecting columns of **A** and forming successively better approximations to **y**. It aims to search for the best local optimal solution in each iteration with the goal of achieving the optimal holistic solution [72]. This section takes the Orthogonal Matching Pursuit (OMP) algorithm [73] as an example.

Algorithm: Orthogonal matching pursuit (OMP)

Input: $\mathbf{y} \in \mathbb{R}^{m\times 1}$: measurement results;
$\mathbf{A} \in \mathbb{R}^{n\times 1}$: measurement matrix;
γ: Threshold value for stop iteration.
Output: sparse signal $\mathbf{x} \in \mathbb{R}^{n\times 1}$
Initialization: $\mathbf{r} = \mathbf{y}$, $\Lambda = \emptyset$;
while $\mathbf{r}^T\mathbf{r} > \gamma$ **do**
  Orthogonal projection: $\mathbf{C} = \frac{|\langle \mathbf{A}_i, \mathbf{r}\rangle|}{\|\mathbf{A}_i\|_{\ell 2}}, i \in \{1, 2, 3, ..., n\}$
  Identify support:
  Λ_Δ = index of $\max(\mathbf{C})$.
  Update:
  $\Lambda = \Lambda \cup \Lambda_\Delta$;
  Perform least square estimation: $\hat{\mathbf{x}} = \left(\mathbf{A}_\Lambda^T\mathbf{A}_\Lambda\right)^{-1}\mathbf{A}_\Lambda^T\mathbf{y}$;
  $\hat{\mathbf{y}} = \mathbf{A}_\Lambda\hat{\mathbf{x}}$;
  $\mathbf{r} = \mathbf{y} - \hat{\mathbf{y}}$.
end

Figure 2.6 Orthogonal matching pursuit (OMP) algorithm

OMP algorithm first projects the measurement results on the orthogonal subspace. This projection is achieved by inner product operation, because $\langle \mathbf{A}_i, \mathbf{r}\rangle = \|\mathbf{A}_i\|_{\ell 2}\|\mathbf{r}\|_{\ell 2}\cos\theta$. The inner product is exactly the projection of $\mathbf{r}$ on $\mathbf{A}_i$ when divided by $\|\mathbf{A}_i\|_{\ell 2}$. This orthogonal projection represents the correlation of **r** to each atom. The atom which has a larger correlation with **r** contributes more to the measurement results, so it is selected in an iteration. Then the selected atom is used to represent the measurement results. The weighting of each atom is decided by least square estimation to minimise the representation error. The selected atoms are removed from the candidate atoms for the latter iterations to avoid repetitive work. To get a smaller representation error, the residual is sent to the projection step to find more atoms. By greedily finding the most correlated atoms to explain the residual, the representation error will convergent to a pre-defined threshold. If the measurement results are corrupted by noise, the representation error cannot reach 0 because the noise term is uncorrelated to the measurement matrix. So the stop threshold can be found by estimating the noise level.

MIP condition in Equation (2.5) defines a sparse reconstruction condition. Cai et al. [21] prove that $\mu < 1/(2K-1)$ is a sufficient condition to recovering K -sparsity signal exactly using OMP. An essential problem in OMP is the stop rule for iteration, which depends on the noise structure. The iteration stops if the residual ($\mathbf{r}$) is below a certain threshold. This threshold for OMP under Gaussian noise environment is given in *Theorem 7* in [21] as:

$$\|\mathbf{r}\|_{\ell_2} \leq \sigma\sqrt{n + 2\sqrt{n \log n}} \qquad (2.11)$$

where σ is the standard deviation of the Gaussian noise. Using this threshold will reconstruct successfully with probability at least $1-1/n$.

Some example algorithms for this category are Matching Pursuit (MP) [74], Series of Matching Pursuit [75], Hard Thresholding Pursuit (HTP) [76], Subspace Pursuit (SP) [77], CoSaMP [27], Iterative Hard Thresholding (IHT) [78].

Combinatorial algorithms: Combinatorial algorithms are algorithms for investigating combinatorial structures from the graph theory perspective. Combinatorial structures are collections of *K*-subsets/*K*-tuple/permutations from a parent set (finite), this is similar to the concept of sparse. Basic steps include generation, enumeration and search. For a particular type, generation is constructing all combinatorial structures. Enumeration is computing the number of all different structures. Search is finding at least one example of a combinatorial structure (if one exists). The optimisation problems in CS is also a type of search problem. These search problems can be solved by ripe algorithms like hill-climbing, simulated annealing, Tabu-search, genetic algorithms. This idea is adopted in sparse signal reconstruction [79-81].

Bayesian methods: Bayesian methods assume the sparse signal obeys a known probability distribution and regarding the stochastic measurements $\mathbf{y} = \mathbf{Ax}$ as a probability distribution related to each nonzero element of $\mathbf{x}$. The distribution of $\mathbf{x}$ needs to ensure $\mathbf{x}$ is compressible, usually by a two-state Gaussian mixture distribution, with each signal element taking either a large or small value. The process to estimate $\mathbf{x}$ is a Bayesian inference problem. The marginal distributions of elements in $\mathbf{x}$ conditioned on the observed measurement need to be approximated. $\mathbf{x}$ can be estimated following the Maximum Likelihood Estimate (MLE) or Maximum a Posteriori (MAP) from their distributions. This estimation can be solved by methods like belief propagation method (BP) [64, 82-84] or Relevance Vector Machines (RVMs) [85, 86]. A key advantage of the Bayesian methods is that it enables the evaluation of error bars on $\mathbf{x}$. These error bars services as a guide in selecting the linear projections to reduce uncertainty in the signal, which provides an intriguing connection between CS and machine learning techniques such as active learning [66, 87, 88].

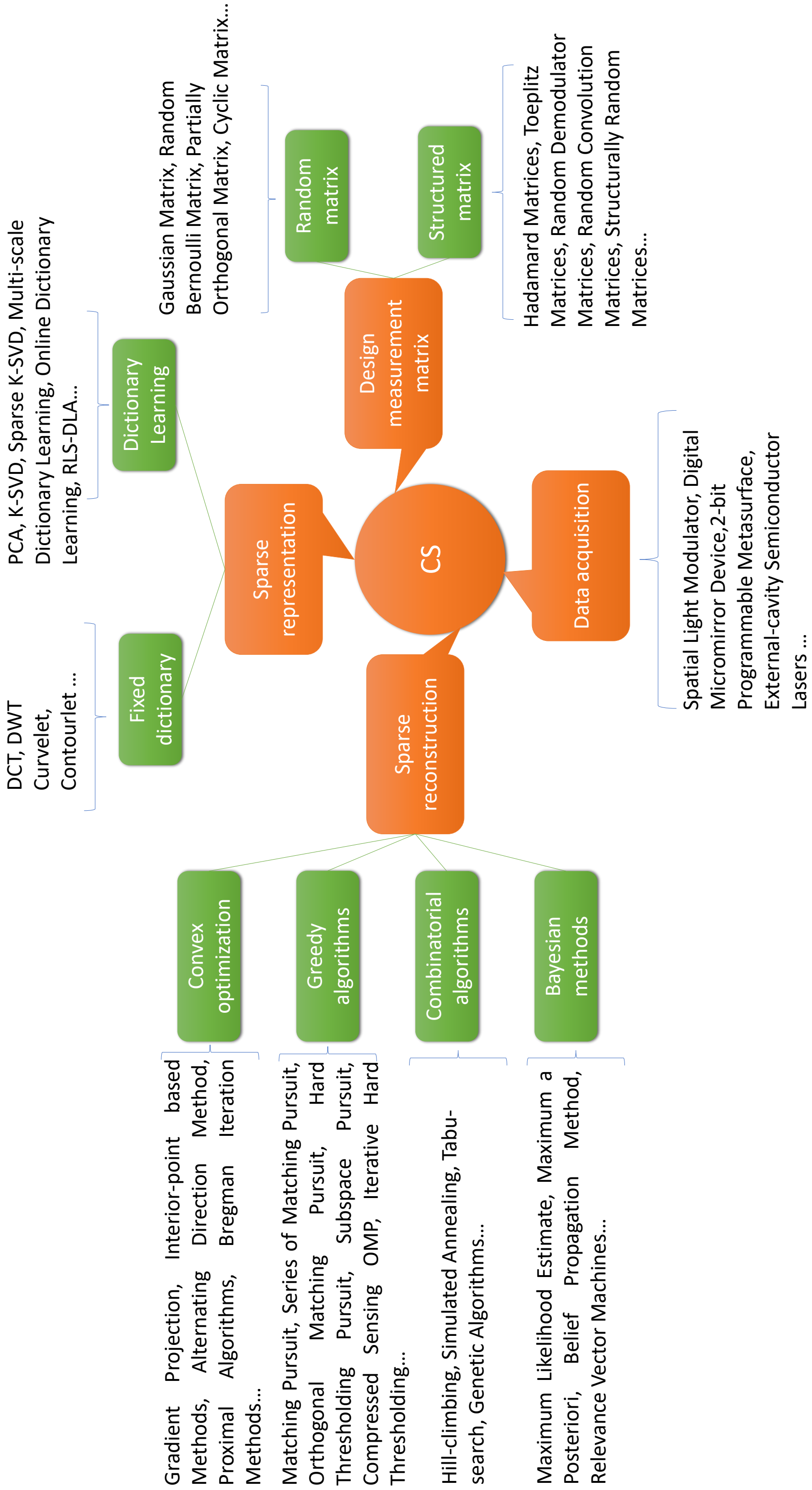

Figure 2.7 Knowledge-tree for CS theory

Among all these categories, convex optimisation algorithms require least measurements but are computationally more complex. Bayesian methods can get the quantitative remaining estimation errors but have considerable computation complexity. Combinatorial algorithms are fast in some scene but call for many measurements, which lessens the advantage of CS. Greedy algorithms are in a good trade-off between those extremes.

By far, the key issues and the state-of-the-art methods in CS theory are reviewed. Figure 2.7 gives a knowledge tree for CS theory, which summarises the above review for CS theoretical background. CS provides a way of using sparse models to solve sensing and signal processing problems, which has the potential to solve challenges like an excessive amount of data using Shannon-Nyquist sampling for NDT applications. Note that NDT&E is not only about data compression, feature extraction for quantitative evaluation is another major concern. The next section reviews the CS theory in the sensing, feature extraction and feature classification stage of NDT&E systems.

2.5 Compressed Sensing in NDT&E Applications

As discussed previously, developing smart sensing technologies that efficiently support the information-based decision by integrating sensing and processing is increasingly important for condition-based maintenance in NDT in the Industry 4.0 era. As an NDT technique which has an advantage over others like contactless measurement and high resolution, current OEW NDT systems have separate sensing and feature extraction which meets challenges to thrive in the trend. From the sensing side, firstly, the time-consuming data acquisition by raster scanning prevents on-line detection. Secondly, the sensing stage disregards the demand for the latter feature extraction, leading to an excessive amount of data for transmission/storage and feature extraction. From the feature extraction side, OEW NDT systems need robust and time-efficient feature extraction methods to segment the background and foreground from the scanned images. This thesis aims to solve these problems in OEW NDT systems with CS models.

Compressed sensing is widely used in field like medical imaging [15, 89-92], SAR imaging [93-96], channel parameter estimation [97-102], etc. However, to the best of the author’s review, there is few CS application in OEW NDT&E systems, and the related research in other NDT&E systems are in an initial state. This section gives an overview of CS application in sensing, feature extraction and defect classification in NDT&E fields to inspire the design in OEW NDT&E systems, and heights the issues of current CS methods for OEW NDT systems in the last sub-section.

2.5.1 Sensing with Compressed Sensing

Sensing is the first and foremost step for NDT&E. There are little hardware sensing systems based on CS for NDT applications. Most studies still use simulated CS data for investigation. This section organises the CS sensing implementation in NDT applications according to the signal domain, i.e., time domain, frequency domain, and spatial domain.

Time & frequency domain: This kind of signal type is usually found in vibration-based NDT like acoustic emission [103], lamb wave inspection [104, 105]. These NDT systems use the traditional method for sensing. CS data is simulated by imposing measurement matrix on the original data. Frequency data is obtained by Fourier transform. Other examples are [106-116].

Spatial domain: This kind of signal type is usually found in microwave NDT, laser scanning, THz, etc. Spatial domain signal witnesses more hardware level CS sensing which implements the measurement matrix by hardware or virtual spatial masks. These masks lead to various weighted summation of the full signal, which corresponds to the CS measurement $\mathbf{\Phi x}$. The virtual masks are commonly implemented by random scan pattern. A random line scanning method in a laser scanning system is presented in [117]. Random scanning pattern is presented in [118] for a microwave imaging system. Hardware masks are structures that will block or modulate the interested signal. A rotating multi-mask is used in [119] for human situation recognition via a pyroelectric infrared sensor. The rotating multi-mask generates different masks under different rotation angle as shown in Figure 2.8(a). A digital micromirror device (DLP3000 with the DLP LightCrafter from Texas Instruments) is used as the mask in a near-field THz imaging system [44] to detect hidden objects. A spatial light modulator (SLM) for THz image is implemented in [120]. The SLM achieved different absorption for Hadamard mask as shown in Figure 2.8(b).

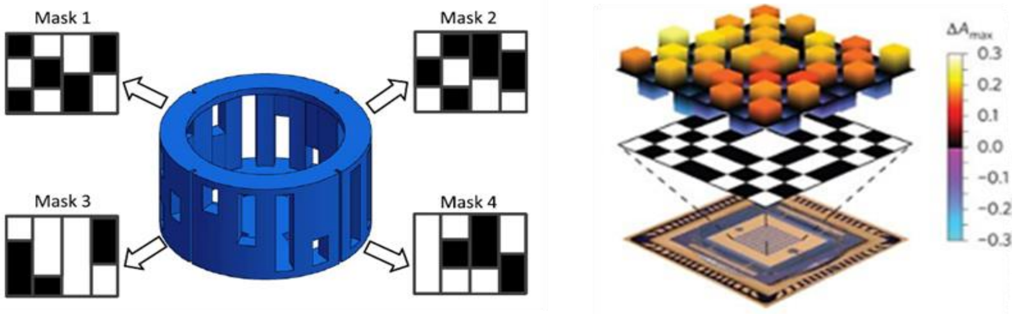

(a) (b)

Figure 2.8 Demo of hardware masks for (a) human situation detection with the pyroelectric infrared sensor [119] and (b) an SLM for THz imaging [120].

For spatial domain signals, there is another category of CS instance that not based on masks. They use the data from standard defect samples are the sparse dictionary and regard the defect signal as the weighted sum of the dictionary signal. The sparse dictionary signals are pre-calibrated and no hardware modification is required for CS data acquisition. An example is compressed sensing for the detection and positioning of dielectric objects inside metal enclosures using microwave measurements in [121]. The dielectric objects are inside the metal enclosures, and six waveguide probes are used for measurement as shown in Figure 2.9(a). Measurement region with a dielectric cylinder placed at 2379 different positions that shown as a honeycomb pattern in Figure 2.9(b).

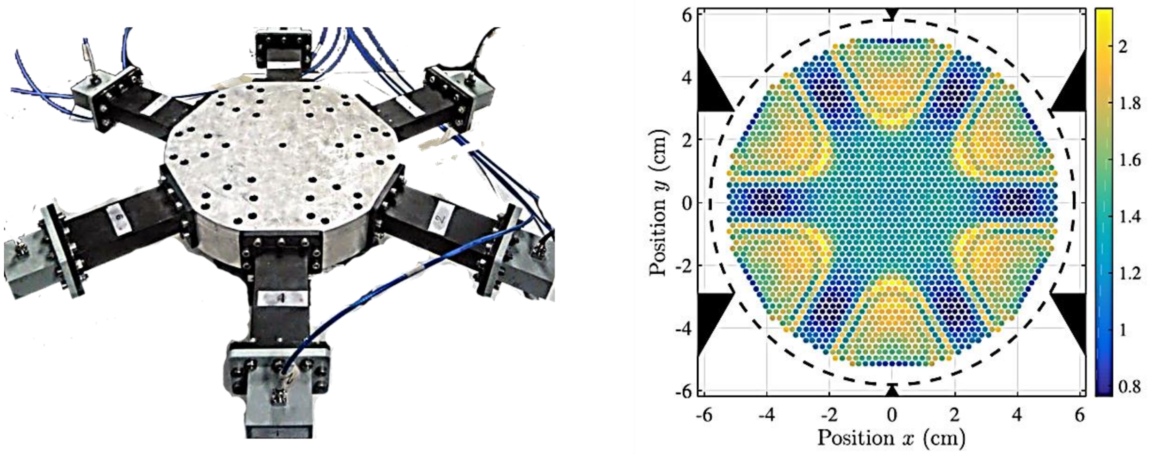

(a) (b)

Figure 2.9 A demo of calibration-based CS for NDT [121]. (a) The experimental setups; (b) The calibration dictionary.

2.5.2 Feature extraction with Compressed Sensing

Concerning when feature extraction is realised related to the sparse reconstruction stage, methods of feature extraction with CS in NDT applications can be categorized as post-reconstruction extraction, pre-reconstruction extraction, and in-reconstruction extraction.

Post-reconstruction extraction: This category only uses CS in the data acquisition stage to compress signal and performs feature extraction on the reconstructed signal. CS and the subsequent feature extraction procedures are sequentially realised. This is the most primitive and most popular application category [10], especially for image data. A CS-based sparse time-frequency representation is presented for finding buried linear structures and impulsive signatures [107]. The design requires less time and space to store the time-frequency information without bringing in significant artefacts in the time-frequency signal in fault diagnosis of bearings. A CS design in the post-processing on the measured S21 parameter in mm-wave NDT in composite panel is presented in [108]. The design reduces measurement time by removal of a reference measurement while maintaining image quality. An application of CS for reconstructing spatially dependent Raman spectra for spatial and spectral flame diagnostics is shown in [110]. They prove that similar spectra can be obtained with the CS scheme within short acquisition times. A method which uses the difference of the recovery image under different sparse basis for damage localisation in lamb wave testing is presented in [104]. Acquisition time is significantly reduced without losing in detection accuracy. In damage localisation in lamb wave inspection, [122] use wrapped frequency transform for sparse representation. The original impulse response can be reconstructed, and the impulse response can indicate the scatter position together with the reflectivity function.

Pre-construction extraction: This category extracts feature on the CS measurement results before the reconstruction stage. It is popular for features that are invariant to downsampling [90, 103, 106, 117] and features that learned by machine learning such as a deep neural network (DNN). The CS data is directly used as a feature in [106] for diagnostics and prognostics in electromagnetic solenoids, because it is observed that the values of some sampling points have a linear correlation with cycle number. The energy of compressively-sensed data is used as a feature for analysis in acoustic emission signal processing for rolling bearing running state assessment [103]. The proposed feature and traditional time-domain feature have the same trend of the running state of rolling bearings. Spectral-energy distribution is chosen as a feature in an EEG acquisition and biomarker extraction system [90], because the distribution of energy of compressed measurement is approximately the same as that of the original signal. Also use distribution as a feature, [117] uses the histogram of CS data from misalignment and bearing damage laser-scanning signal as a feature, because the histogram is invariant to downsampling. [123] proposed an algorithm to extract centroid feature of the star from CS data in star images. Another subcategory uses machine learning to automatically learn a vector as feature. Example applications are CS in EEG signal [124], pyroelectric infrared motion sensor-based gesture detection [119], bearing fault diagnosis [113, 114], diagnosis of large linear arrays [125].

In-reconstruction extraction: This category directly reconstructs feature from the CS data. Sparse representation to the features rather than the original data is adopted. Some feature is sparse such as frequency harmonic components, while more manipulation such as subtract measurement data from the reference data is needed for sparse representation. For the former case, the original vibration signal is sparse in the frequency domain for wind turbine monitoring, so the periodic impulsive feature in the frequency domain can be directly reconstructed in [109]. Similarly, in a vibration signal-based roller bearing faults detection system [111], the position of the high frequency is the target feature because faults lead to high-frequency components in the spectrum. The fault features can be detected far before the full reconstruction if the fault feature is significant in the spectrum, because algorithm like OMP always finds the most significant atom in each iteration. The harmonic components and the period information of impulsive components are used as features to identify a fault in vibration test on machines in [112]. Out-race fault influences on the period of impulsive components, misalignment fault brings harmonic frequency, they are sparse in the spectrum. For the latter case, the difference between the excitation coefficient and excitation of a reference failure-free array is sampled in an array diagnosis application [126]. When the number of fault elements is small, the difference is sparse and will indicate the fault location. The same method is used in diagnosing the process faults in multi-station assembly processes by subtracting measurement from specification [127]. Instead of using defect-free data as a reference, another way is using defect data as a reference. In a system for detection and positioning of dielectric objects inside metal enclosures by microwave measurements [121], each position for unit dielectric objects is pre-obtained as the sparse dictionary, then do CS reconstruct with the measured superposition signal. The reconstruction image indicates the object position.

2.5.3 Defect classification with Compressed Sensing

CS is used in NDT applications for defect classification. The basic idea is using the different defect class as a sparse dictionary and find the most sparse representation of the measurement on the sparse dictionary. The number of dominant sparse coefficients indicate the probability of belonging to each class. This in line with the purview of pattern recognition in the computer science field [128]. The idea is witnessed in a partial discharge pattern recognition of XLPE cables system [129]. It is worth noting that when the dictionary is trained from defect-free samples, defect detection can be achieved by check the representation error. A defect data brings in large sparse representation error while defect-free data have small representation error.

This is a special case of defect classification. An example is a fault detection system via sparse representation for semiconductor manufacturing processes [130].

2.5.4 Challenges of CS methodology in open-ended waveguide NDT&E

From the CS theory point of view, experts in mathematics side put considerable effort into digging sparse representation, measurement matrix design and sparse reconstruction algorithms. A workshop of Future Direction in Compressed Sensing and the Integration of Sensing and Processing is held in January 2016 at Duke University in Raleigh-Durham [2]. This workshop gathers experts in CS research. The workshop report outlines the future direction of CS for the next 10 to 15 years. One of the future goals is ‘Sensing + X’ or Task Oriented Sensing, which jointly consider sensing and processing for integrated sensing-processing solutions. Based on this benchmark, this thesis works on integrated sensing-processing solutions with CS for open-ended waveguide NDT systems, instead of focusing on the theory side of CS such as non-convex optimisation algorithms.

The review of CS application in NDT&E indicates that there is no CS design in open-ended waveguide systems for NDT&E, and CS in NDT applications are still in its infancy. CS witnesses some application in laser scanning systems which use down-sampling to reduce the scanning time, and some frequency harmonic components feature extraction in vibration-based NDT&E systems. There are many remaining issues for CS in NDT&E applications, especially for OEW NDT&E systems. As mentioned in Chapter 1, waveguide NDT systems have some critical challenges in sensing and feature extraction. The corresponding key issues of using CS in OEW NDT&E systems to address these challenges are summarised as follows:

(1) The data acquisition is time-consuming using raster scan and frequency sweep in traditional open-ended waveguide NDT systems, which prevents on-line detection. Open-ended waveguide NDT systems use raster scan to acquire spatial images, and each scanning point needs frequency sweep to obtain frequency response. This process is very time-consuming when the scanning area becomes large. There are some designs using a waveguide antenna array to reduce scanning time [131], but it leads to more expensive and more power-consuming data acquisition devices. On the other hand, less scanning point contributes to reducing sampling time. In the literature review in section 2.5.1 to 2.5.3, CS is a state-of-the-art solution which implements down-sampling without losing any information. There

are few works design rotating masks in THz imaging, which increases cost but difficult to interface with current waveguide systems. Some literature uses random down-sampling pattern in laser-scanning and microwave imaging systems. However, there are many remaining issues. Firstly, the related literature did not mention how to deal with a down-sampling percentage when the sparsity K is unknown. Secondly, no on-line detection solutions in OEW NDT systems are observed. So feature extraction is possible only after the scanning. Jointly sensing-feature extraction design is more time-efficient.

(2) The sensing stage of traditional OEW NDT systems did not consider the needs of the latter feature extraction. For example, traditional OEW NDT systems sample large data amount, but if the interested feature only contains in a small part the obtained data, they will incur large processing overhead for the feature extraction process. Data compression protocols are the straightforward technical route to compress data, but data compression protocols compress data only after sampling. On the contrary, CS already demonstrates joint sensing-compression ability in many fields, which eliminates data compression hardware or the storage space need to perform compression protocols. According to the review, there are CS down-sampling instances in laser scanning systems and THz imaging systems. However, there is still no literature considering optimise the measurement data from the defect extraction side, i.e., what data is enough for preserving the feature for decision-making, only capturing these data is more time/storage/computation-efficient. How to capture and efficiently reconstruct these data is a key issue.

(3) Feature extraction algorithms for OEW NDT systems need to be robust and time-efficient. The traditional feature extraction procedure that imposed on the reconstructed full data is not time/storage-efficient, this kind of procedure brings benefit for sensing but no benefit for feature extraction. Robust feature extraction such as defect region segmentation from a complex background is also challenging. OEW NDT systems need to segment defect areas from the spatial reflection/transmission coefficients image. Some materials have a complex image background. For example, composite materials have a texture which interfering damage detection. Furthermore, there is an inevitable nonparallel between the specimen surface and the scanning plane, which causes variation in lift-off distance and makes some part of the spatial image has large values. According to the review, few works are using the difference of image from health sample and defect sample for damage localisation; they can

be used to segment the damage region in open-ended waveguide systems. However, they are not robust to complex image background such as texture. Traditional image segmentation methods also cannot properly address this issue. On the other hand, almost all CS solutions for NDT systems handle feature extraction from spatial data on the reconstructed full data according to the literature review. This is not time-efficient because the sparse reconstruction process is time-consuming. Efficient and robust damage region segmentation from complex image background is a key issue.

2.6 Chapter Summary

This chapter gives an overview of compressed sensing. The state-of-the-art of CS theory in sparse representation, measurement matrix design and sparse reconstruction algorithm are reviewed. NDT applications that use CS in their sensing and feature extraction stage are reviewed to get a state-of-the-art of how CS solve NDT problems. The key issues of applying CS in OEW NDT systems to address its critical challenges are highlighted from the review.

The following chapters will address these challenges and key issues accordingly. In summary, Chapter 3 develops on-line CS model to address the challenge of time-consuming data acquisition, which reduces the sampling time by one order of magnitude. Chapter 4 investigates a feature-supervised CS-based CS data acquisition to address the challenge of reserving interested features while reducing data, and efficiently reconstruct the interested data; Chapter 5 elaborates robust and time-efficient damage detection methods directly on CS data without reconstructing the full data. More details are discussed in each chapter respectively.

Chapter 3. On-line CS Model for Open-ended Waveguide NDT&E

This chapter proposes an on-line CS model to address the challenges of time-consuming data acquisition by raster scan in open-ended waveguide NDT systems. As highlighted in the last chapter, the sparsity K is a key parameter in many spare reconstruction algorithms, and it is used to guide the number of measurement. However, it is usually difficult to estimate K in practical applications when there is no enough training data. To achieve downsampling without knowing the sparsity K, the proposed on-line CS model implements accumulated sampling and recovery with a customised 0/1 Bernoulli measurement matrix by using historical sensing results to guide the on-going data acquisition. The measurement number is decided by the quality of the recovery data. Compared to traditional raster scan designs which require complete sampling to obtain all data, this model can obtain the whole data and defect information while the scanning is conducting, thus forming an on-line process. Furthermore, the proposed model does not require any hardware update, which is easy to implement. Damage region in the reconstructed image can be extracted using a proposed histogram threshold edge detection (HTED) algorithm. The experimental results in low-energy impact damage detection illustrate the time efficiency of the CS model and more accurate damage region segmentation using HTED. The proposed compressed sensing technique is attractive in quality control of CFRP production. This technique can also be applied to situations where the sampled data is partly lost. Dispensing with hardware updates incurs minimum disruption and also benefits cost control and improves productivity. The work in this chapter is published on IEEE Transactions on Industrial Electronics.

3.1 Problem Statement & Related Works

This section states the impact damage detection on CFRP materials and reviews related techniques (Not only CS methods) for it. CFRPs materials have a high strength-to-weight ratio, high modulus-to-weight ratio, good corrosion and fatigue resistance ability. These impressive mechanical properties make them attractive in numerous industrial fields, e.g. aerospace [132], medical science [133] and electric system [134]. However, due to the lack of through-thickness reinforcement, CFRPs are vulnerable to impact forces [135]. Impact forces can induce a wide variety of composites failure modes such as disbanding, micro-cracking and delamination. These damages put CFRP structures in safety risk, which calls for effective integrity testing and evaluation techniques. To this end, some non-destructive testing and evaluation techniques have been applied for investigating CFRPs impact damage, such as eddy current thermography [136, 137], X-ray [138], guided wave [139] and optical fibre bragg grating sensors [140]. Eddy current thermography is largely influenced by environmental temperature, and the polymer matrix in CFRPs is vulnerable to the heat-affected zone in thermography [141]. X-ray is hazardous while guided wave and optical fibre bragg techniques suffer from coupling and complex installation issues.

OEW NDT techniques are widely used for evaluation of CFRP structures [142-144]. Yang et al. [145] use 65~67GHz millimetre wave which successfully detected impact damage with 9J of impact energy on CFRP. Dong et al. [146] use terahertz frequency to detect a low-velocity impact on hybrid fibre-reinforced composite laminate. OEW NDT systems use raster scan to get the spatial-spectral reflection coefficients of CFRP. Reflection coefficients are affected by the angle between the electrical field vector direction of the electromagnetic wave and the carbon fibre direction in the CFRP surface. As CFRP is anisotropic material, when the angle is zero, reflection coefficients from with and without damage areas are easily distinguished. Furthermore, impact damages cause some change in material property of the damage area, which changes the intrinsic impedance of it as a result. The spatial image for different frequency frames is usually different due to the complex internal structure and skin effect. So, VNA works in a frequency-sweeping mode in order to get multiple frequency resonances and thus revealing the defects at certain frequencies, as shown in Figure 3.1.

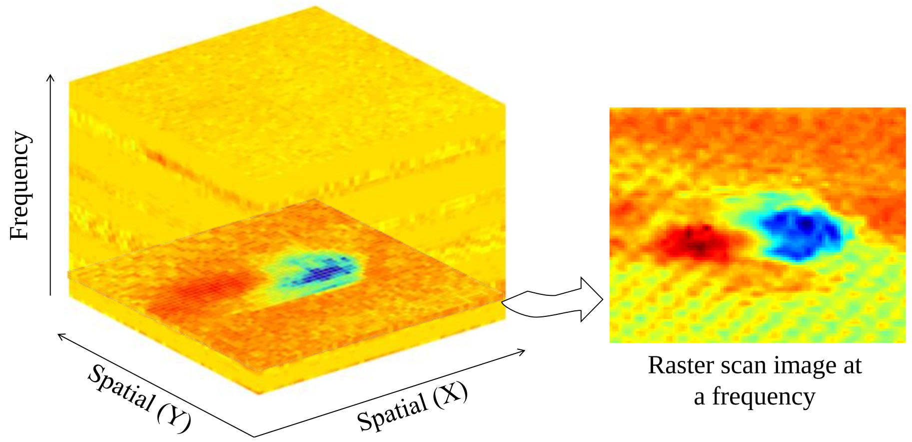

Figure 3.1 Demo of a dataset for impact damage detection with OEW NDT.

All these literature use raster scan to sample the RF reflectivity of all target area with certain step size. When the step size is small or the target scanning area is large, the raster scan process becomes very time-consuming. For example, Salski et al. [147] use printable RF inductive sensors which are operating on 10~300MHz to detect crack/delamination/voids in CFRPs based on raster scan. The number of measurement points in a single line of sensors is $N-1$, where N is the number of individual inductors per line. When using $N = 8$ RF inductive sensors on a single line and choosing 1 mm step size to scan 160×200 mm^2 area, about 4500 translations of the scanner are needed to acquire all 32000 measurement points, which will take about 30 minutes. To reduce this time, they point out that using a large array of sensors is helpful. S. Yuan et al. [148] use large-scale wireless impact monitoring sensors to localise the impact damage.

These hardware-based methods will increase the cost. Compressed sensing (CS) offers a possibility to reduce the acquisition points as shown in Chapter 2. CS is originally from medical applications where CS leads to less radiation exposure to patients, such as magnetic resonance imaging (MRI) [89, 149]. Inspired by CS application in MRI, some literature use compressed sensing for down-sampling in scanning systems as reviewed in section 2.5.1. However, they did not address the unknown sparsity K and the measurement number as a result. In addition, the afore-mentioned efforts are based on post-processing of sampled data, which is not efficient for an industrial process. This chapter proposes a CS-based on-line model for waveguide NDT systems with a case study of on-line and automatic evaluation of CFRP structures' integrity.

3.2 The Proposed On-line CS Model for Open-ended Waveguide NDT&E

A novel accumulated sampling & recovery process and an automatic impact damage region segmentation algorithm which enables on-line detection is proposed in this section. This model is more time-efficient than the damage detection process in traditional OEW imaging which detects damage after raster scan. The method keeps the sampling number as low as possible under the condition that the sparsity K is unknown. A stability detection method is also proposed to balance time efficiency and damage detection accuracy. The overall methodology diagram is shown in Figure 3.3 below.

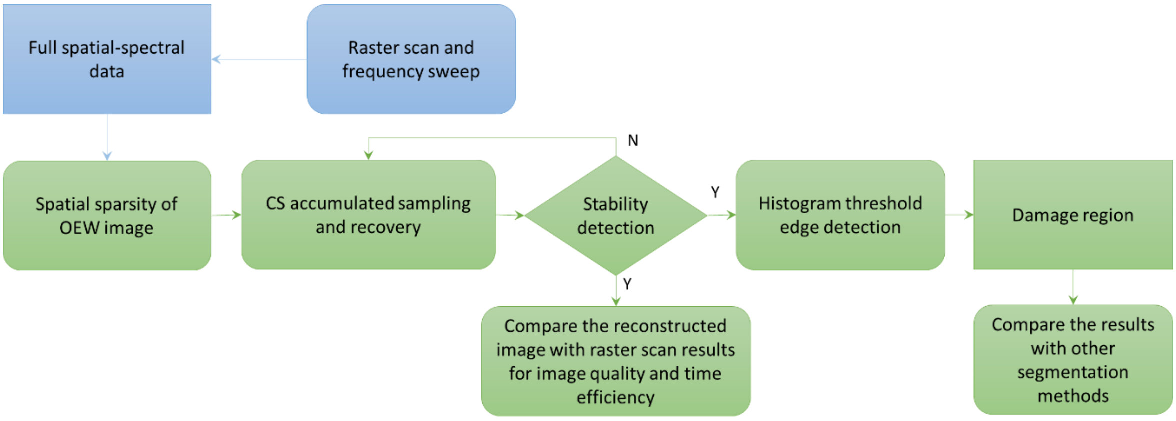

Figure 3.2 Methodology diagram for the proposed on-line CS model

Traditional method uses raster scan and frequency sweep to get the whole spatial-spectral data, as shown in the blue blocks. The proposed method performs sparse analysis firstly with the full spatial-spectral data. Then a 0/1 Bernoulli measurement matrix is proposed for accumulated sampling and recovery. More sampling percentage leads to better reconstruction image. When the sampling percentage is high enough, the recovered image tends to be stable, so a stability detection process is designed to judge if the sampling is stable. This stability detection block ensures that the system will not suffer from undersampling or oversampling, because when the sampled data is not enough for the latter processing, the system will keep sampling new data, and it stops once the stability condition is met. Defect region is segmented with a proposed histogram threshold edge detection algorithm when the recovered image is stable. For validation, the reconstructed images from the image recovery step are compared with the raster scan results. The damage region segmentation results are compared with other image segmentation methods. Alternatively, one can perform defect pattern detection after each reconstruction, which forms an on-line process. The details are discussed in the following sub-sections.

3.2.1 Sparsity analysis and CS accumulated sampling & recovery

The reflection coefficients from SUT can be mathematically modelled as a three-dimensional representation as $I\left(k_f,k_x,k_y\right)$, where $k_f, k_x, k_y \in \mathbb{Z}^+$ are the index for sweeping frequency and location in X and Y direction of the scan area. They have maximum value N_f, N_x, N_y respectively. For certain k_f, it degrades into a 2D form $\mathbf{I} \in \mathbb{R}^{+,\ N_x \times N_y}$, which can be represented as an image. Most of the image is smooth texture with a dominant low frequency. So the image is sparse in discrete cosine transform (DCT) domain. $\mathbf{I}$ is reshaped as a vector $\mathbf{i} \in \mathbb{R}^{+,\ n\times 1}$ (where $n = N_x N_y$) and represented as:

$$\mathbf{i} = \mathbf{\Psi}\mathbf{i}' \tag{3.1}$$

where $\mathbf{\Psi} \in \mathbb{R}^{n\times n}$ is the sparse basis and $\mathbf{i}'$ is sparse. Sparse representation is not the key concern for this Chapter, the commonly used sparse basis for images are DCT and DWT. This sparse representation lays the foundation for compressed sensing in open-ended waveguide NDT&E systems for CFRP impact damage detection.

Based on Equation (3.1), an accumulated 0/1-Bernoulli matrix $\mathbf{\Phi}_i \in \mathbb{B}^{m\times n}$ $(m \ll n)$ is generated to measure the reflection coefficients:

$$\begin{cases} \mathbf{y}_i = \mathbf{\Phi}_i \mathbf{\Psi}\mathbf{i}' + \boldsymbol{\xi}_i \\ \mathbf{\Phi}_{i+1} = \mathbf{\Phi}_i \vee \mathbf{\Phi}_\Delta \\ \mathbf{\Phi}_i \wedge \mathbf{\Phi}_\Delta = \mathbf{0}^{m\times n} \end{cases} \tag{3.2}$$

where $i \in \mathbb{Z}^+$, $\mathbf{y}_i \in \mathbb{R}^{+,\ m\times 1}$, $\mathbf{\Phi}_\Delta \in \mathbb{B}^{m\times n}$ is augmented measurement matrix, $\boldsymbol{\xi}_i \in \mathbb{R}^{m\times 1}$ is the Gaussian noise with zero mean and variance σ^2, $\mathbb{B}$ is binary space, '$\vee$' and '$\wedge$' are the logical *And* and *Or* respectively. Figure 3.3 gives a diagram representation of the CS accumulated sampling & recovery process.

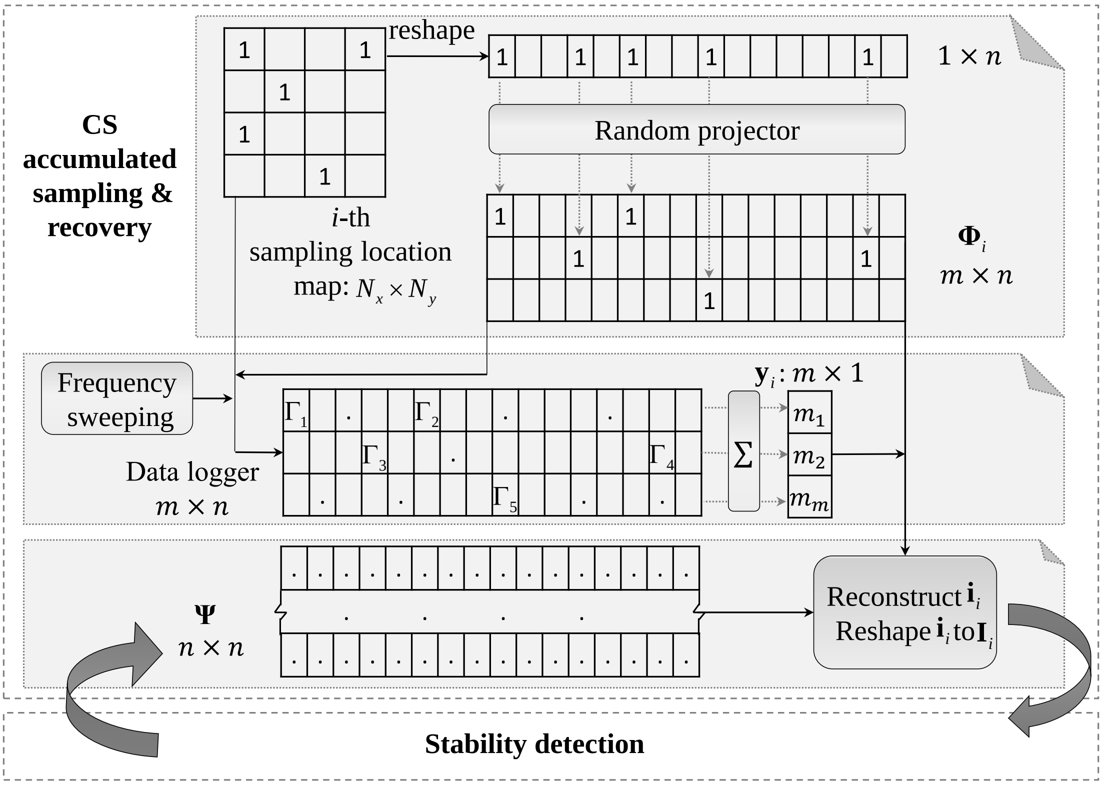

Figure 3.3 The diagram of CS accumulated sampling & recovery.

This sampling process starts from a sampling map with size $N_x \times N_y$, which has an initial percentage (e.g. 3%) of uniformly distributed '1'. The '1' in the map denotes the point should be sampled. Subsequently, the sampling maps is reshaped as a $1\times n$ vector and projected to the measurement matrix $\mathbf{\Phi}_i$ by a random projector. The random projector which implemented as Matlab code ensures that those '1' from sampling map randomly distributed on each row of $\mathbf{\Phi}_i$ to form a 0/1-Bernoulli matrix, it also makes sure that each row has at least one '1'. Then these sample data are saved to the data logger corresponding to $\mathbf{\Phi}_i$. Then data in data logger is accumulated by row to get the final measurement results for store, $\mathbf{y}_i$. Thus, the $N_x \times N_y$ reflection coefficients are compressed into $m\times 1$ CS measurements results.

Finally, this measurement results together with the measurement matrix and sparse basis ($\mathbf{\Psi}$) are used to reconstruct the whole reflection coefficients image by solving the problem in Equation (2.3). OMP algorithm is chosen for reconstruction due to its simplicity and fast convergence speed. The current reconstructed $\mathbf{i}_i$ are reshaped into a 2D image $\mathbf{I}_i$. If the current reconstructed image $\mathbf{I}_i$ cannot meet the stability requirement discussed in the next sub-section, this process will repeat until the requirement is met. For each new sampling and recovery iteration, an augmented measurement matrix ($\mathbf{\Phi}_\Delta$) which meets the condition $\mathbf{\Phi}_i \wedge \mathbf{\Phi}_\Delta = \mathbf{0}^{m\times n}$ and $\mathbf{\Phi}_{i+1} = \mathbf{\Phi}_i \vee \mathbf{\Phi}_\Delta$ is applied. $\mathbf{\Phi}_i \wedge \mathbf{\Phi}_\Delta = \mathbf{0}^{m\times n}$ means the sampling locations in new sampling map are different from any previous sampling location so that every new sampling iteration will get data from new locations. The random projector will also project the reshaped new sampling map into a new position in $\mathbf{\Phi}_i$. $\mathbf{\Phi}_{i+1} = \mathbf{\Phi}_i \vee \mathbf{\Phi}_\Delta$ means when reconstructing the image, all historical data are used. These constraints form an accumulated sampling and recovery process. For an extreme case, there is only one '1' in $\mathbf{\Phi}_\Delta$, which means every single sampling location will lead to a new reflection coefficients image.

Figure 3.4 gives pseudocode for generating a measurement matrix that satisfies Equation (3.2). The inputs are additive sampling percentage and the size of CS data and all pixel number. The output is the on-line measurement matrix and the corresponding sampling percentage. After some necessary initialisation, the online-Bernoulli measurement matrices are generated with an iteration process. The stop criteria is the stability detection result in the next sub-section. Figure 3.5 shows a demo of a measurement matrix and sampling map using this pseudocode, where the white pixels is the location to sample.

Algorithm: Generate online Bernoulli measurement matrix

Input: $0 < \Delta\rho < 1$: additive sampling percentage;
$m \in \mathbb{Z}^+$: number of measurement;
$n \in \mathbb{Z}^+$: length of signal.

Output: $\mathbf{\Phi} \in \mathbb{B}^{m \times n}$: The online Bernoulli meaturement matrix;
ρ: Current sampling percentage.

Initialization: $\rho = 0$, $\mathbf{\Phi} = \mathbf{0}^{m \times n}$;
$\mathbf{I}$ = Random permutate 1 to n;
$k = [n\Delta\rho]$, additive sampling number;
$i = 1$, iteration number;
while *stop criteria not satisfied* **do**
  $\Delta\mathbf{ColumnIndx} = \mathbf{I}(k(i-1)+1 \text{ to } ki)$;
  $\mathbf{\Delta RowIndx}$ = Random choose k number from 1 to m;
  $\mathbf{\Phi}(\mathbf{\Delta RowIndx}, \Delta\mathbf{ColumnIndx}) = 1$;
  $i = i + 1$;
end

Figure 3.4 Pseudocode to generate on-line 0/1 Bernoulli measurement matrix

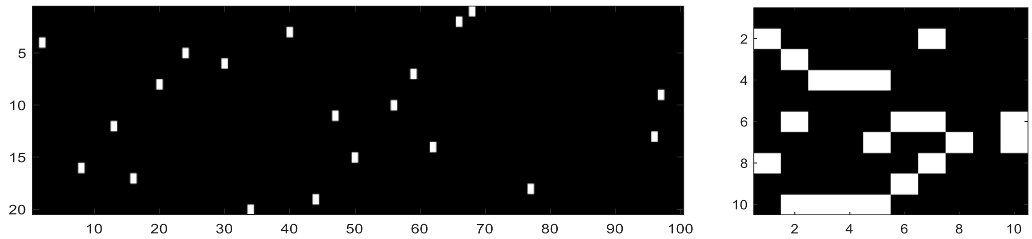

(a) (b)

Figure 3.5 A demo of (a) measurement matrix and (b) sampling map using the pseudocode. This demo considers a n =10×10 scanning grid and 20 sampling number. All the number on both axis are pixel index.

3.2.2 Stability detection

The diagram of stability detection is given in Figure 3.6. Noise perturbs the reconstructed images, which harms stability detection. So, edge-preserving filtering is used to reduce the recovery noise and thus to improve recovery stability.

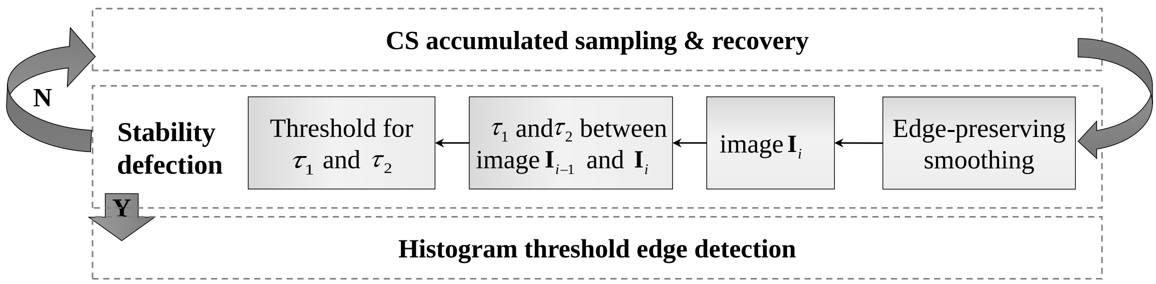

Figure 3.6 The diagram of stability detection.

Edge-preserving filtering is a technique to smooth images while preserving basic significant features like gradients, jumps, spikes, edges and boundaries. A bilateral filter is adopted here as introduced in detail in [150]:

$$\mathrm{BF}[I]_p = \frac{1}{W_p}\sum_{q\in\rho} g_{\sigma_s}\left(\|q-p\|\right) g_{\sigma_r}\left(f(q)-f(p)\right) f(q) \tag{3.3}$$

$$W_p = \sum_{q\in\rho} g_{\sigma_s}\left(\|q-p\|\right) g_{\sigma_r}\left(f(q)-f(p)\right) \tag{3.4}$$

where W_p shown in Equation (3.3) is the normalization factor; $g_{\sigma_x}(t)=\exp\left(-t^2/\left(2\sigma_x{}^2\right)\right)$ is the Gaussian weighting function; σ_s and σ_r denotes the standard deviation for the domain and range kernel, the behaviour of these two parameters are discussed in section 2.3 in [150]; *f*(.) and ρ denotes the signal and a discrete bounded set of pixels where the image signals are defined; *p*, *q* are pixel index.

After edge-preserving smoothing, normalised root mean square error (NRMSE, τ_1) and 2D correlation coefficient (τ_2) between consecutive reconstructed images are calculated to assess the stability of the recovered image, they are given by:

$$\tau_1 = \frac{\|\mathbf{I}_{i+1}-\mathbf{I}_i\|_{\ell_2}}{\|\mathbf{I}_i\|_{\ell_2}} \tag{3.5}$$

$$\tau_2 = \frac{\sum_p\sum_q \left\langle \mathbf{I}_A, \mathbf{I}_B \right\rangle}{\sqrt{\left(\sum_p\sum_q \mathbf{I}_A{}^2\right)\left(\sum_p\sum_q \mathbf{I}_B{}^2\right)}} \tag{3.6}$$

where $\mathbf{I}_A = \mathbf{I}_{i+1,pq} - \mathrm{E}\left[\mathbf{I}_{i+1}\right]$; $\mathbf{I}_B = \mathbf{I}_{i,pq} - \mathrm{E}\left[\mathbf{I}_i\right]$; $\mathrm{E}[\cdot]$ is mean value operator; *p*, *q* are the index of the two images. Both parameters are used here because they fail to distinguish different intensity and intensity distribution between images concurrently and individually. With the sampling percentage increasing, the recovered images tend to be stable, i.e. NRMSE tends to be 0, and 2D correlation coefficients tend to be 1. More sampling data contributes little to the reconstruction quality. The threshold can be set for both these parameters to judge whether the reconstructed image is stable enough.

3.2.3 Defect region segmentation with the proposed histogram threshold edge detection

Defect region is a feature widely used in NDT to quantitatively show the damage degree in composite materials [151-153]. Automatic defect detection improves efficiency in the industrial process. Detecting defect pattern is referred to as image segmentation in the image processing field. There are [154] threshold-based segmentation (e.g. Otsu's method and histogram-based methods [155]), edge-based segmentation like watershed techniques and Canny edge detection, etc. For defect pattern detection, authors in [6] propose an event-based automatic damage detection method for defects on metal. They use Monte Carlo approach to decide the threshold for a defect event. Their method cannot get the whole defect information before scanning all defect area. Besides, their method is useful in metal cracks localisation but not reliable and efficient in OEW NDT image of CFRP, because the CFRP images have woven texture and non-horizontal placement of specimen will cause a significant difference in the final image as our research in [156]. These features bring the idea of using texture filters [157] to extract the defect pattern in CFRP, but this method gives false detection in non-defect specimens easily. These techniques have their preferable application scene, which fails to address the characters of impact damage image from open-ended waveguide imaging systems.

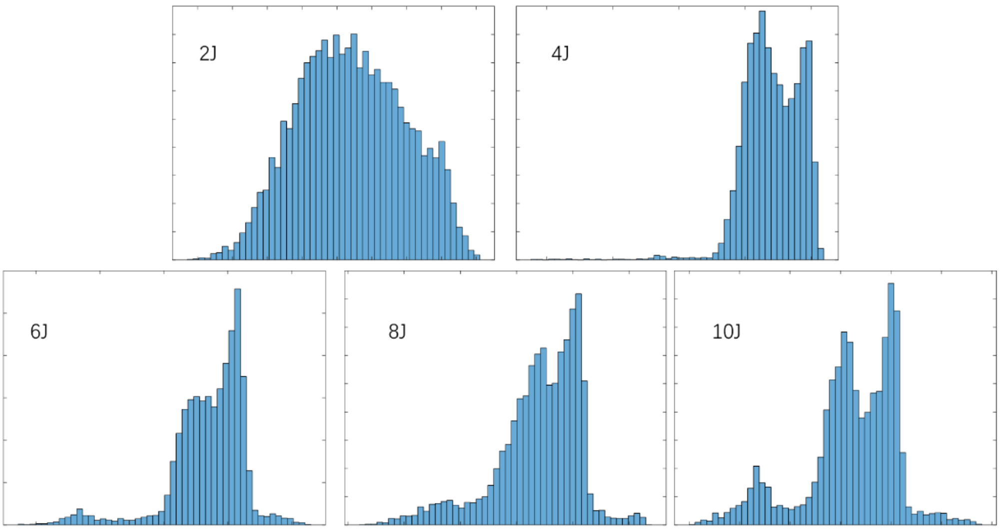

Figure 3.7 Histogram for impact damage image in Figure 3.14. The images from 4J to 10J specimens have long tails comparing to the 2J image, which can be used to extract the general defect pattern.

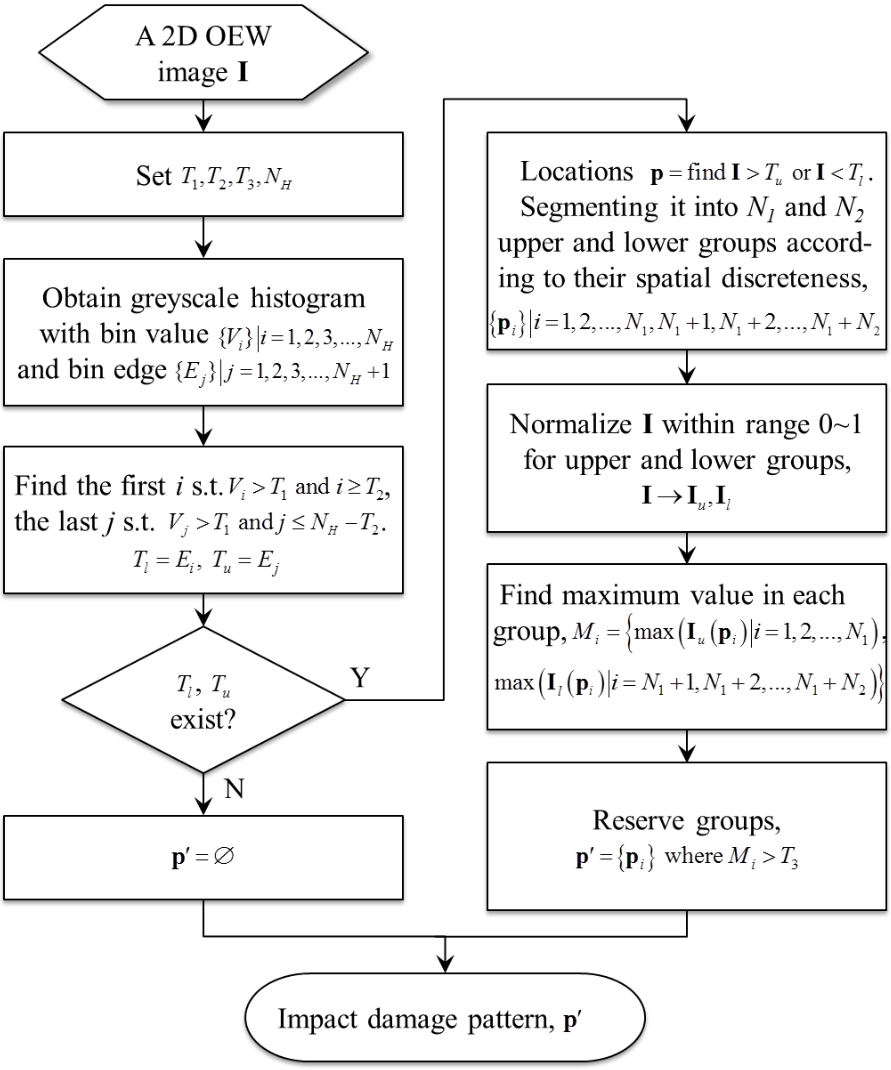

Figure 3.8 The proposed histogram threshold edge detection (HTED) algorithm

In this system, the amplitudes of reflection coefficients of the low impact energy defect area are different from the non-defect area, and the defect area only accounts for a small part of the total scanning area. These characters make the histogram right/left/bilateral long-tailed as shown in Figure 3.7, which enables using upper/lower/bilateral thresholds to get the general defect pattern.

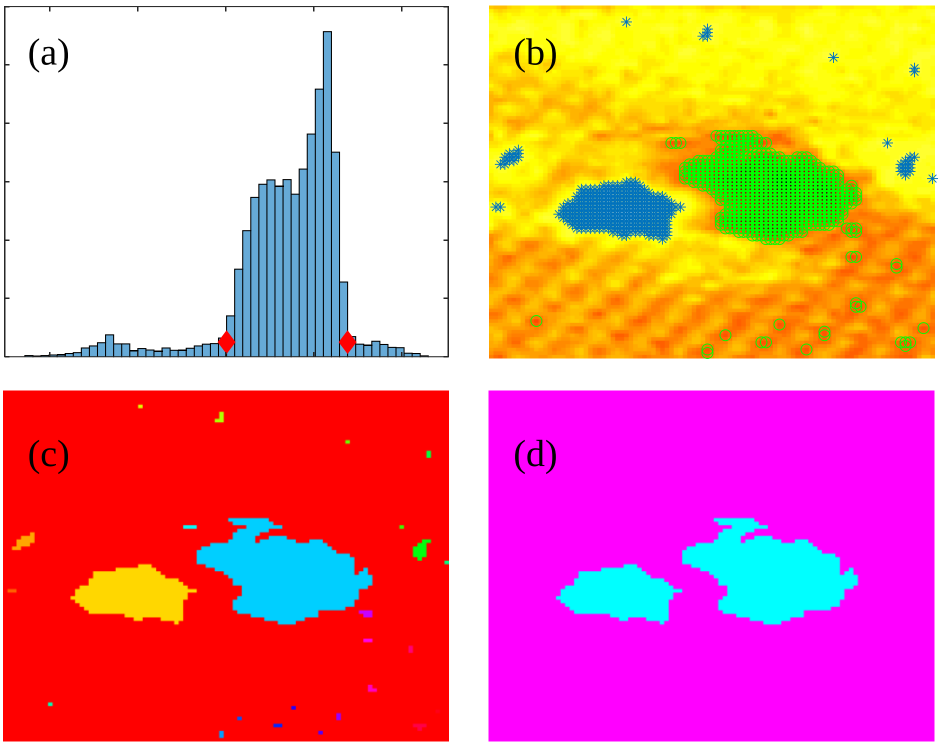

Figure 3.9 Results for HTED for the 6J image in Figure 3.14. (a) The threshold value; (b) The upper and lower threshold areas; (c) The clustered candidate defect pattern; (d) The final defect pattern.

Based on the characteristic of the histogram of defect image on CFRP materials, a computer vision-based algorithm called histogram threshold edge detection (HTED) is proposed to segment the damage region by detecting the damage edge and location. The proposed algorithm is shown in Figure 3.8. This algorithm automatically finds an upper threshold and a lower threshold in the intensity histogram, as shown in Figure 3.9(a). T_1 and T_2 are based on the defect area only account for a small part of the total scanning area. They can be set as a small fraction of the maximum bin value V_i and the bin number N_H respectively. These two thresholds together ensure extracting more detail of damage region but cannot distinguish the background texture/noise and damaged areas, as shown in Figure 3.9(b). So a clustering process is proposed to remove wrong candidates. All the candidate areas are clustered into the individual group as shown in Figure 3.9(c). Only the groups which have relatively large maximum value is reserved, which is controlled by T_3. As the maximum and minimum value in $\mathbf{I}$ are normalised to 1 respectively, T_3 can be a value which is slightly smaller than 1. Figure 3.9(d) shows the final extracted defect pattern, which reserves details for the defect pattern while robust to the texture background. These parameters can be optimised using training data.

3.3 Experimental Setup for Evaluating the On-line CS model

3.3.1 Hardware systems

The following hardware systems are used for validation. An open-ended rectangular waveguide (ORWG) probe with the dominant mode TE_{10} is used in this study. The probe has an inner dimension $a \times b$, where *a* and *b* are the longer edge and shorter edge respectively. The CFRP specimen is characterized by magnetic permeability (μ), electric permittivity (ε) and electrical conductivity (σ). d_0 is lift-off distance.

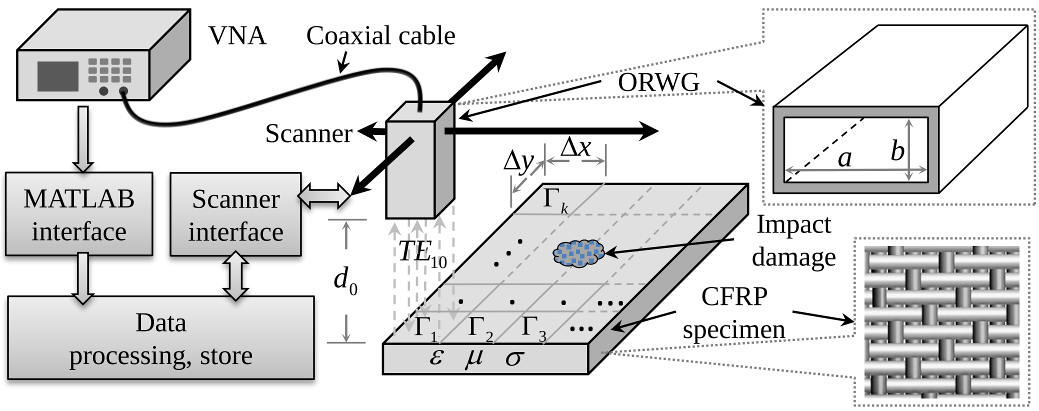

Figure 3.10 Diagram of the experimental system

The devices for the experimental system are shown in Figure 3.11. An X-Y scanner which carrying an ORWG probe is used to scan arbitrary point on specimens. The scanner scans random location according to the sampling map shown in Figure 3.11. The reflection coefficients are measured by vector network analyser (Agilent PNA E8363B) working in frequency-sweeping mode at different points in X-Y plane through a coaxial cable connected to the waveguide probe. The lift-off distance in Z direction keeps constant. MATLAB implementation of our algorithms together with a scanner and general purpose interface bus interface control synchronize probe location and measurement of VNA. Calibration is done for the VNA and the coaxial cable using a calibration kit (open, short and loaded) to compensate the cable characteristic and channel delay of the measurement results. The experiment parameters are shown in Table 3.1. The electromagnetic skin depth of CFRP at 100kHz is calculated to be 50mm in [158], which can be expanded to K-band using Equation (1.1).

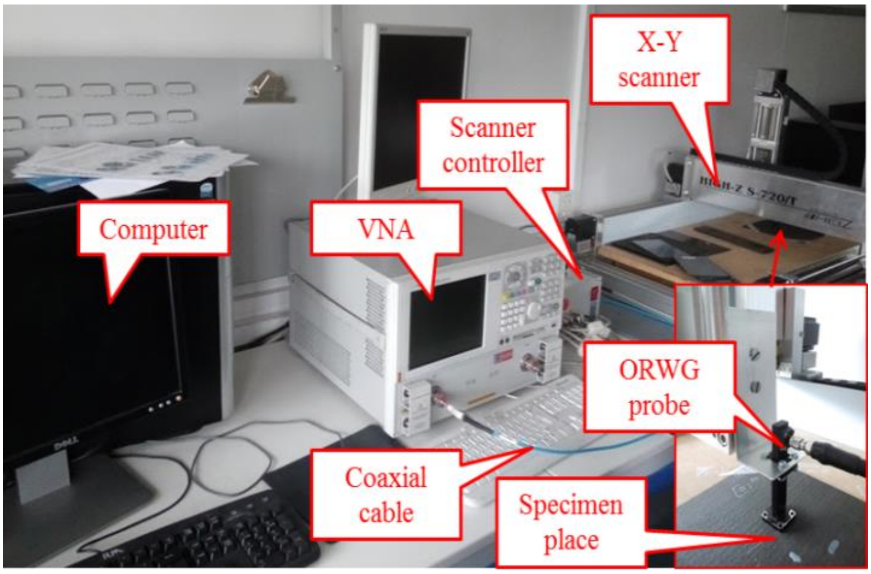

Figure 3.11 Devices for the experiment

Table 3.1 Parameters settings

Parameters	Value
Frequency band	18 GHz~26.5 GHz
Number of linear frequency points	1601
Scan area	30 mm × 30 mm around the impact point
$a \times b$	10.668 mm × 4.318 mm
W	2, 4, 6, 8 10 J
$\Delta x \times \Delta y$	0.3 mm × 0.3 mm
$f_{c,10}$	14.0607 GHz
d_0	1 mm
δ	0.971 ~ 0.118 mm

To validate the proposed method, the damage region needs to be covered in the scanning area. However, it is not necessary to scan the whole specimen in this validation, because the sparse property of the spatial image will not be influenced much by the size of the final image. This OEW imaging system emits same wave power for each scanning grid, and the distance from each scanning point to the probe keeps same, so the final image of received signal power should be smooth. This smooth property makes the image sparse in DCT domain, the size of image almost has no influence on the sparse property. Scan large area will take much more time as well and the impact point is known in this case. For these reasons, the scanning area is 30 mm × 30 mm around the impact point. The impact point can be found by using the white lines as shown in Figure 3.13. However, in practical applications where the potential damage area is not known, scanning the whole area is necessary. By using the proposed CS measurement method, it is much faster than the raster scan for the whole area.

3.3.2 Specimens

The CFRP specimens have 12 layers of 5H satin balanced carbon fibre woven fabrics as shown in Figure 3.10, manufactured by TenCate Advance Composites, Netherlands. The polymer matrix is made of polyphenylene sulphide and a thermoplastic resin system. Specimens are in a rectangular shape with a size of $100\times130\ mm^2$ and with $3.78\mp0.05\ mm$ of average thickness. Impact damages are created with different impact energy (W) by a free-fall hammer with mass $m = 2kg$ over the specimen centre from various height (h), as is shown in Figure 3.12. The hammer has a hemispherical bumper head with $20mm$ diameter. W is calculated by:

$$W = mgh \tag{3.7}$$

where g is the acceleration of gravity. Figure 3.13 shows five different specimens with various impact energy from 2J to 10J. Those scales on each specimen are used for deciding the impact point.

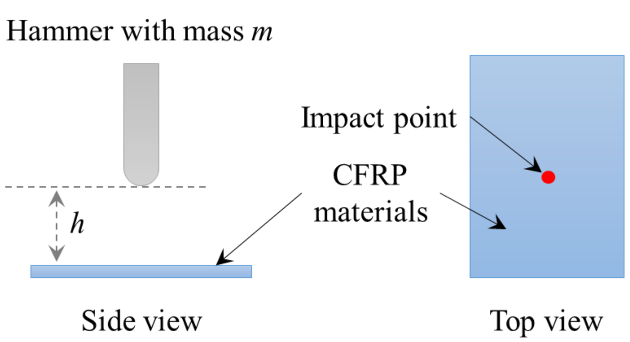

Figure 3.12 Schematic for generating impact damage on CFRP materials

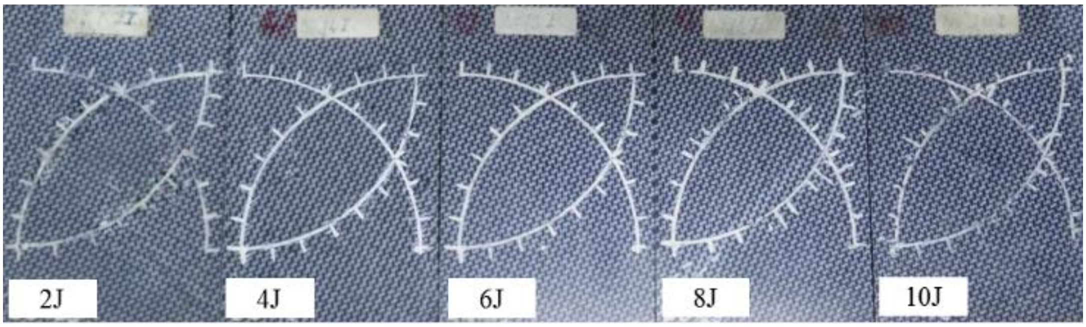

Figure 3.13 CFRP specimens under different impact energy. These damages caused by low impact energy are almost invisible, which may be evaluated as healthy using visual inspection. OEW NDT is capable of detecting such low impact energy damage.

Figure 3.14 shows the spatial images around the impact point obtained at 19.0041GHz with open-ended waveguide probe. Images for 4J, 6J, 8J, 10J specimens shows an obvious distortion in the centre, which indicates impact damage. The 2J specimen does not have significant distortion, which means that the 2J impact energy did not cause any damage or the damage fails to reveal in this method. The background of the image contains a texture pattern, which indicates the woven structure of specimens. Damage pattern in the 4J specimen looks differently from the 6J, 8J and 10J specimen, more repeat scanning to this area also shows a similar pattern. The reason may be that the 4J specimen suffers from other defect besides the 4J impact energy, or more likely, the 4J impact energy cases some disbanding just like the right side of the 10J specimen.

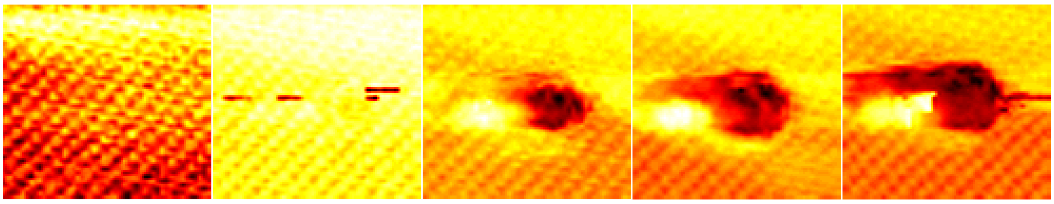

Figure 3.14 Raster scan results with open-ended waveguide NDT system. From left to right, 2J, 4J, 6J, 8J, 10J

Using the settings in Table 3.1, both N_x and N_y are 100. The total scanning location is $n = N_x N_y$. We reconstruct the whole image for every 3% of total locations. In a real application, if the reconstruct device is powerful enough, one can reconstruct the whole image for every single additional sampling location, which saves measurement time most. With the development of parallel reconstruction methods like [159] and Cloud computing as well as Super Computer, this becomes practical.

3.4 Evaluation Results

3.4.1 CS accumulated sampling and recovery results

In order to verify our sparse analysis, we apply DCT to the traditional raster scan image for specimens shown in Figure 3.14. Our previous study [156] indicates that the frequency frame with large standard deviation value can reveal the defects. We choose frequency 19.0041GHz which is the first lobe of standard deviation between all reflection coefficients that can reveal the defects.

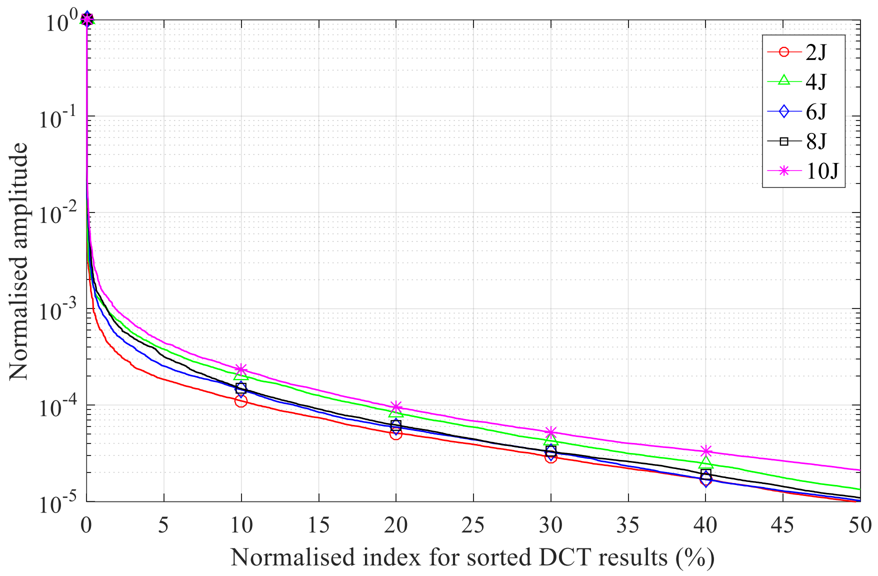

Figure 3.15 Normalised amplitude of sorted DCT results

The frequency components are normalised and sorted in descend order as shown in Figure 3.15. It is obvious that small percent of DCT results have dominant amplitude and the curve decays rapidly, which means the reflection coefficients are sparse in DCT domain.

After applying the accumulated sampling and recovery in Figure 3.8, the reconstruct results using OMP for different sampling percentage of different specimens at 19.0041GHz is shown in Figure 3.16. Only 3% of sampling percentage already reveals a general defect pattern in 6J to 10J specimens compared to the corresponding raster scan results in Figure 3.14. The reconstructed images with higher sampling percentage are more visually close to the raster scan results for all specimens, because more sampling percentage contains more information from the original image.

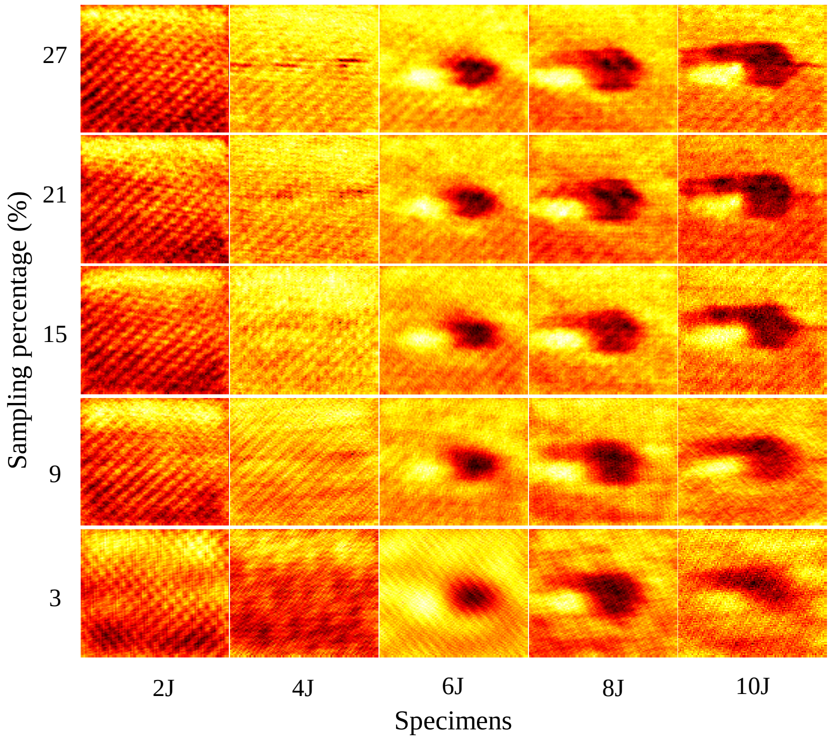

Figure 3.16 Recovery results under different sampling percentage for different specimens.

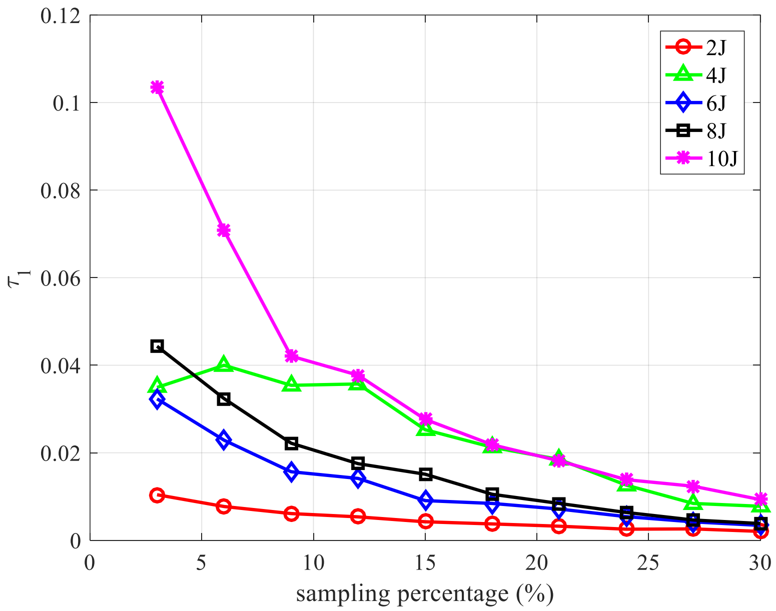

Figure 3.17 Average NRMSE between CS recovered images and raster scan images for different specimens.

The τ_1 and τ_2 between CS recovered images and raster scan image with 3% of step size are shown in Figure 3.17 and Figure 3.18 for quantitative analyse. It is the average results for multiple frequency points under the same specimens. The reconstructed images approach raster scan image with sampling percentage increasing. In a real application, the time for moving the waveguide probe from one location to another location is much less than getting reflection coefficients from N_f inquiry frequency, and frequency sweeping is necessary in order to find the frequency that can reveal the texture and defect. The curves order in Figure 3.17 generally the same as that in Figure 3.15, which coincides with a truth that higher sparse level needs less sampling data. The 4J specimen one alienated from others as shown in Figure 3.18. The reason is that the correlation coefficient is sensitive to intensity distribution. If the small defect area in 4J specimen located in a different location in the reconstructed image, the correlation coefficient will suffer greatly.

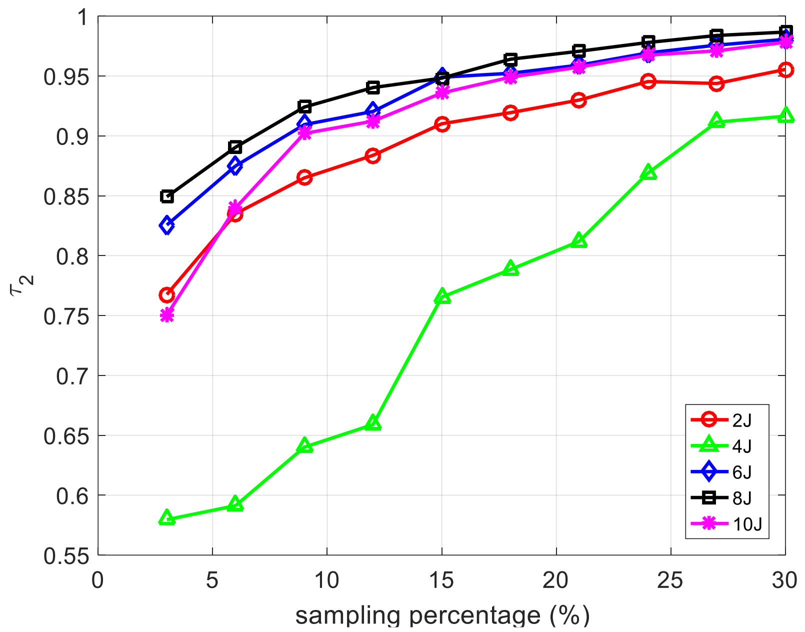

Figure 3.18 Average 2D correlation coefficients between CS recovered images and raster scan images for different specimens.

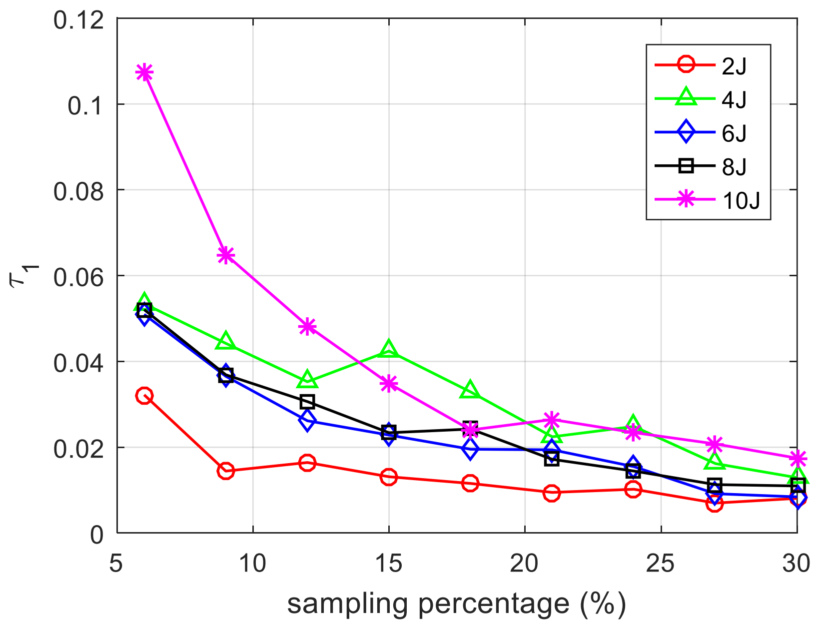

Figure 3.19 Average NRMSE between consecutive images for different specimens.

3.4.2 Stability detection results

According to the method in Figure 3.3, the NRMSE and 2D correlation coefficients between two consecutive recovered images for all specimens are shown in Figure 3.19 and Figure 3.20. With the sampling percentage increasing, the NRMSE is decreasing generally. By contrast, the 2D correlation coefficients are increasing. This means the reconstructed image becomes more stable. Setting threshold for τ_1 and τ_2 can judge the stability of recovery results. There is a trade-off between sampling time and the accuracy of damage pattern detection. Empirically, $\tau_1 \leq 0.02$ and $\tau_2 \gg 0.95$ is recommended in low impact energy damage detection.

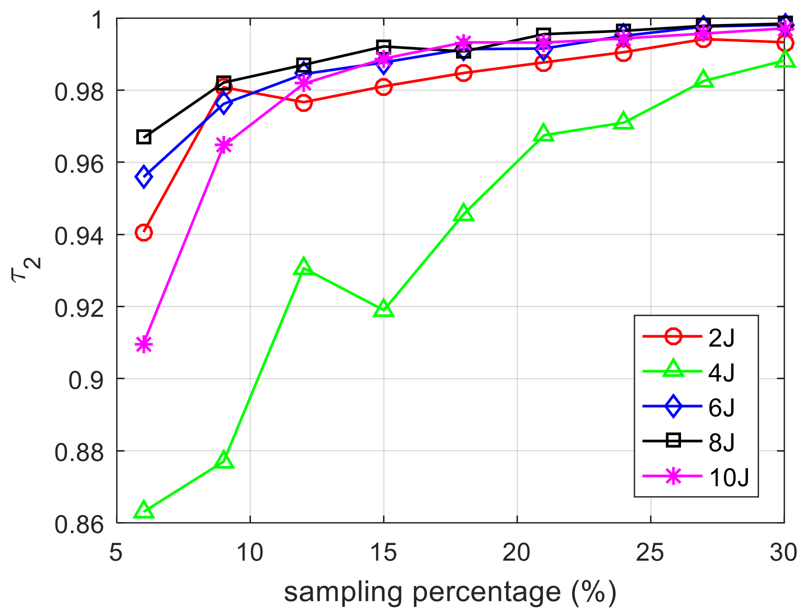

Figure 3.20 Average 2D correlation between consecutive images for different specimens.

3.4.3 Evaluation of defect region segmentation with the proposed HTED

This subsection shows the results for the proposed edge detection algorithm for automatic damage detection. The recovery results with 18% of sampling location are chosen as stabled results to perform our algorithm. We choose histogram bin number 50 in our study, and T_1 = 0.2max($\boldsymbol{V}_i$), T_2 = 6, T_3 = 0.7 in Figure 3.8. These parameters are not strictly so.

The damage pattern detection results for different detection techniques and specimens are shown in Figure 3.21. Otsu's threshold method and Canny edge detection method have good performance on large defect pattern, but response poorly for the small pattern. The watershed algorithm already shows over-segmentation problem and texture filter method fail to give solid defect area. The proposed method gives the most accurate defect pattern. For 2J specimen, there is no damage pattern revealed, but all other algorithms find the illusive texture. The first two rows in Figure 3.21 also compare the damage detection accuracy between CS recovery results with 18% of sampling percentage and raster scan results. The 18% sampling percentage one has approximately the same detected damage pattern as the raster scan one although missing some details. This means more than 80% of sampling time is saved. More sampling percentage leads to more accurate detection results, but the reconstruction time will suffer. The trade-off between them should be considered in a real application.

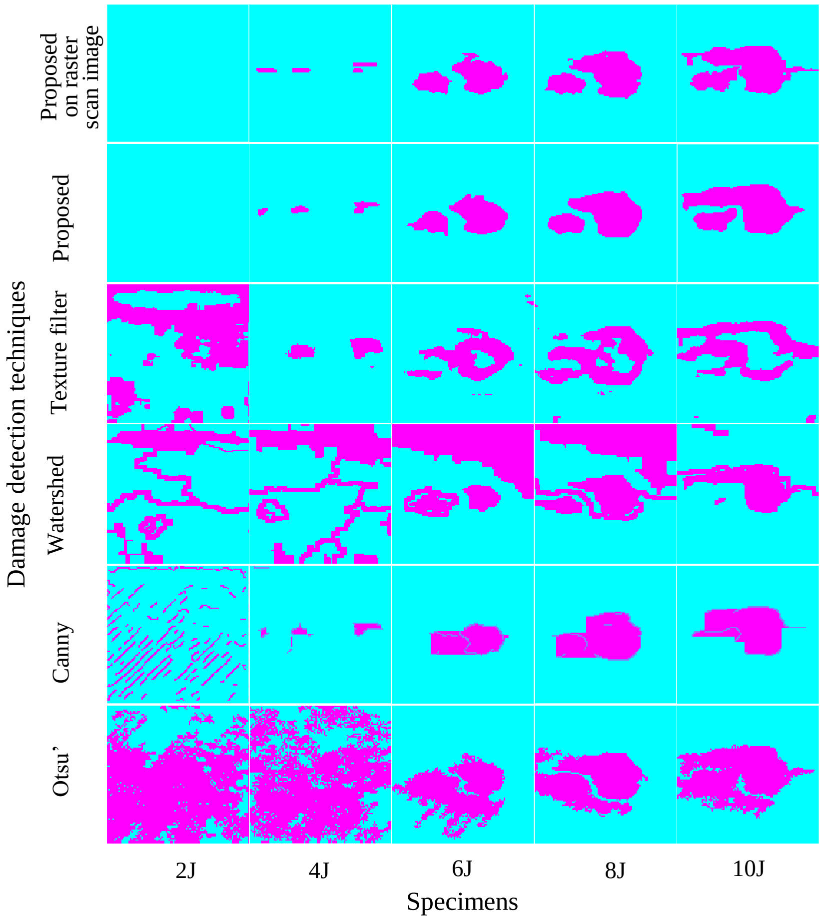

Figure 3.21 Damage pattern detection results for different detection techniques and specimens. All these techniques are performed using CS recovered results with 18% of sampling percentage except the first row, which is based on the raster scan image. The read pattern is the detected defect pattern.

Comparing with other works, this paper manages to detect impact damage with energy as low as 4J, lower than 9J which is reported in [145], thus achieving state-of-the-art detection level as reported using eddy current pulsed thermography [136]. More importantly, this framework is an on-line process, which means damage pattern detection is performed concurrently with data collection.

3.4.4 Evaluation of time-efficiency for the proposed CS method

The overall time-consumption consists of the probe moving time, frequency sweep time and delay time after moving the probe to make sure the probe already stable. For the proposed CS solution, it further includes measurement matrix generation time and reconstruction time. These time-consumption factors are denoted respectively in Table 3.2 below.

Table 3.2 Time-consumption factors

Notation	Description
t_p	Total probe moving time
t_f	frequency sweep time for each pixel
t_d	delay time after moving the probe
t_m	measurement matrix generation time
t_c	Sparse reconstruction time

For *n* sampling pixels, the raster scan time (T_R) can be denoted as:

$$T_R = t_p + n\left(t_f + t_d\right) \tag{3.8}$$

The CS methods time can be denoted as:

$$T_{CS} = t_p + m\left(t_f + t_d\right) + t_m + t_c \tag{3.9}$$

where *m* is the number of measurement for CS methods. t_c and t_m depends on the computation power and the software algorithms to implement it, they are relatively short when comparing to the raster scan. For example, recovery whole reflection coefficients using 18% of sampling percentage takes around 2 minutes on a Windows computer with Intel® Core™ i5-4690 CPU. This time is far less than raster scanning, which takes around 35 minutes. Besides, t_c and t_m keeps reducing with the development of cloud computing and supercomputer. As for t_p, the probe moving time for raster scan and CS methods are similar. Even if the CS methods only need to sample a part of the full image, the time for moving probe randomly in the image counteract the downsampling benefits. With the increase of *n*, the time complexity of CS methods comparing to raster scan are:

$$\frac{T_{CS}}{T_R} = o\left(\frac{m}{n}\right) \tag{3.10}$$

where m is much smaller than n. The scanning burden reduced to m/n of raster scan. For example, m/n =18% sampling percentage using CS method has approximately the same detected damage pattern as the raster scan in the case study in this chapter. This means around 80% of sampling time is saved.

3.5 Chapter Summary

This chapter develops an on-line CS model to offer faster data acquisition and reduce sampling data amount than the traditional raster scan in OEW NDT systems. A case study in impact damage detection for CFRP structure using open-ended rectangular waveguide probe is carried out for validation. The spatial images for CFRP specimens are sparse in DCT basis in the case study; a customised 0/1 Bernoulli measurement matrix is designed for downsampling under CS scenario based on this sparse condition. Orthogonal matching pursuit algorithm is used to reconstruct the full image with the downsampling data, DCT basis, and the designed measurement matrix. To address the issue of hard to determine the sampling pixel numbers that required for reconstruction, an accumulated sampling process is developed. The measurement number is decided by the quality of the reconstructed image. When the reconstructed image is stable enough, the defect pattern is extracted with the proposed histogram threshold edge detection (HTED) algorithm. One can perform defect detection for every accumulated sampling and recovery, which forms an on-line process. The case study shows that HTED algorithm is robust to texture and lift-off distance variation comparing to other image segmentation methods, and the data acquisition time and data amount is reduced to m/n of raster scan while maintaining equivalent image quality and defect region as that of the traditional raster scan. There are additional advantages for the proposed on-line CS model. Firstly, this is a software algorithm, which means no hardware update is needed for waveguide imaging system while improving scanning efficiency. Secondly, compressed sensing recovers the whole image with only a fraction of sparse samples, which makes this framework also applicable for situations where the sampled data is partially lost using a sparse representation, e.g., data recovery from fault nodes in large-scale sensor networks.

The proposed method has some limitations. It is worth noting that the image recovery process in the accumulated sampling & recovery block may take a relatively long time, although it is much faster than the raster scan. One the one hand, the development of cloud computing and supercomputer can address this shortage. On the other hand, new sampling model which reduces the reconstruction overhead is a more fundamental issue that improves computation power. Furthermore, the feature extraction is performed on the reconstructed data for this model, which leads to large data amount for feature extraction as what raster scan suffers. The next chapter develops CS models to speed up reconstruction processes for applications. Specifically, the next chapter will develop a feature-supervised CS model that considers the latter feature extraction process to reduces the data amount for feature extraction and efficiently reconstruct the data. The proposed stability detection method relies on the reconstructed image for each iteration, and it works as the stop rule for the accumulated sampling process. Investigating one way that can directly use the CS sampled data as input rather than the constructed image is a potential improvement for this method, because the repeat the reconstruction is a relatively time-consuming process. The proposed HTED algorithm is based on the histogram character (i.e. there is long tail in one or both side of the histogram) of the CFRP damage, so it is only applicable to cases where the damage region only accounts for a small part of the whole image, such as small crack detection and low energy impact damage detection.

Chapter 4. Feature-supervised CS Data Acquisition

The last chapter points out that develops new sensing model that considers the latter feature extraction process to reduces the data amount while reserving interested feature is necessary. This chapter proposes feature-supervised compressed sensing (FsCS) which involves feature extraction process to supervise the sensing process in waveguide imaging systems. Besides sparsity information of the spatial reflection coefficients, the feature extraction process becomes another constraint input to supervise measurement matrix design. Compared to traditional spatial-spectral sweep and compressed sensing solutions, only the data which can extract the interested features is sampled in FsCS. Furthermore, FsCS contains one aligned spatial-spectral sensing (ASSS) scheme which jointly reconstructs each block using their joint sparsity to speed up the recovery. The proposed scheme is validated in an open-ended waveguide imaging system for impact damage detection. The work in this chapter is submitted to IEEE Transactions on Instrumentation and Measurement.

4.1 Problem Statement

Open-ended waveguide NDT systems use spatial-spectral sweep to get spatial and spectral response of SUT. Figure 4.1 recalls the overall diagram of waveguide NDT systems. The waveguide probe emits microwaves to a pixel on the SUT and captures reflection signals. Multiple frequency responses are obtained with frequency sweep. Then the probe sweeps to the next pixel with spatial scanning. The obtained data can be represented as a 3D cube as shown in Figure 4.1. Each horizontal frame is a spatial reflection coefficients image that either using amplitude or phase, which can be used for non-destructive testing and evaluation. Each vertical frame for a pixel is the responses at different frequencies, which can be used for material characterization. As mentioned in the conclusion part of the last chapter, the proposed on-line CS model suffers from the problem of heavy reconstruction overhead. Because all frames in the sampling frequency band are sampled and reconstructed for feature extraction, which brings problems from both feature extraction and sampling perspective.

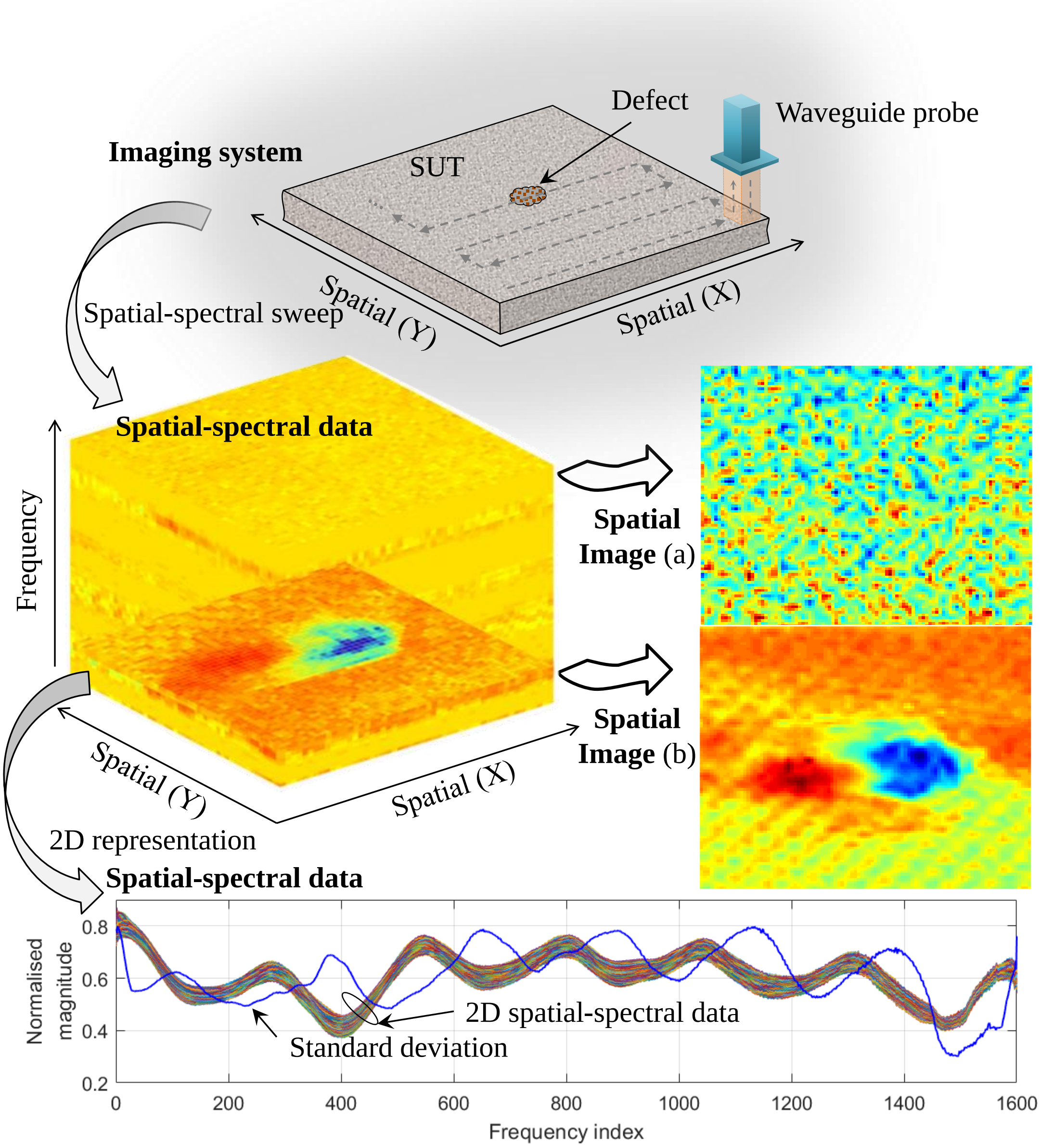

Figure 4.1 Diagram for open-ended waveguide NDT systems.

From the feature extraction point of view, the sampled data are usually highly redundant for feature extraction. As mentioned before, spatial images for different frequency frames are usually different due to the complex internal structure of SUT such as composite materials and skin effect. For example, spatial image (b) in Figure 4.1 reveals a significant difference in magnitude for some area while image (a) only shows a fuzzy image. The bottom part of Figure 4.1 shows the close-up presentation of the dataset. The multiple frequency reflections of each pixel are plotted as a line vs frequency index. In fact, only a small part of spatial-spectral blocks which have good contrast among spatial responses is suitable for feature extraction, the rest of the data are redundant. Pre-processing the data to find these blocks is a key step in the feature extraction process, which traditionally extracted by imposing operation like standard deviation to each frame on the whole frequency range. Spatial images that reveal defect is corresponding to high standard deviation value in this case as shown in Figure 4.1. Compressed sensing indicates that there is no need to sampling the part of data that will be finally discarded, which is one of the motivations for the work in this chapter.

From the sampling point of view, the CS model in the last chapter sequentially reconstructs each spatial image, which is a relatively time-consuming process. As shown in the bottom of Figure 4.1, the frequency response for spatial pixels are highly correlated, and neighbour spatial images are highly correlated as well. This correlation lays the foundation for the joint sparsity scenario, where correlated data can be jointly reconstructed to improve reconstruction speed.

4.2 Related Works

CS witnesses some application in reducing data amount in waveguide and microwave imaging systems. The last chapter [160] reduce the spatial sampling data in a waveguide NDT system based on a customised measurement matrix and discrete cosine basis. X. Yang et al. [161] show that 30% randomly under-sampled spatial pixels can get good images. H. Kajbaf et al. [162] also report 20% to 30% spatial pixels of the fully-sampled uniform measurements can reconstruct the image in synthetic aperture radar (SAR) systems. 3D SAR systems also reduce time cost and data in data acquisition [163]. Time-critical systems benefit from CS due to down-sampling. M. T. Bevacqua et al. [164] propose a CS-based method for 3D breast cancer microwave imaging, which reduces patient exposure to radiation. The measurement number/data of CS can be reduced to the order of sparse level normally. Besides reducing sampling time and data, CS also brings other benefits with proper sparse representation. S. H. Jung et al. [165] propose using CS in millimetre-wave SAR systems with reduced samples but obtained higher resolution. M. N. Stevanović et al. [166] devise a CS strategy to select the optimal orders to consider in the imaging procedure without needing any prior information on the perfect electric conducting target. B. Gao et al. [6] apply sparse representation in non-destructive defect detection in metals. There are also applications of CS in defect detection in other materials [108].

The above CS applications have common problems. The reconstruction process is time-expensive for frame-by-frame recover for the whole spatial-frequency data, although much faster than spatial-spectral sweep. To address these challenges, some papers explore the joint sparsity for situations where multiple signals have a same sparse pattern. Z. Du et al. [167] propose a model to adaptively control sparse level to simultaneously enforce all segments sharing a same active atom set. L. Wan et al. [168] use multimodal joint sparse representation to improve the performance of biometrics recognition. They represent the received data by a sparse linear combination of potential steering vectors while constraining the observations from different frequencies subject to sharing the same sparsity pattern. Similar multimodal joint sparse representation also applied in face recognition [169]. D. Bi et al. [170] investigate a multifrequency CS model for 2D near-field microwave SAR imaging system. Spatial data of each frequency are represented as a hierarchical tree structure under a wavelet basis, and spatial data of different frequencies are modelled as a joint structure. G. Xia et al. [171] propose a joint kernel sparse representation model, which uses a kernel-induced space with a geodesic exponential kernel for sparse representation. All these methods reduce sensing time and data amount by the downsampling ability of compressed sensing. However, they bring in substantial reconstruction burden in reconstructing the full data, and they did not take the feature extraction process into consideration.

There are few works on feature extraction-oriented sensing in other fields. X. Zhang et al. [172] design specific CS for moving-target imaging by exploiting the geometry information of the defocused results. Z. Du et al. [109] propose CS based impulsive feature detection for wind turbine systems. B. H. Chen et al. [173] propose a novel rain streak removal method that is based on error-optimized sparse representation. For microwave imaging systems, M. Cetin et al. [17] review the sparse representation in SAR imaging systems, but no literature offers joint sensing and feature extraction design.

4.3 The Proposed Feature-supervised CS Data Acquisition

The overall methodology diagram of this chapter is given in Figure 4.2. The traditional method uses raster scan with frequency sweep to acquire the full spatial-spectral data, however, most of the data are discarded when extracting the damage region. The last chapter proposes a method that samples a part of the spatial data, but the method also obtains the full spatial-spectral data by reconstruction. Instead of performing feature extraction in the whole reconstructed spatial-spectral data which involves a laborious reconstruction and feature extraction process as in traditional CS methods, this section proposes feature-supervised CS (FsCS) scheme to reduce the processing burden in feature extraction and reconstruction burden, and innovatively integrate the feature extraction process into the sensing process.

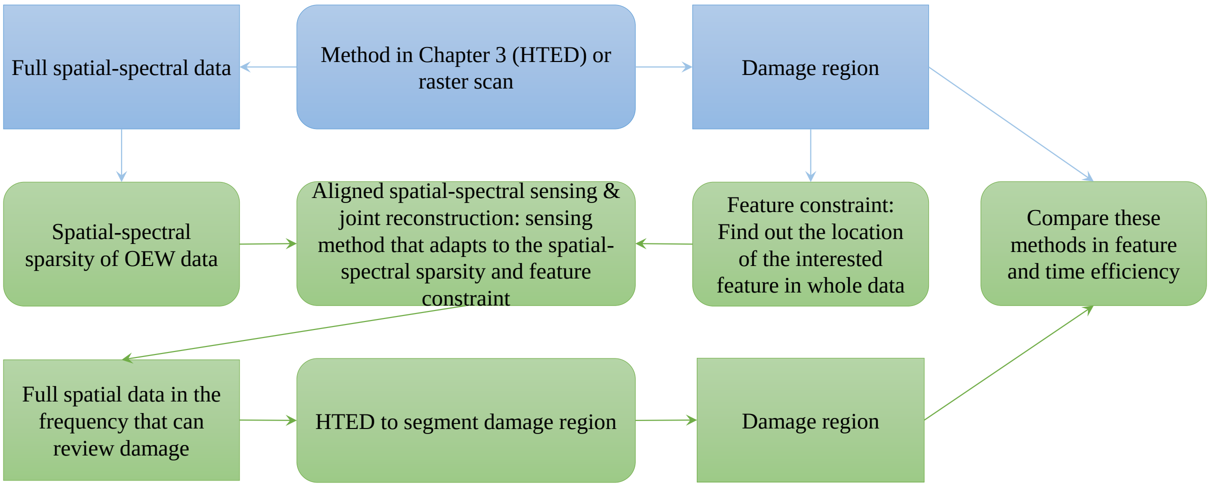

Figure 4.2 Methodology diagram for the proposed feature-supervised data acquisition

The proposed method uses the location of the damage region as a feature constraint to supervise sensing. Based on this feature constraint and the joint spatial-spectral sparsity of OEW data in this case study system, an aligned spatial-spectral sensing algorithm is designed. This sensing algorithm only obtains the spatial data in the frequency that can review the damage. The post feature extraction is greatly simplified and reduced data amount. This scheme is applicable to cases where features embedded in small segments of whole data. Taking time and storage efficiency into account, only acquiring these data is enough for feature extraction. For validation, the proposed method is compared with the traditional methods in terms of feature quality and time efficiency. More details are discussed in next subsections.

4.3.1 Spatial-spectral sparsity

This subsection explores the sparsity between neighbour frames and frequency response between pixels, aiming to sparsely represent them for joint reconstruction. As shown in Figure 4.1, the frequency sweep data of raster scan from waveguide NDT system is a 3D signal sampled from frequency/time/spatial domain, denoting as $\mathbf{\Gamma} \in \mathbb{R}^{Nx \times Ny \times n_f}$, which can be regarded as video on the frequency domain. There are n_f frames, and each frame is a 2D image with size $Nx \times Ny$. The data has 2D forms when reshaping each frame into a vector $\mathbf{i}_i \in \mathbb{R}^{n_s \times 1}$, where $n_s = NxNy$ and $i = 1,2,3,\ldots,n_f$. The individual spatial data $\mathbf{i}_i$ can be expanded on a more compact dictionary like discrete cosine transform (DCT) $\mathbf{D} \in \mathbb{R}^{n_s \times n_s}$ as $\mathbf{i}_i = \mathbf{D}\mathbf{s}_i$, where $\mathbf{s}_i \in \mathbb{R}^{n_s \times 1}$ are the sparse coefficients. Under such decomposition, neighbour frames usually have the same sparse patterns, i.e., they have the same non-zero positions but with different values. Denoting the measurement results for the individual frequency with measurement matrix $\mathbf{\Phi} \in \mathbb{R}^{m_s \times n_s}$ and some noise $\mathbf{n}_i$ as $\mathbf{y}_i = \mathbf{\Phi}\mathbf{D}\mathbf{s}_i + \mathbf{n}_i$, the whole measurement results for all frequency is

$$\mathbf{Y} = \mathbf{\Phi}\mathbf{D}\mathbf{S} + \mathbf{N} \tag{4.1}$$

where $\mathbf{Y} = \left[\mathbf{y}_1\ \mathbf{y}_2\ \mathbf{y}_3\ \cdots \mathbf{y}_{n_f}\right] \in \mathbb{R}^{m_s \times n_f}$ and $\mathbf{S} = \left[\mathbf{s}_1\ \mathbf{s}_2\ \mathbf{s}_3 \cdots\ \mathbf{s}_{n_f}\right] \in \mathbb{R}^{n_s \times n_f}$, $\mathbf{N}$ is the Gaussian noise term. Thus, $\mathbf{S}$ has some zero rows. Then we can seek the row-sparse matrix $\mathbf{S}$ by solving the following joint optimisation problem according to Equation (4.2):

$$\arg\min_{\mathbf{S}} \ \|\mathbf{S}\|_{\ell_{2,0}} + \lambda H\left(\mathbf{Y}, \mathbf{\Phi}\mathbf{D}\mathbf{S}\right) \tag{4.2}$$

When choosing $H\left(\mathbf{y}, \mathbf{A}\mathbf{s}\right) = \frac{1}{2}\|\mathbf{y} - \mathbf{A}\mathbf{x}\|_{\ell 2}$, the optimisation problem becomes:

$$\hat{\mathbf{S}} = \operatorname{argmin} \frac{1}{2}\sum_{i=1}^{n_f} \|\mathbf{y}_i - \mathbf{\Phi}\mathbf{D}\mathbf{s}_i\|_{\ell 2}^2 + \lambda_1 \|\mathbf{S}\|_{\ell 2,1} \tag{4.3}$$

where λ_1 including different subscript variant are Lagrange factor. After obtaining $\hat{\mathbf{S}}$, the data can be simply obtained by $\mathbf{\Gamma} = \mathbf{D}\mathbf{S}$. Likewise, the frequency response of each pixel can be sparsely represented as well. The overall process is the same as the above analysis, the only difference is that substituting n_f with n_s and switching n_s and n_f when they show together as an index.

The sparse dictionary can be found empirically or using all kinds of transform like DCT or discrete wavelet transform (DWT) or singular-value decomposition (SVD) on the training data. There are also some blind dictionary learning solutions [124]. The sparsity K can be found by thresholding the sorted absolute cumulate summation of decomposed coefficients on the corresponding sparse dictionary. The threshold can be 95% empirically, which means the largest K coefficients dominant 95% of total power. When there is no enough training data, the accumulated and recovery process in the last Chapter can be used.

4.3.2 Feature constraint for supervising data acquisition

As shown in Figure 4.3, traditional feature extraction processes impose data screening function (denote as $f(\cdot)$) on each frame $\mathbf{i}_i$ to obtain an indicator, then the frequency position that reveals damages (denote as $\mathbf{k}$) is extracted by thresholding the indicator values. Then the interested feature is extracted from the refined spatial-spectral data. The data screening process for each frame from $i = 1$ to $i = n_f$ can be denoted as

$$\sigma_i = f(\mathbf{i}_i) \tag{4.4}$$

$$\mathbf{k} = \varepsilon(\boldsymbol{\sigma} - \gamma_1) \tag{4.5}$$

where γ_1 is a threshold, greater γ_1 lead to less data. $\boldsymbol{\sigma} = \begin{bmatrix} \sigma_1 & \sigma_2 & \sigma_3 & \cdots & \sigma_{n_f} \end{bmatrix}$ is the corresponding feature data screening indicator for each frequency point. $\varepsilon(x) = \dfrac{d}{dx}\max\{x, 0\}$ is the unit step function. For traditional feature extraction, equation (4.4) is laborious when $\mathbf{i}_i$ is in large volume or $f(\cdot)$ is a very complex process.

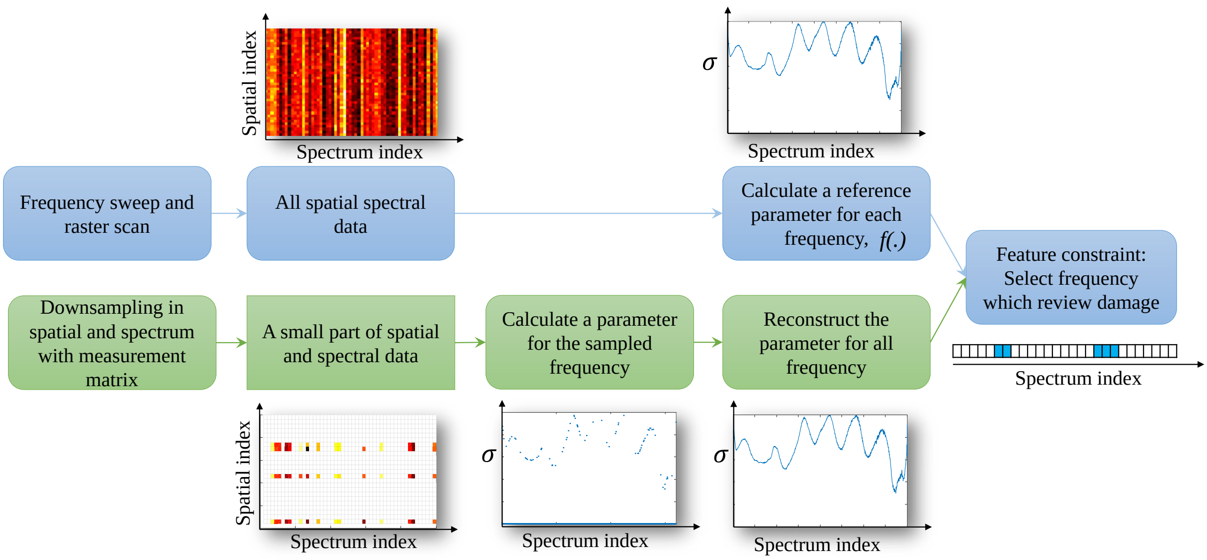

Figure 4.3 The diagram of feature constraint.

Instead of imposing Equation (4.4) on $\mathbf{i}_i$ for traditional feature extraction, this paper innovatively uses CS to reconstruct the feature data screening indicator. This is based on one fact that $\boldsymbol{\sigma}$ is usually sparse. For example, the standard deviation shown in Figure 4.1 is smooth that has dominant low-frequency components when decomposed with DCT. A downsampling block is introduced first for this purpose.

$$\mathbf{y} = \boldsymbol{\Phi}_f \boldsymbol{\sigma} \tag{4.6}$$

where $\boldsymbol{\Phi}_f \in \mathbb{B}^{m_f \times n_f}$ is the spectral measurement matrix, the detail generation process for this measurement matrix will be introduced in the next subsection. $\mathbf{y} \in \mathbb{R}^{m_f \times 1}$ is the measurement results. However, $\boldsymbol{\sigma}$ cannot be measured directly because it is not a physical parameter that can be measured. Alternatively, sample value can be used to estimate the population value according to statistic theory. For example, the sampling standard deviation can be used to estimate the population standard deviation by modifying the standard deviation formula from Equation (4.7) to Equation (4.8) to provide an unbiased estimation.

$$\sigma = \sqrt{\frac{1}{n_s}\sum_{i=1}^{n_s}\left(x_i - \mu\right)^2} \tag{4.7}$$

$$\sigma_s = \sqrt{\frac{1}{m_s - 1}\sum_{i=1}^{m_s}\left(x_i - \overline{x}\right)^2} \tag{4.8}$$

where m_s is the sample number on each spatial frame. μ and $\overline{x}$ are the population mean and sample mean respectively. So we can use Equation (4.10) to substitute Equation (4.6) by employing Equation (4.8) as $f(\cdot)$ and specially design the measurement matrix $\boldsymbol{\Phi}_\kappa$,

$$\boldsymbol{\Phi}_\kappa \quad \text{s.t.} \begin{cases} \boldsymbol{\Phi}_\kappa \in \mathbb{B}^{m_\kappa \times n_\kappa} \sim \mathrm{B}\left(1, p_\kappa\right),\ \kappa = \left\{s_1, f\right\} \\ \sum \forall \text{column of } \boldsymbol{\Phi}_\kappa < 2,\ \sum \forall \text{row of } \boldsymbol{\Phi}_\kappa = 1 \\ \mathrm{O}\left(K_\sigma \log n_f\right)/n_f \le m_f = \left\lfloor n_f p_f \right\rfloor \ll n_f \end{cases} \tag{4.9}$$

where p_κ is compression ratio. So, Equation (4.6) can be rewritten as

$$\begin{aligned}\mathbf{y} = \mathbf{\Phi}_f \boldsymbol{\sigma} &= \mathbf{\Phi}_f f\left(\mathbf{\Gamma}\right) \\ &= \mathbf{\Phi}_f f\left(\mathbf{\Phi}_{s1}\mathbf{\Gamma}\right) \\ &= f\left(\mathbf{\Phi}_f \left(\mathbf{\Phi}_{s1}\mathbf{\Gamma}\right)^T\right)\end{aligned} \tag{4.10}$$

The first two constraints in Equation (4.9) means that the p_κ percentage of '1' in $\mathbf{\Phi}_f$ and $\mathbf{\Phi}_{s1}$ are located in different rows and columns, which ensures that $\mathbf{\Phi}_{s1}\mathbf{\Gamma}$ is a sample of $\mathbf{\Gamma}$ without any scaling. It also ensures $\mathbf{\Phi}_f f\left(\mathbf{\Phi}_{s1}\mathbf{\Gamma}\right) = f\left(\mathbf{\Phi}_f \left(\mathbf{\Phi}_{s1}\mathbf{\Gamma}\right)^T\right)$. The last constraint offers successful reconstruction condition on $\boldsymbol{\sigma}$. m_f and δ can be empirically set in practical applications. m_s does not have such constraint because no spatial reconstruction is needed. The reconstruction problem for $\boldsymbol{\sigma}$ becomes

$$\hat{\boldsymbol{\sigma}} = \min_{\boldsymbol{\sigma}} \quad \left\|\boldsymbol{\sigma}\right\|_{\ell_0} \quad \text{s.t} \quad H\left(\mathbf{y}, \mathbf{\Phi}_f \boldsymbol{\sigma}\right) \le \gamma \tag{4.11}$$

The data which can reveal feature $\tilde{\mathbf{\Gamma}} \in \mathbb{R}^{n_s \times n_\sigma} \subset \mathbf{\Gamma}$ is the frequency location where Equation (4.5) has '1', n_σ is the number of these frequency locations.

The proposed feature data screening method only samples p_s subset of spatial pixels and p_f subset of their frequency responses and obtains the full feature data extraction indicator value, which will be used to supervise the sensing process.

4.3.3 Aligned spatial-spectral sensing that supervised by feature constraint

Based on the above modelling, an aligned spatial-spectral sensing (ASSS) scheme is proposed in Figure 4.4 to down-sample and jointly reconstruct the spectral-spatial responses which contain defect information. Besides the joint sparse information, feature constraint is another input for sensing. After the sampling, only a small part of spatial data in frequency axis that can review the damage are sensed and jointly reconstructed. The reconstructed data are used to segment the damage region.

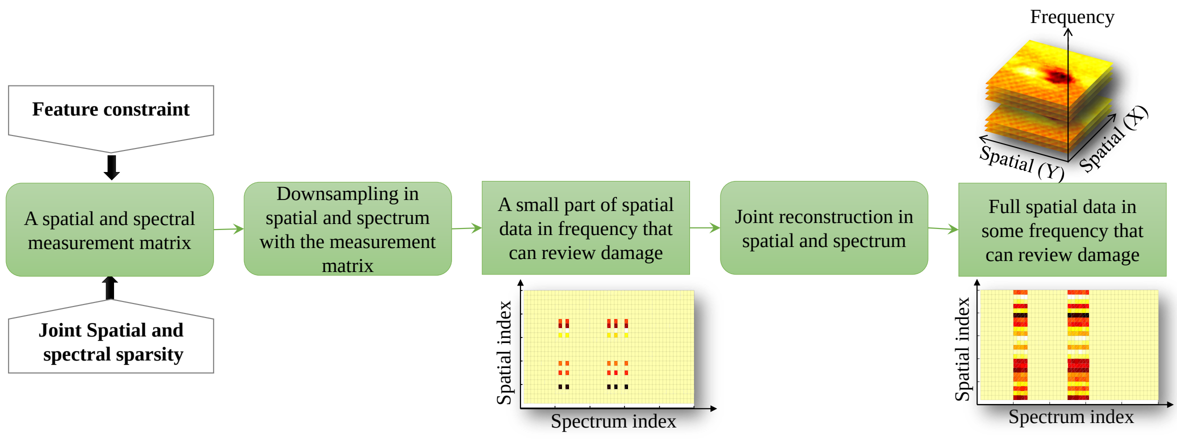

Figure 4.4 The diagram of aligned spatial-spectral sensing.

Figure 4.5 gives the process in a more rigid way. The inputs are the feature constraint (denote as **k**) obtained in the feature constraint subsection. It defines the specific sensing range which has the feature information and influences the dimension of $\mathbf{\Phi}_\zeta$. K_ζ and $\mathbf{D}_\zeta$ are obtained in the spatial-spectral sparsity section. Compression ratio is the last input which is defined by the user. It is worth noting that n_σ / n_f of data compression ratio already achieved using the feature constraint.

Two measurement matrices $\mathbf{\Phi}_\zeta$ obeying 0/1 Bernoulli distribution for spatial and spectral sampling is designed in the first three steps under the feature constraint. Firstly, m_ζ should be greater than the sparse level K_ζ for successful reconstruction. The sampling location which denotes as '1' in the measurement matrix can be implemented by randomly choosing m_ζ values from 1 to n_ζ. The sampled locations are randomly distributed to each line of the measurement matrix with the random column and row index. This design ensures that the there is no blank data in the measurement results. Each column has one '1' at most which eliminate duplicate sampling. This design can be used to design the measurement matrix in Equation (4.10) as well, because it ensures that the sampling results are a subset of the original signal without any scaling. The on-line measurement matrix generation process in Figure 3.4 can be used for implementation.

Algorithm Aligned spatial-spectrum sampling (ASSS)

Input: Spatial and spectrum measurement matrix, $\mathbf{\Phi}_\zeta$, $\zeta = \{s, \sigma\}$. And it have the following constraint,

$$\begin{cases} \mathbf{\Phi}_\zeta \in \mathbb{B}^{m_\zeta \times n_\zeta} \sim \mathrm{B}(1, p_\zeta) \ \text{ s.t. } \sum(\forall \text{column of } \mathbf{\Phi}_\zeta) < 2 \\ \mathrm{O}(K_\zeta \log n_\zeta)/n_\zeta \leq m_\zeta = \lfloor n_\zeta p_\zeta \rfloor \ll n_\zeta \end{cases}$$

where $\mathbb{B}$ is binary space, $\mathrm{B}(1, p_\zeta)$ is 0/1-Bernoulli distribution. p_ζ and K_ζ are the normalized sampling percentage and sparsity in spatial and spectrum domain, respectively.

1: Measurement: $\mathbf{Y} = \mathbf{\Phi}_\sigma(\mathbf{\Phi}_s\mathbf{\Gamma})^{\mathrm{T}} + \mathbf{N}$, where $\mathbf{\Gamma}$ is the unknown signal, $\mathbf{N}$ is Gaussian white noise.

2: Spectrum reconstruction, $\hat{\mathbf{S}}_\sigma = \operatorname{argmin} \frac{1}{2} \sum_{i=1}^{m_s} \left\| \mathbf{Y}_i - \mathbf{\Phi}_\sigma \mathbf{D}_\sigma \hat{\mathbf{S}}_{\sigma,i} \right\|_{\ell 2}^2 + \lambda_1 \left\| \hat{\mathbf{S}}_\sigma \right\|_{\ell 2,1}$

3: Virtual measurement in spatial, $\mathbf{Y}_s = \mathbf{\Phi}_s \mathbf{\Gamma} = \left(\mathbf{D}_\sigma \hat{\mathbf{S}}_\sigma\right)^{\mathrm{T}} = \mathbf{\Phi}_s \mathbf{D}_s \mathbf{S}_s$

4: Spatial reconstruction for neighbor frames, $\left\{\hat{\mathbf{S}}_k\right\}_{k=1}^{n_\sigma/d} = \operatorname{argmin} \frac{1}{2} \sum_{i=k}^{k+d} \left\| \mathbf{Y}_{s,i} - \mathbf{\Phi}_s \mathbf{D}_s \hat{\mathbf{S}}_{k,i} \right\|_{\ell 2}^2 + \lambda_2 \left\| \hat{\mathbf{S}}_k \right\|_{\ell 2,1}$, where $n_\sigma/d \in \mathbb{Z}^+$, $d \in \mathbb{Z}^+$ is the number of neighbor frames.

5: $\mathbf{S} = \left[\hat{\mathbf{S}}_k\right]_{k=1}^{n_\sigma/d}$, $\mathbf{\Gamma} = \mathbf{D}_s \mathbf{S}$

Output: $\mathbf{\Gamma}$

Figure 4.5 The proposed ASSS algorithm

OEW NDT systems get $m_\sigma \times m_s$ observation in spectral and spatial domain with $\mathbf{\Phi}_\zeta$. All sampling locations are aligned, i.e., all frames have the same spatial sampling location and all sampled pixels have the same frequency location. This aligned scheme brings some critical advantages. Firstly, each sampled pixel obtains most frequency sampling points, and each sampled frequency point obtains most pixel values, thus ensuring high-quality reconstruction for the sampled location and all spatial-frequency data as a result. Secondly, different frames or pixels can share the same measurement matrix, which is easy for hardware and software implementation. Lastly, sharing the same measurement matrix reduces the storage space when saving measurement matrix for reconstruction.

The whole frequency response of sampled pixels can be jointly reconstructed using methods like OMP. After the spectral reconstruction, the reconstructed full frequency response for sampled pixels fills the unsampled frames on the spatial domain, which works as a virtual measurement process. All frames have sampled data, and these data are in the same location for each frame due to the aligned property. As for the spatial reconstruction, the *d* neighbour frames are segmented into the same block which can be jointly reconstructed. This block-by-block joint reconstruction manner dramatically reduces the reconstruction burden. All interested frames can be reconstructed in a shifting manner and concatenating the results.

4.4 Experimental Setup for Evaluating Feature-supervised CS Data Acquisition

FsCS needs to randomly sample in spatial and sample interested frequency range. For random spatial sampling, OEW NDT systems can use an X-Y scanner to locate the probe at arbitrary pixels as shown in Figure 4.1. There is also other specially designed hardware for CS that makes use of spatial masks rather than mechanical scan [45, 120]. For spectral sampling, the progression in direct digital frequency synthesiser (DDFS) provides fast and reliable arbitrary frequencies output. Modern VNAs use frequency synthesiser gradually. Likewise, there are designs like frequency masks or even spatial-frequency masks [48, 174]. The computationally intensive reconstruction process for large spatial area can go to the more powerful computational centre like cloud computing, which fits with the IoT structures [4].

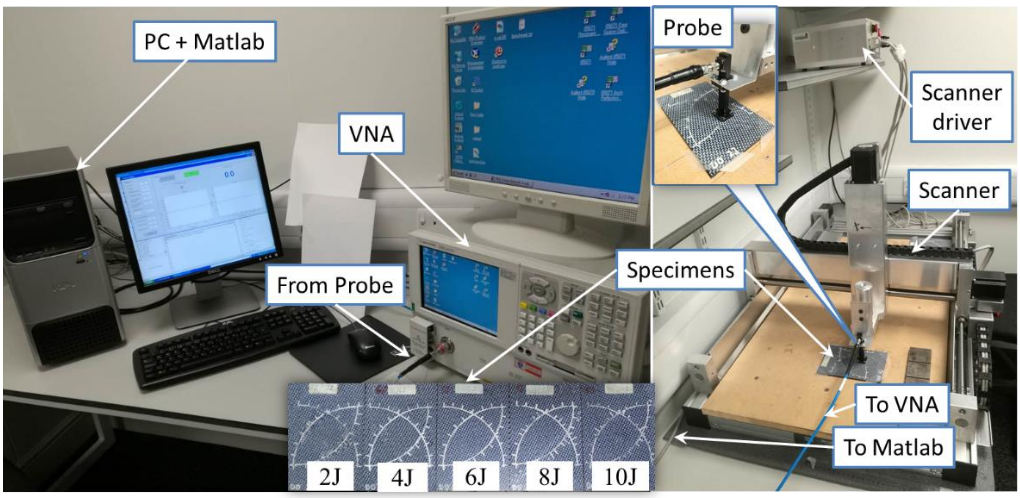

Figure 4.6 System setup for the proposed algorithms

This chapter validates the proposed algorithms in an open-ended waveguide imaging system in our lab experiment as shown in Figure 4.1 and Figure 4.6. A mechanical scanner which carries an open-ended rectangular waveguide probe is used to measure an arbitrary point on specimens. The measure location depends on the measurement matrix. A vector network analyser (Agilent PNA E8363B) is connected to the waveguide probe to emit and measure the microwave. Matlab is used to control the network analyser and mechanical scanner through the GPIB interface, which can cope with both random spatial sampling and random spectral sampling. The reconstruction process is done on a personal computer with Intel i5 4690K CPU and 8GB memory. During the reconstruction process, orthogonal matching pursuit (OMP) is used for feature constraint indicator reconstruction and joint reconstruction. Same specimens as in the last chapter are used as SUT. The SUTs are six carbon fibre reinforced polymers (CFRPs) with different impact damage in the centre part. Each specimen is scanned with raster scan and frequency sweep (spatial-spectral sweep) scheme for 20 times with slightly different scan area thus getting enough training data to get the sparsity K. The probe scans 99×99 pixels in each scanning. The frequency band is 18GHz to 26.5GHz with 1601 frequency points.

4.5 Evaluation Results

4.5.1 The joint sparsity of the dataset

This section validates the joint sparsity of the dataset obtained in the last section in spatial and frequency domain. The joint sparsity in the frequency domain is evaluated first. The spectral data are smooth wave shape curves, which is sparse when decomposing on DCT basis. Figure 4.7 presents the spectral data and DCT coefficients of pixel no. 1 in 6J specimen. The dominant DCT coefficients are in the beginning part. The zoom-in part shows the first coefficient is around ten times larger than all other coefficients, which presents high sparse. For more general cases, the sorted average DCT coefficients for all dataset are given in Figure 4.8. The data from all specimen shows a sharp decrease at the beginning. The largest DCT coefficients are around 1000 times larger than the 50th largest coefficient for all these curves, which means all the spectrum data are sparse in DCT basis. To get a vision of joint frequency sparsity, the spectral data and DCT coefficients for two pixels in the 6J specimen are given in Figure 4.9. It is obvious that the two different spectral data shows the same index for dominant coefficients and with different values, which is joint sparse. For more general cases, the probability of the first 30 DCT coefficients index is in the most significant 30 coefficients for the dataset is presented in Figure 4.10. The probability is obtained by finding the most significant 30 coefficients for all dataset and keep down their index, followed by counting the number of each index. The figure shows that the most significant 30 coefficients mainly located at the beginning of DCT coefficients, i.e. the dominant coefficients are located almost in the same coefficients index. Furthermore, the probability of sharing the same sparse coefficients index for the largest N_m

coefficients are given in Table 4.1 to present joint sparsity level. This probability is obtained by counting the number of same coefficients index out of the N_m largest coefficients for arbitrary pair of pixels. Figure 4.10 is the case when N_m=30, other cases for N_m=20, 50,100 are shown in the table. The most significant 20 DCT coefficients have 99.36% probability in sharing the same sparse index, the probability is around 86% even extending to the largest 100 coefficients which prove the joint sparsity.

(a)

(b)

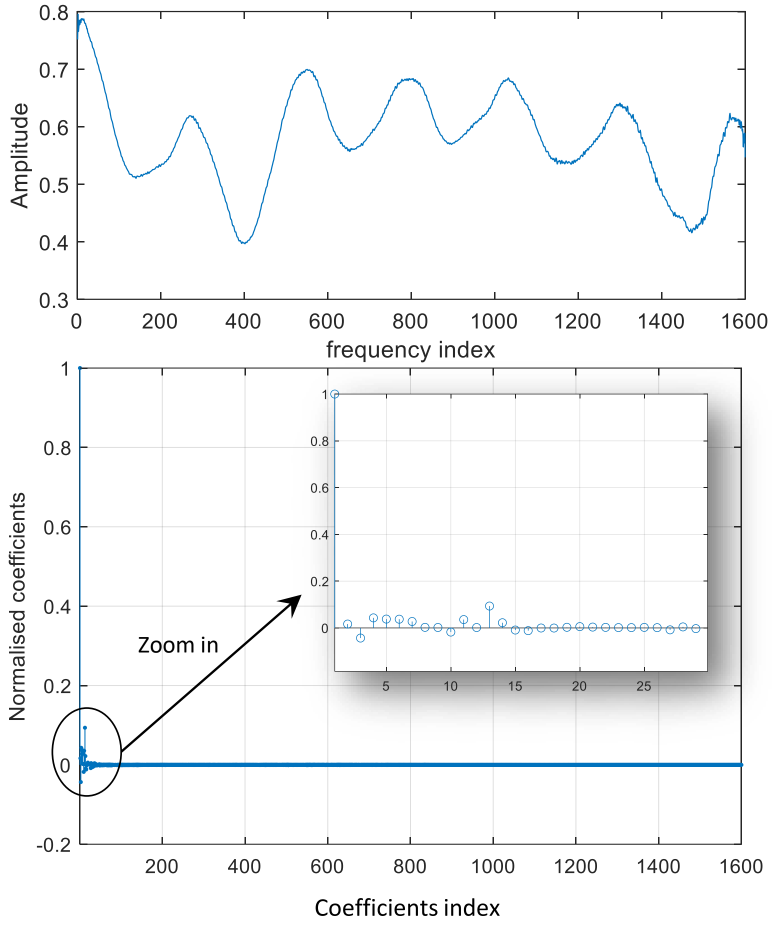

Figure 4.7 The DCT coefficients of the spectral data pixels. (a) The spectral data; (b) the DCT coefficients

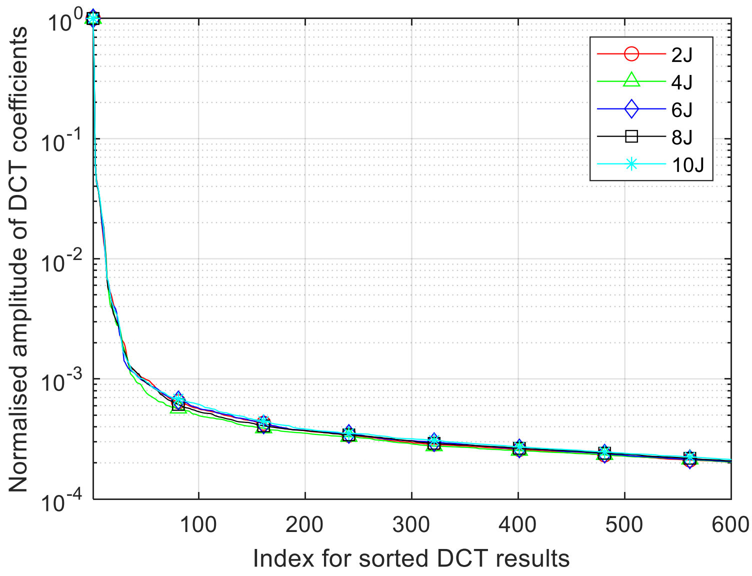

Figure 4.8 The average DCT coefficients of spectral data for the different specimen.

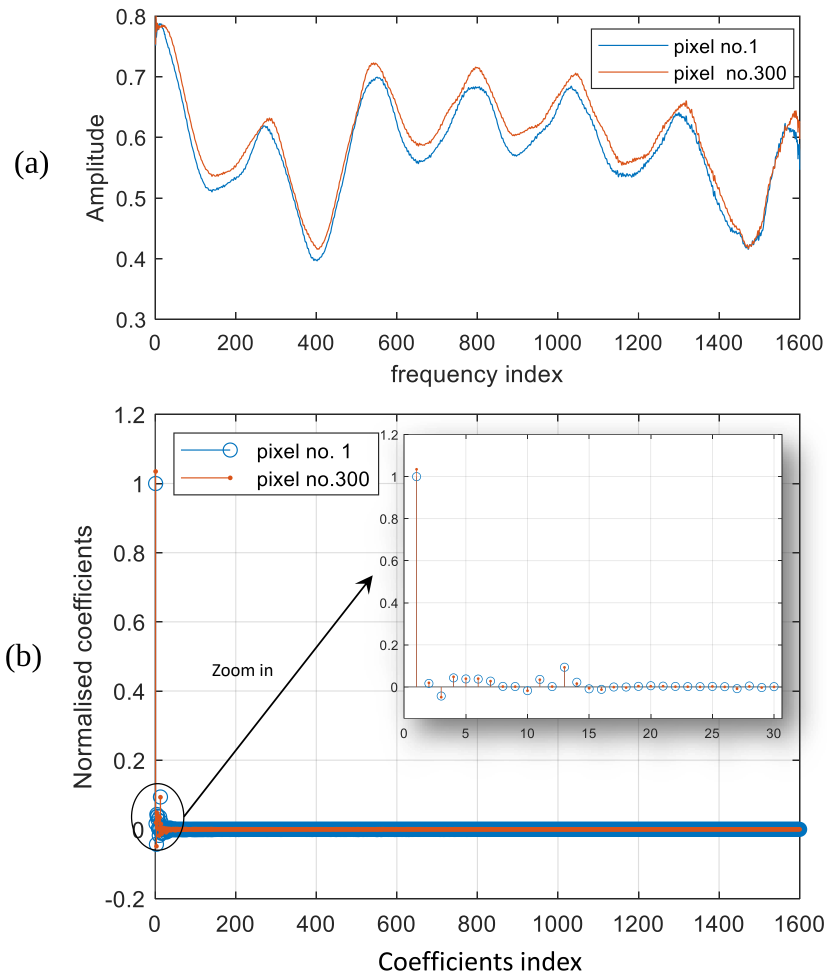

Figure 4.9 The (a) spectral data of two pixels and (b) the corresponding DCT coefficients. The dominant coefficients of pixel no. 1 and no. 300 have same position but different value.

Table 4.1 The probability of sharing the same sparse coefficients index for the largest N_m coefficients.

The largest N_m coefficients	The probability of sharing the same sparse coefficient index out of N_m largest coefficients
20	0.9936
30	0.9775
50	0.8995
100	0.8589

(a)

(b)

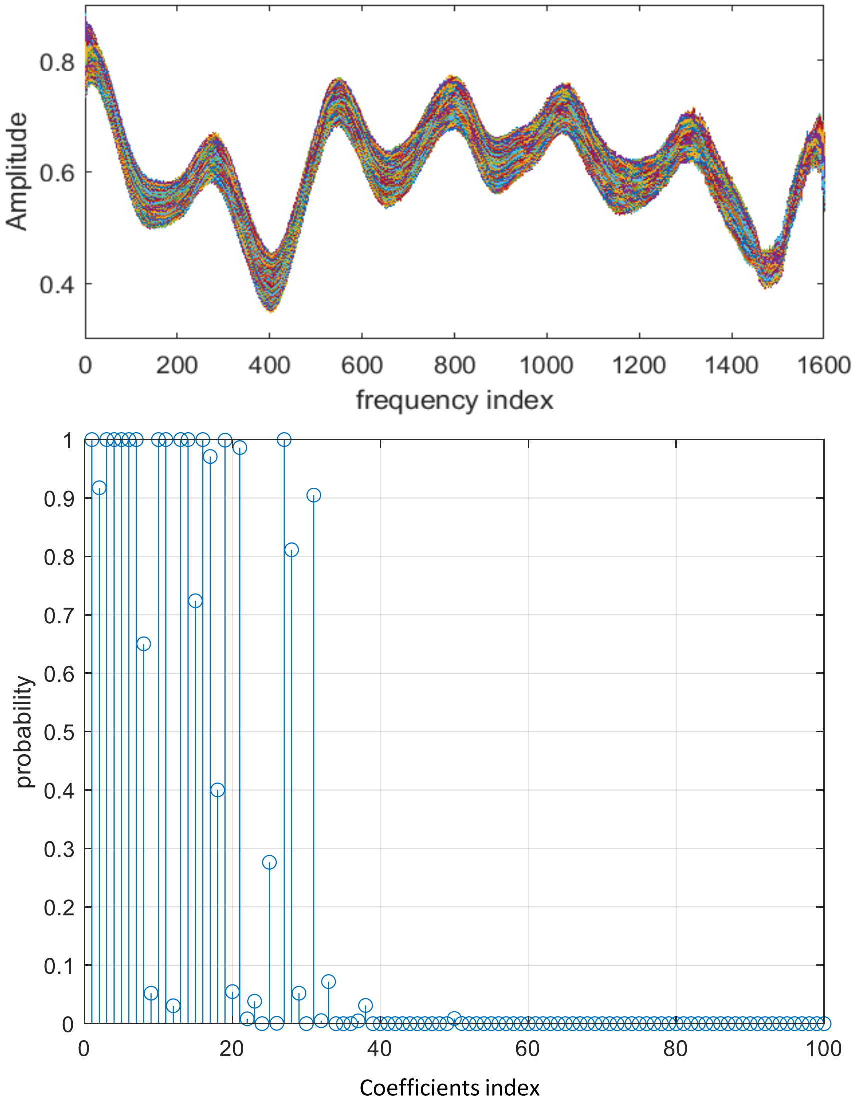

Figure 4.10 The (b) probability of coefficients index is in the most significant 30 coefficients for (a) the dataset.

The joint sparsity in the spatial domain is evaluated after the joint sparsity in the frequency domain. Figure 3.15 in Chapter 3 already shows the spatial frame is sparse on DCT basis. Based on the analysis, the joint spatial sparsity is discussed. As shown in Figure 4.5, the proposed

ASSS algorithm reconstructs the spatial data block-by-block with *d* neighbour frames. To prove this design, the DCT coefficients for image no. 50 and no. 160 in 6J specimen is shown in Figure 4.11 firstly. The two images are significantly different from each other, and their DCT coefficients are also different as shown in Figure 4.11(b). For these two images, no joint sparsity property is observed. The *d* is 160−50=110 in this case, which demos that too large *d* cannot meet the joint sparsity condition. Another case where *d*=20 is shown in Figure 4.12. The two images are visually like each other, and their DCT coefficients in Figure 4.12(b) shows joint sparsity property. Their dominant coefficients share the same index with a different value.

(a)

(b)

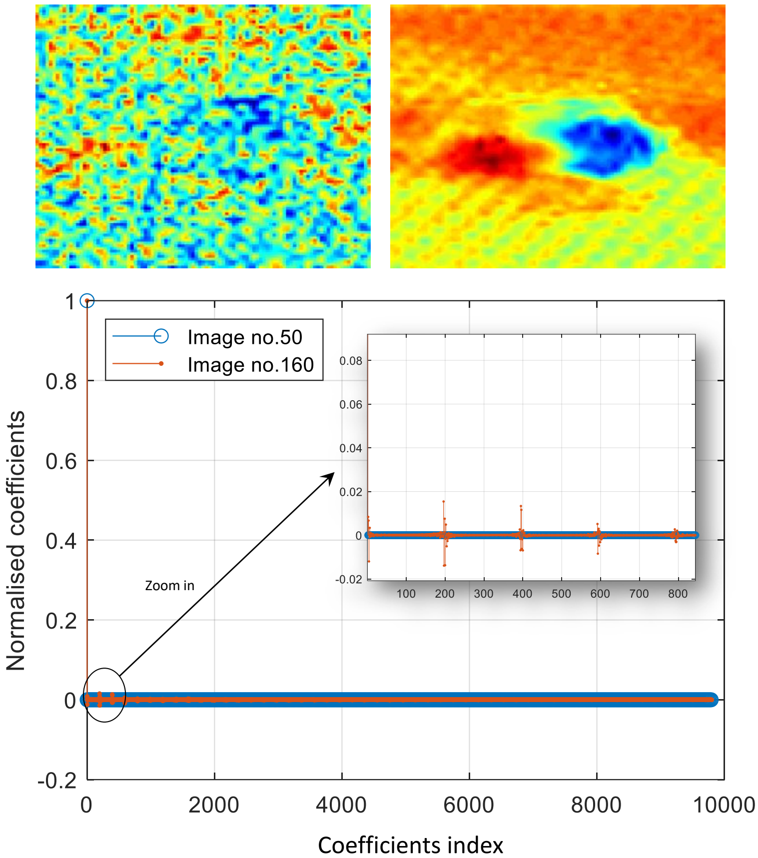

Figure 4.11 The DCT coefficients (b) of two different spatial images (a) with d=110. They have totally different sparse coefficients.

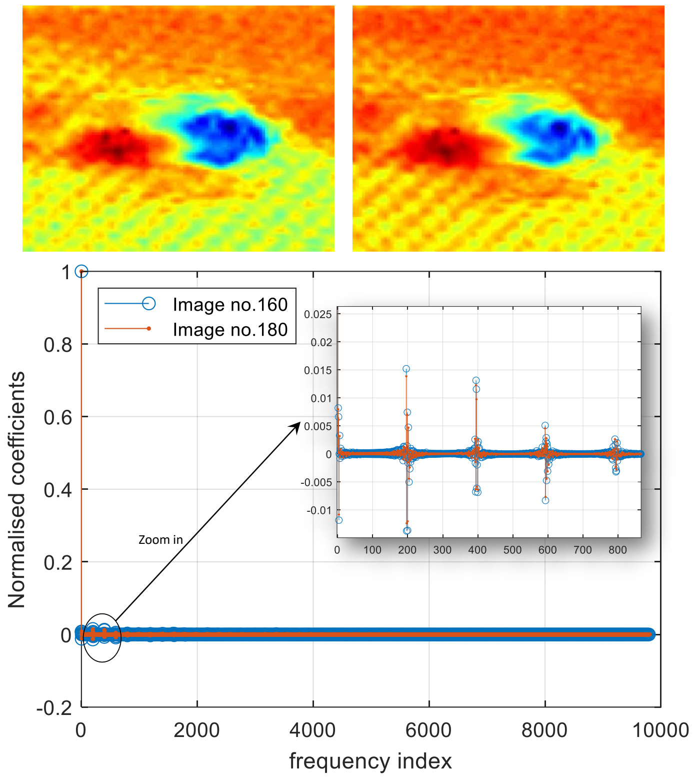

Figure 4.12 The (b) DCT coefficients of (a) two different spatial images with d=20. They have same sparse coefficients location but different values.

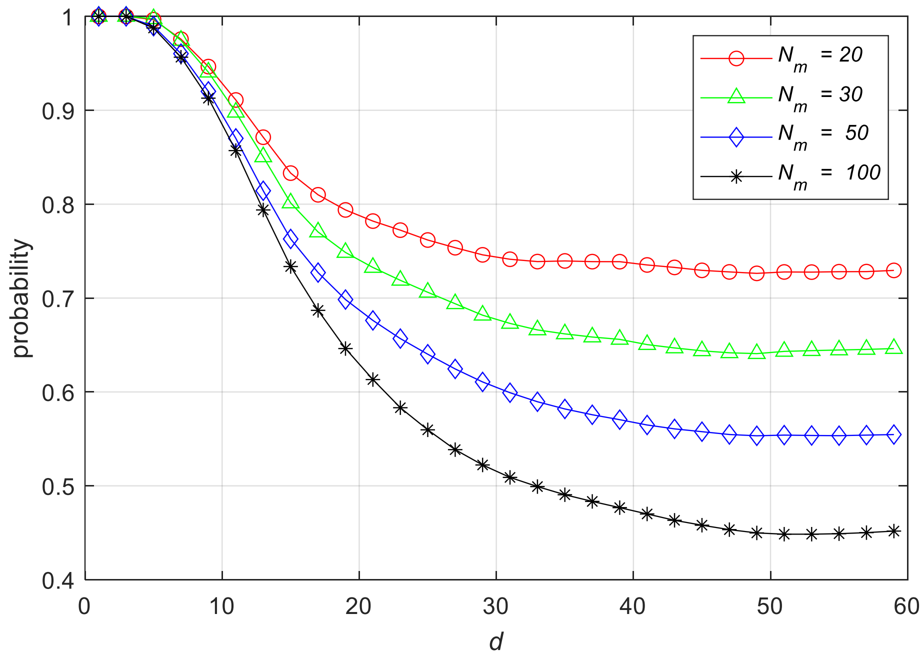

Figure 4.13 The probability of sharing the same DCT coefficients index vs d under different N_m

The above evaluation proves that the value of d will influence the joint sparse condition. d quantifies the number of neighbour frames. When d is too large, there is no joint sparsity. On the contrary, too small *d* will decrease the time gain of the proposed methods. To help with setting the *d* values, the probability of sharing the same DCT coefficients index again *d* is given in Figure 4.13. This probability is obtained by counting the number of same coefficients index out of the N_m largest coefficients for an arbitrary pair of images, and randomly chooses the reference image (d = 0) with uniform distribution. The figure shows that the neighbour frames with d<10 has high joint sparsity with probability more than 0.9. The probability decreases rapidly hereafter before stable. Because the corresponding two images become more visually different with *d* increasing, but they share a small part of dominant values that lead to stable. The figure shows that a stricter threshold has higher joint sparsity as the probability is higher vertically for less N_m.

4.5.2 The feature constraint for impact damage detection on CFRPs

The accuracy of feature constraint will directly influence the right spatial-spectral data to sample. This section performs the proposed feature constraint extraction scheme on the same specimen and same spatial area as raster scan. Figure 4.14 calculates the feature extraction indicator for the different specimen, the indicator is the standard deviation in this impact damage detection case on CFRPs. They are smooth curves which are sparse on DCT basis. To validate this, the sorted DCT coefficients are given in Figure 4.15. A sharp decrease is observed at the beginning, which proves sparse on DCT basis.

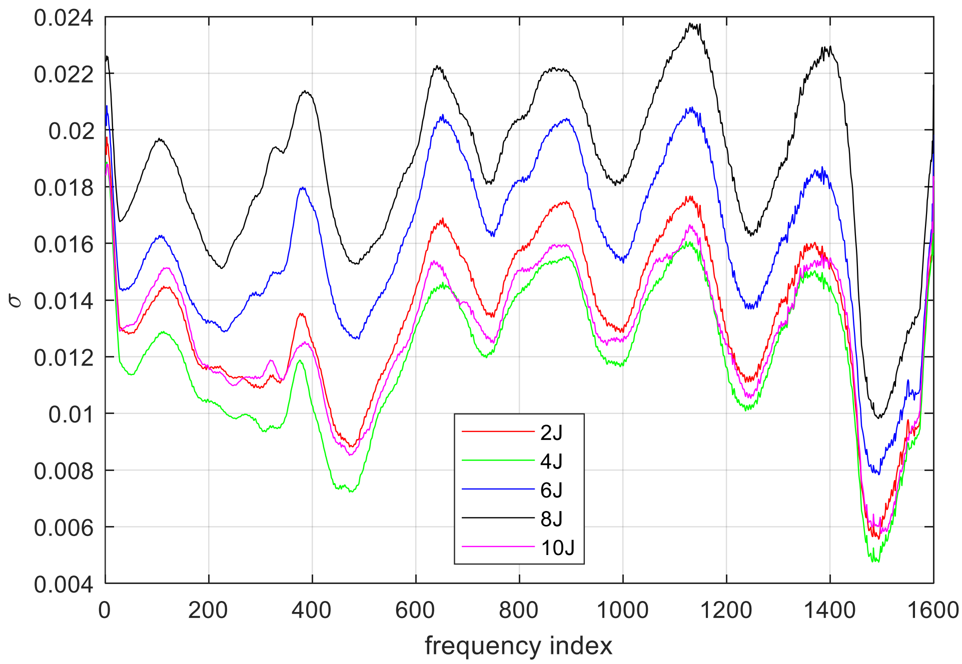

Figure 4.14 The standard deviation of dataset for different specimen from 2J to 10J.

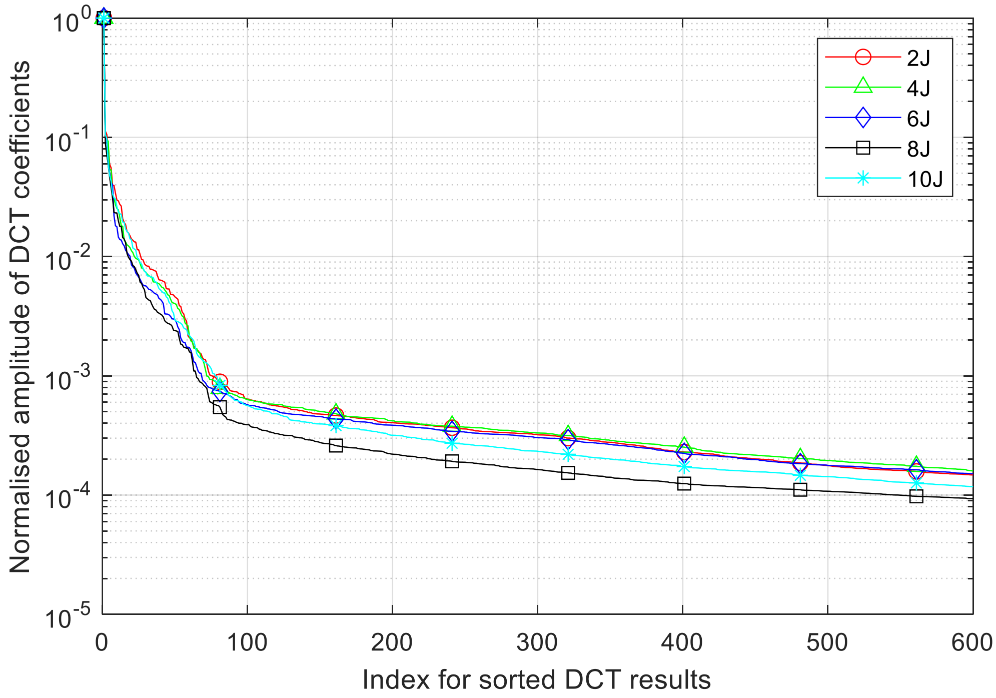

Figure 4.15 The sorted DCT coefficients for σ in Figure 4.14.

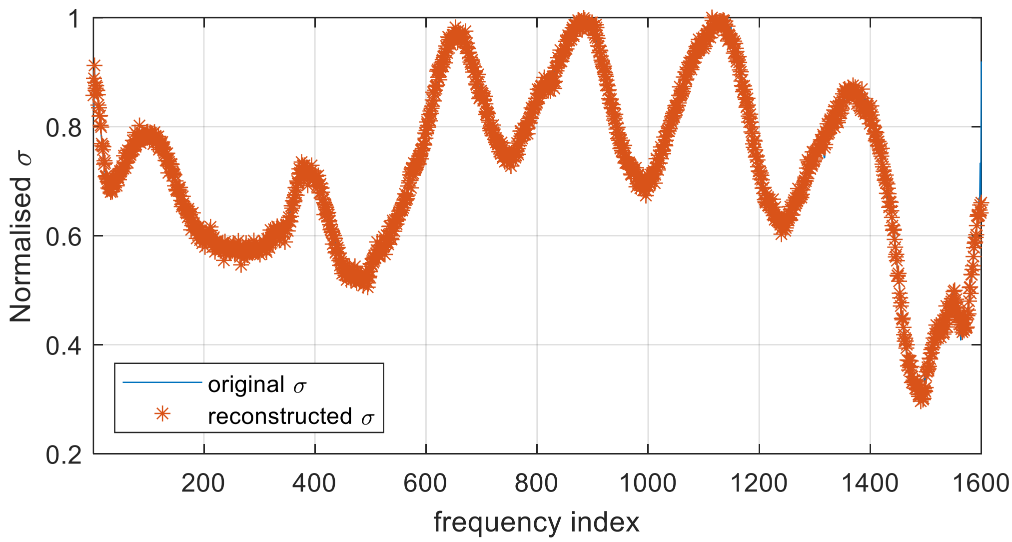

Figure 4.16 A demo for reconstructing the feature extraction indicator for a 6J specimen with DCT as the sparse basis and m_f=320.

Based on the sparse analysis, Figure 4.16 gives one demo for reconstructing the feature extraction indicator. The measurement matrix $\mathbf{\Phi}_f$ is generated using the algorithm in Figure 3.4. $\mathbf{\Phi}_{s1} = \mathbf{1}$ in this case. m_f is set to 320, which is 20% of the whole frequency band. For implementation, $\mathbf{\Phi}_f$ is imposed to the frequency sweep data to select the frequency frame for calculating the corresponding σ_i, which is more practical because the random sampling in frequency domain do not save sampling time significantly and brings more complicated implementation process. The reconstructed standard deviation using OMP perfectly fits with the original standard deviation, which validates the ability to find target frequency qualitatively.

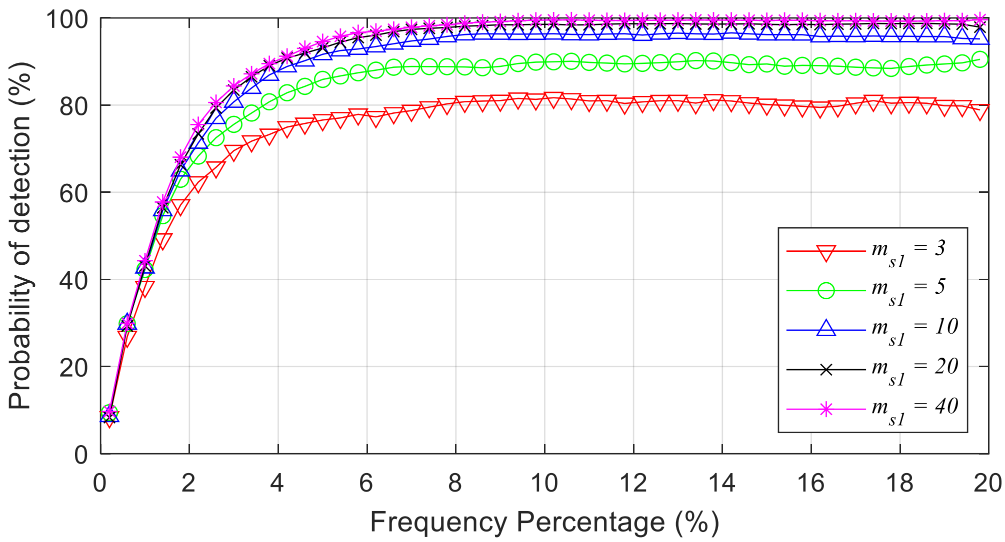

Figure 4.17 Probability of detection vs spectral sampling percentage.

For quantitative validation, the probability of detection p_f is used. It is defined as the probability that the position difference of detected target frequencies and the true target frequencies is below a pre-defined threshold, which can be calculated by thresholding the Hamming distance between original $\mathbf{i}$ and detected $\hat{\mathbf{i}}$ with Monte Carlo methods as

$$p_f = E\left[1-\sum_{i=1}^{n_f}\operatorname{xor}\left(\mathbf{i}_i,\hat{\mathbf{i}}_i\right)\Big/n_f\right] \tag{4.12}$$

where $E[\cdot]$ is the mathematic expectation, $\operatorname{xor}(\cdot)$ is exclusive-*or* operation. What is different from the qualitative validation settings is that $\mathbf{\Phi}_{s1}$ is set using the algorithm in Figure 3.4 for different spatial sampling percentage. Only small number of spatial locations are sampled with frequency sweep. Then $\mathbf{\Phi}_f$ is imposed on the frequency sweep data. Such settings only calculate a small part of $\boldsymbol{\sigma}$ with $f(\sigma_i)$, the rest of $\boldsymbol{\sigma}$ is reconstructed with this part of values instead of from $f(\sigma_i)$. As mentioned in section 4.3.2, $f(\sigma_i)$ is laborious when the data volume is high or $f(\cdot)$ is a very complex process. The average probability of detection under such case for a various number of spatial pixels m_{s1} is shown in Figure 4.17. γ_1 is set as

$0.95\max(\boldsymbol{\sigma})$ which mean only the most significant 5% of indicator values are chosen. It is evident that the increase in pixel number does not contribute to the detection probability significantly. Even just 3 sampling pixels (0.03% of the total pixel) get the right target frequency with more than 80% probability when using just 20% of frequency sampling percentage. 40 pixels (0.41% of the total pixel) can find the right target frequency. The probability of detection is increasing slowly when the spectral sampling percentage is large enough, which is influenced by the sparsity on DCT basis.

4.5.3 Aligned spatial-spectral sensing

The reconstruction quality of ASSS is the source data where defect pattern is extracted. OMP is used to jointly reconstruct the sampled spectral and spatial data. Spatial-spectral sweep results are used as a baseline. To fully explore the performance of ASSS, all the frequency band is set as interested frequency, i.e. there is no feature extraction constraint applied. In such a case, all spatial-spectral data can be reconstructed for further analysis. Note that the proposed ASSS scheme is additive with the feature constraint. The feature constraint only refines the frequency band where ASSS is applied. Figure 4.18 presents some results for different spatial and spectral sampling percentage with DCT as the sparse basis. With the increase in spatial and frequency sampling percentage, the reconstructed results become more like the baseline. 30% in spatial and spectral domain already has little visual difference to the baseline in this case study.

Two metrics are used to compare the baseline results and the ASSS results frame-by-frame, i.e., the 2D correlation and normalised root mean square error (NRMSE). 2D correlation evaluates the similarity between the overall shapes of different datasets, while NRMSE evaluates the similarity using the absolute difference. Using both leads to a more accurate evaluation. The average 2D correlation for all frames in different specimen samples are shown in Figure 4.19. Either increasing the spatial sampling percentage or spectral sampling percentage improves the reconstruction quality. In this ORWG imaging system, only 30% of spatial and frequency sampling percentage for ASSS obtains 98.2% similarity as the baseline. Even 3% in both domains gets 69.4% similarity. The intersecting line between 90% similarity plane and 2D correlation surface demonstrates the combination case where the similarity is greater than 90%. For example, 10% spectral and 20% spatial (2% of whole data) sampling percentage.

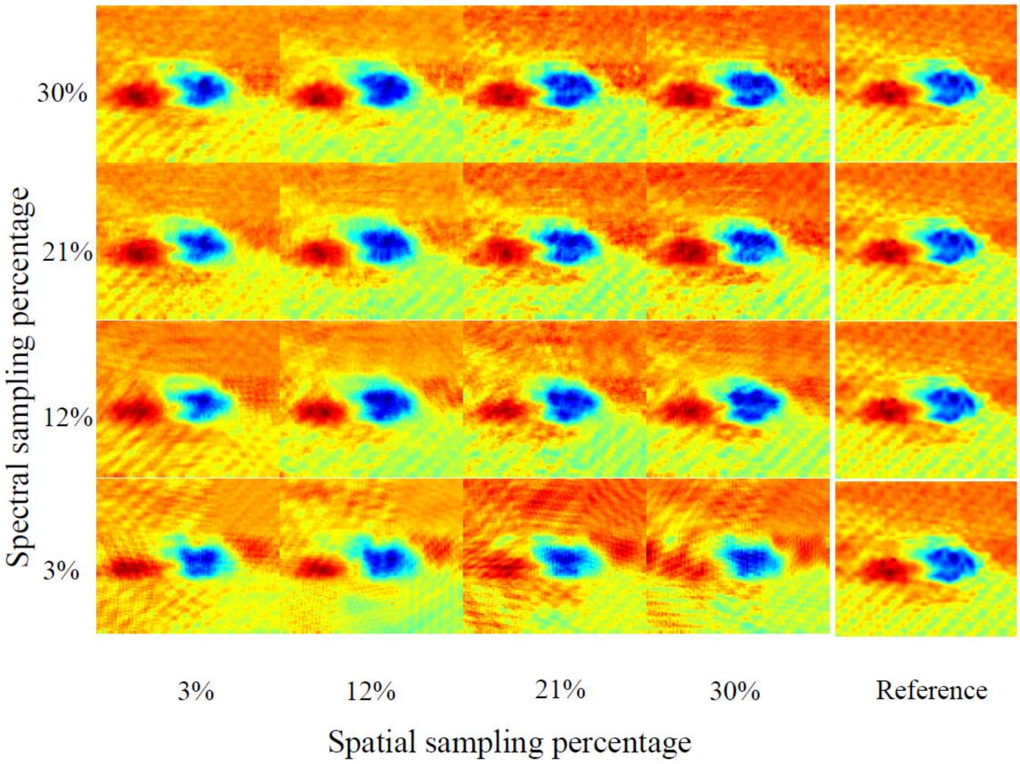

Figure 4.18 A comparison between the reconstructed image using the proposed algorithms and the spatial-spectral sweep.

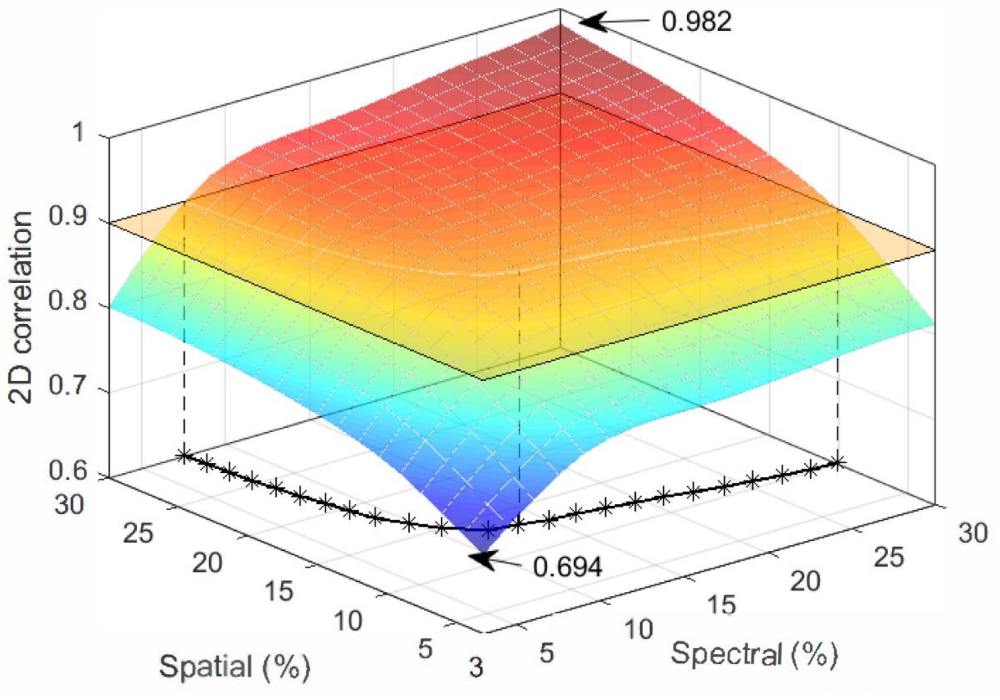

Figure 4.19 Average 2D correlation under different spatial and spectral sampling percentage.

The average NRMSE is shown in Figure 4.20, which demonstrates a sharp decrease when the spectral sampling percentage increase. Increase in spatial sampling percentage does not have such a significant influence as increasing spectral percentage. The 2D correlation results and the NRMSE prove that only sampling as low as 2% of what spatial-spectral does get more than 90% similarity, which saves 98% sampling data/storage space.

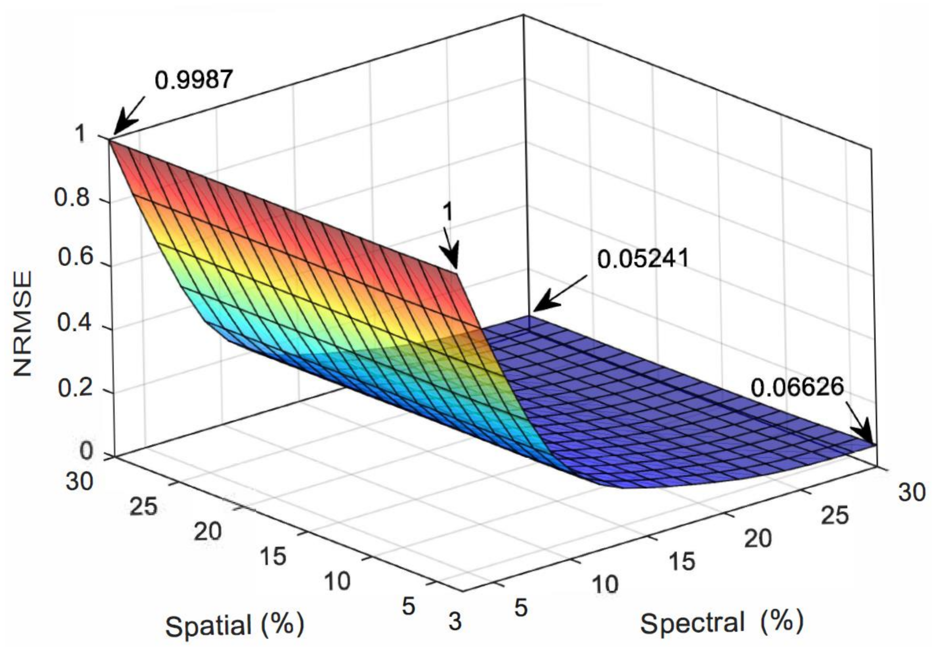

Figure 4.20 Average NRMSE under different spatial and spectral sampling percentage.

4.5.4 The influence on feature quality for the proposed ASSS with feature constraint

The proposed scheme preserves feature with reduced data amount. This section presents the influence on feature quality with the proposed feature-supervised CS data acquisition. The defect region segmented on the spatial-spectral sweep is used as a baseline to evaluate the extracted feature with FsCS. The defect region is the interested feature in this study. The defect region is extracted from the frequency frames which correspond to large standard deviations, and the proposed scheme senses it by setting the threshold in the feature extraction constraint as $\gamma_1 = 0.7\max(\boldsymbol{\sigma})$. Thus the frequency band to apply ASSS only occupies ρ = 30% of the total frequency band in this case study. The sampling burden and the data for feature extraction is greatly decreased. To extract the binary defect region, we employ the HTED algorithm from chapter 3 because of its superior de-nosing ability. The HTED algorithm is applied in both raster scan images and the reconstructed images with the proposed method. The raster scan results is used as baseline. Figure 4.21 presents some extracted defect pattern for various spatial-spectral sampling percentages. More sampling percentage leads to more similar defect pattern as the baseline. Even 3% of spatial sampling obtains similar defect pattern as baseline together with 30% of spectral sampling, because the reconstructed image under this sampling configuration achieves more than 90% of correlation with the baseline.

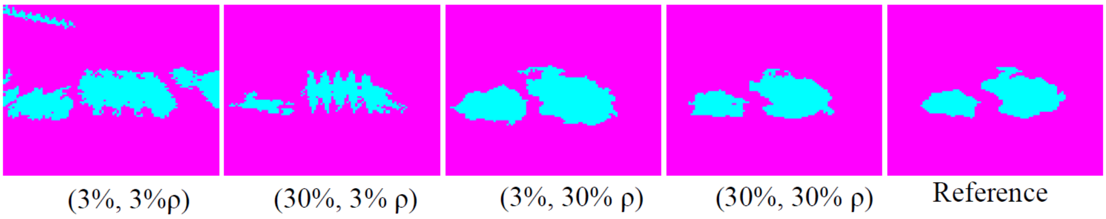

Figure 4.21 The extracted defect pattern with various spatial-spectral sampling percentage.

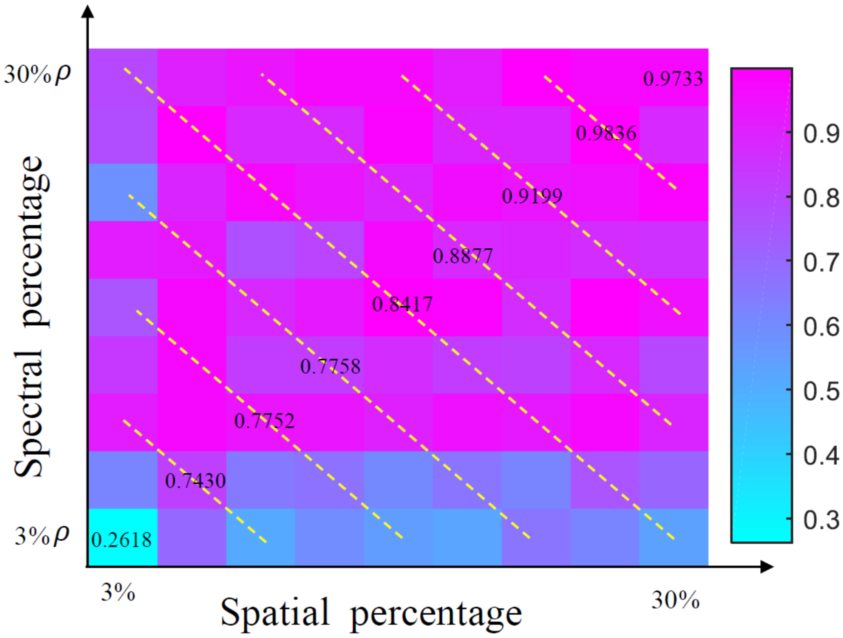

Figure 4.22 Similarity ratio of defect pattern size between the proposed scheme and spatial-spectral sweep results.

Quantitative evaluation is carried out by the average similarity ratio of defect size between the proposed method and the baseline by spatial-spectral sweep. Different spatial-spectral sampling percentage, specimens and frequency frames in each specimen are counted in the average. The similarity ratio (p_τ) is defined as

$$p_\tau = \left|S_{rec} - S_{ref}\right| / S_{ref} \tag{4.13}$$

where S_{rec} and S_{ref} denote reconstructed defect and the baseline. The results are shown in Figure 4.22. The similarity ratio is very low under 3% of spatial and spectral sampling rate because the sampling amount is not in the order of $m = \mathrm{O}(\alpha \log n)$, which cannot guarantee successful reconstruction. The similarity ratio increases with the increase of spatial and spectral sampling percentage. To highlight this influence, the average similarity of diagonal similarity ratio (The elements covered by the yellow dash line) is calculated and labelled in the figure. It clearly illustrates that more spatial-spectral sampling percentage leads to higher similarity ratio. Figure 4.22 also shows that defect patterns extracted from around only 20%ρ×20%=1.2% of spatial-spectral sweep data already have more than 90% of similarity ratio as the reference image, which demonstrates FsCS preserves feature integrity even under the millesimal level of sampling percentage.

4.5.5 The gain of the proposed method in reducing data amount and improving time-efficiency

This chapter develops ASSS methods with feature constraint that aims to reduce data amount for feature extraction. Only the sector of data that will finally be used for feature extraction is sampled. The gain in reducing data amount is decided by the γ_1 in equation *(4.5)*. For example, $\gamma_1 = 0.95\max(\boldsymbol{\sigma})$ leads to 5% of full data, which have a gain of reducing 95% of data for feature extraction.

On the time-efficiency side, this chapter jointly reconstructs neighbour frames based on their joint sparsity, which speeds up the reconstruction greatly. To prove this, joint reconstruction and sequential reconstruction with OMP for same datasets are performed. Ten neighbour frames are chosen from the 6J specimen are the dataset $\mathbf{X}$. When using OMP for joint reconstruction, the sparse support Λ is identified using only one spatial frame, then the support is used to construct the whole dataset with $\mathbf{X} = \left(\mathbf{A}_\Lambda^{\mathbf{T}}\mathbf{A}_\Lambda\right)^{-1}\mathbf{A}_\Lambda^{\mathbf{T}}\mathbf{Y}$ according to the OMP algorithm in Figure 2.6. The running time for the two methods in Matlab R2018a with Core I7-7500u CPU and 8GB memory is shown in Figure 4.23 below. The time is recorded with 'tic' and 'toc' command in Matlab. The running time increases rapidly with the number of spatial percentages, but the joint reconstruction increases much slower. The time gain that defines as the ratio for the two times is shown in Figure 4.24, which shows a linear trend with the increasing of spatial sampling percentage. These two figures illustrate the time-efficiency of using joint reconstruction.

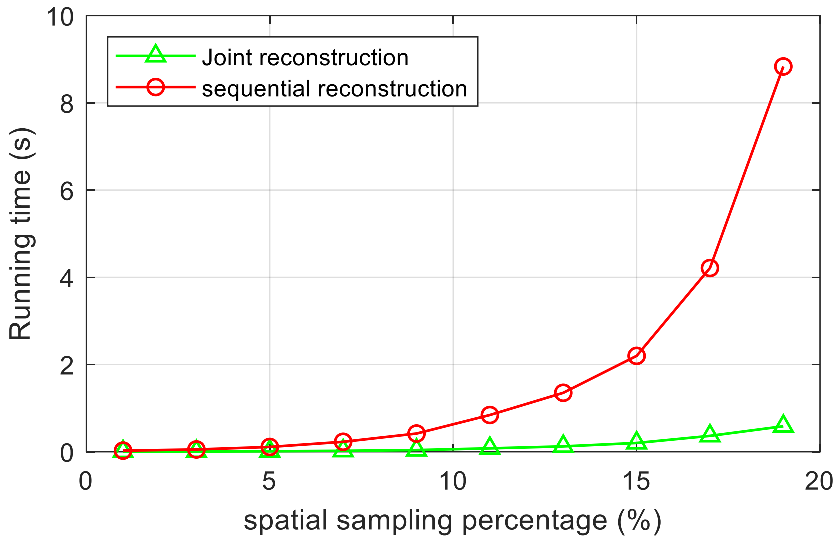

Figure 4.23 Running time compare between joint reconstruction and sequential reconstruction with OMP for ten spatial frames.

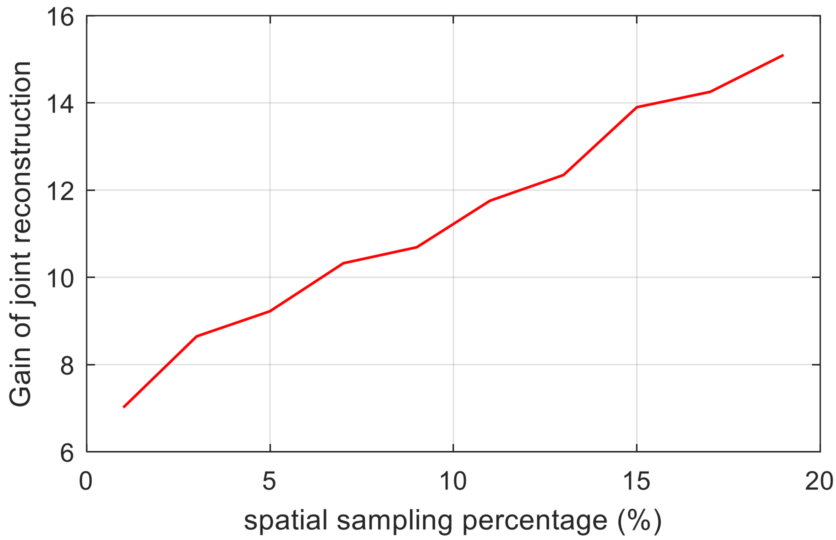

Figure 4.24 Time gain of joint reconstruction when compared to sequential reconstruction with OMP.

4.6 Chapter Summary

Based on the proposed online CS-based model in the last chapter, this chapter proposes feature-supervised compressed sensing (FsCS) which involves feature extraction process to supervise sensing process in open-ended waveguide NDT systems. FsCS researves the interested feature while reducing the data amount, and FsCS improves reconstruction speed by using joint sparsity in and reconstructing with joint reconstruction. The frequencies which reveal the feature only occupy a small part of the frequency band, this method finds this sparse frequency range with feature constraint to supervise the sampling process. Subsequently, based on joint sparsity of neighbour frame, an aligned spatial-spectrum sampling scheme is proposed to only sample interested frequency range for required features by using a customised 0/1 Bernoulli measurement matrix. The interested spectral-spatial data are reconstructed jointly which has much faster speed than frame-by-frame methods. The case study in impact damage detection on CFRP materials with open-ended rectangular waveguide shows that the data amount is reduced greatly without compromising feature quality. The gain in time-efficiency increases almost linearly with the number of sampling points comparing to sequential reconstruction.

As for limitations, one core condition for this method is the interested feature only embedded in a small part of the whole data. In fact, this is the case for many applications. Traditional applications collect data first before extracting the useful information, the collected data is usually highly redundant for a specific feature. However, this method needs the sparsity information as prior information of the feature data screening indicator in the feature constraint step, which means the user needs to get the indicator using traditional way first if they know nothing about the signal character. A second condition is that the multi-dimension data should have joint sparsity property for the aligned spatial-spectral sampling. This is also based on analysis of the training data to get the joint sparsity information.

Chapter 5. Damage Detection using CS Data

The previous two chapters mainly contribute to the data acquisition side. Feature extraction is another crucial issue in open-ended waveguide NDT systems. The previous chapters propose HTED algorithm for impact damage detection on CFRP, and it shows well performance than other image segmentation algorithms. However, it is performed on the reconstructed full data after the relatively time-consuming sparse reconstruction. Although reconstructing the full data is good for visualisation and other processing, more critical issue is that how the feature itself which directly related to decision-making can benefit from CS measurement scheme. Compared to the feature extraction in the previous two chapters, this chapter proposes qualitative and quantitative defect detection algorithms from CS data directly rather than from the reconstructed data. The work in this chapter is presented in the 23rd International Workshop on Electromagnetic Nondestructive Evaluation, Michigan, USA, 2018 and forms one paper for it.

5.1 Qualitative Detection using CS Data

5.1.1 Problem statement & related works

Qualitative detection gives a one-bit decision on the SUT, either health or illness. The proposed HTED algorithm in chapter 3 takes the fully reconstructed spatial image as input and achieves more accurate defect pattern extraction than other image segmentation methods. However, it is too laborious for qualitative defect detection with HTED. As mentioned in previous chapters, the histogram for the amplitude of reflection coefficients that contains the damaged area shows long tails in impact damage detection on CFRP materials. This feature can be used for making a binary decision. One property for this histogram feature is that it is invariant to downsampling, which means the binary qualitative detection does not require full data. There are traditional downsampling methods [175] like random line scanning [117], uniform downsampling and 2D random line scan. The data obtained in this thesis is also downsampling data using the customised 0/1 Bernoulli matrix, this section investigates the possibility of directly defect defection on the CS data without reconstruction.

5.1.2 The proposed CS-based qualitative defect detection

The overall methodology to solve the highlighted problem in the last subsection is given in Figure 5.1. The proposed CS-based qualitative defect detection is shown in green, other cross validation methods are also given. Firstly, the specimens are sampled with the following methods. Different data will obtain after the sampling, these data are then sent to a proposed histogram thresholding process for the qualitative decision. Finally, compare their decision results. More detail about the proposed scheme is given hereunder.

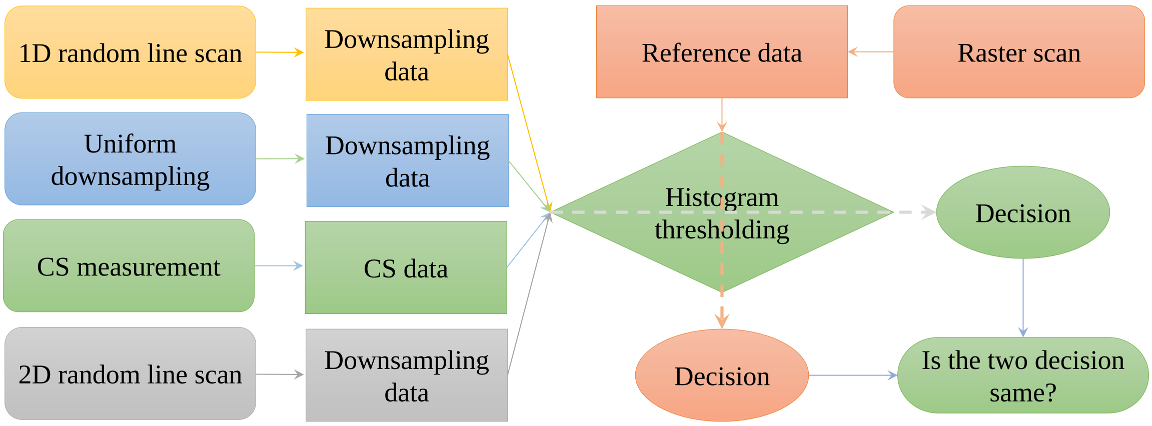

Figure 5.1 Methodology diagram for the proposed CS-based qualitative defect detection. The proposed method is shown in green, other methods like line scan are also given for cross validation.

Recall the CS measurement model for signal **x**,

$$\mathbf{y} = \mathbf{\Phi x} + \boldsymbol{\xi} \tag{5.1}$$

An element of the measured data can be denoted as:

$$y_i = \sum_{j=1}^{n} \Phi_{i,j} x_j + \xi_i \tag{5.2}$$

From the probability theory point of view, i.e., regarding the signal elements *x* and *y* as random variables. According to Equation (5.2), the distribution of *y* is usually different from *x*. However, they can have the same distribution under some special design of $\mathbf{\Phi}$. For example, if each row of $\mathbf{\Phi}$ only have one constant value '*a*' and have '0' for the rest of it, Equation (5.2) becomes:

$$y_i = a x_j + \xi_i \tag{5.3}$$

In such cause, x and y will have the same distribution if the variance of the Gaussian noise term $\mathrm{var}(\xi) \ll E[ax]$. Fortunately, the measurement matrices in Chapter 3 and Chapter 4 meet the condition. So, qualitative defect detection directly on CS data is possible. The diagram is shown in Figure 5.2. The input parameters are under the same constraint as the HTED algorithm in Chapter 3.

The proposed method performs qualitative defect detection in CS measurement, i.e. random downsampling of the whole spatial area using the customised 0/1 Bernoulli measurement matrix in Chapter 3 and Chapter 4. Other downsampling methods such as thresholding of random line scanning, uniform downsampling and 2D random line scan are used to compare with the proposed method. Figure 5.3 shown the demo sampling pattern for all these methods, where the red area is sampling locations.

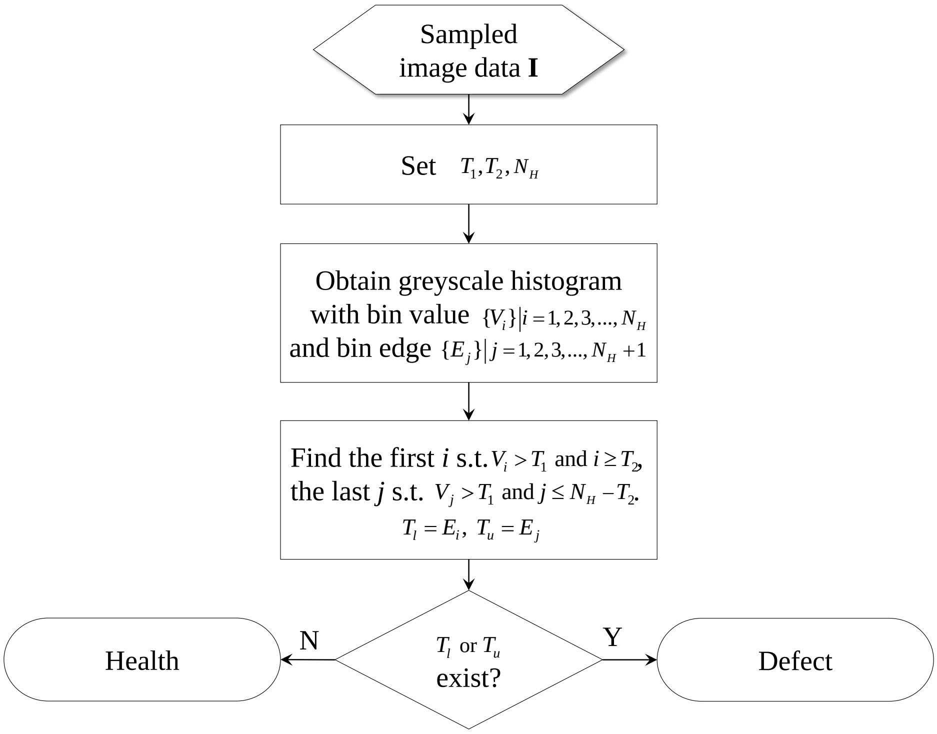

Figure 5.2 Diagram for qualitative defect detection

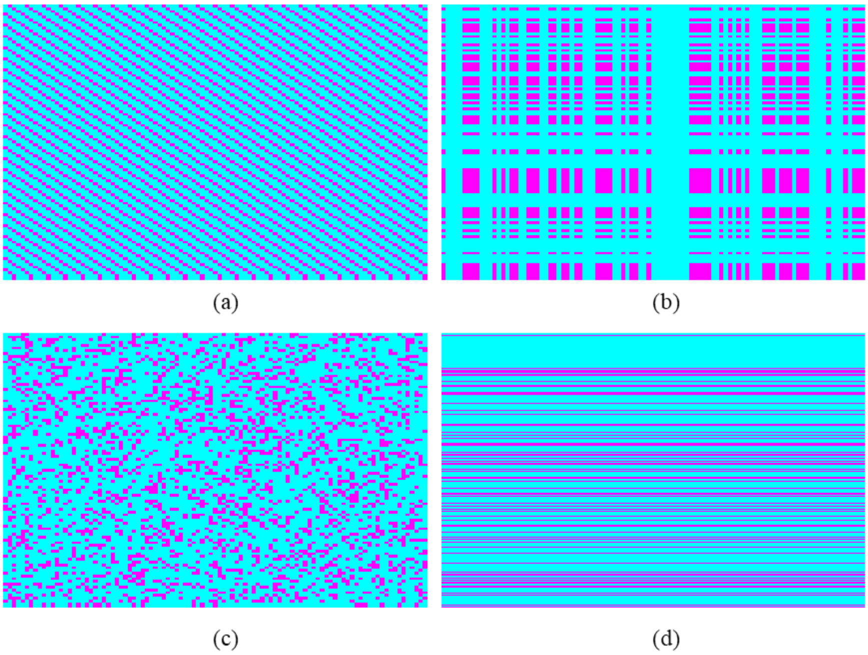

Figure 5.3 Sampling pattern for (a) uniform downsampling, (b) 2D random line scan, (c) CS-based, (d) 1D random line scan for 25% of sampling percentage.

5.1.3 Experimental setup for the proposed CS-based methods

To evaluate the CS based qualitative defect detection method, this section uses the same specimen as that in Figure 3.13 and the experimental setup in Figure 3.11. CS-based methods, 1D and 2D random line scanning, uniform downsampling are implemented for performance evaluation as shown in Figure 5.1.

To simplify the process, VNA only sample at one narrow frequency band which reveals the damage areas, i.e. around 19GHz according to the results in Chapter 3. The number of frequency point is 801. Then a 100*mm*×100*mm* spatial area on the five specimens which involves the impact point in the centre is sampled with raster scan. One 30*mm*×30*mm* rectangular window is applied to the raster scan data to form a study area. The window shift in X and Y direction with 1*mm* of step size. The spatial data in each window is chosen as a reference image for qualitative defect detection. Then the equivalent sampling data of CS-based methods, 1D and 2D random line scanning, uniform downsampling are obtained by taking the logical '*And*' using the sampling pattern in Figure 5.3 and the reference image. These study areas include cases with/without the impact defect.

5.1.4 Evaluation results for the proposed CS-based methods

The cross validation methods are compared in term of precision (η_{pre}), recall (η_{rec}), probability of detection (η_{PoD}) and accuracy (η_{Acc}) which is defined as follows:

$$\eta_{pre} = N_{TrA} / N_{ToA} \quad (5.4)$$

$$\eta_{rec} = N_{TrA} / N_{ReA} \quad (5.5)$$

$$\eta_{PoD} = N_{ToA} / N_{ReA} \quad (5.6)$$

$$\eta_{Acc} = N_{Tr} / N_{T} \quad (5.7)$$

where N_{TrA}, N_{ToA}, N_{ReA}, N_{Tr}, N_{T} represent true-alarm number, total alarm number, total alarm number from reference data, truly detected number and total test number, respectively. The precision indicates how accurate the alarms are. The recall indicates how completed the true alarm results are. The probability of detection indicates how complete the alarm results are. And the accuracy indicates how accurate a decision is. These indicators together will give a more comprehensive performance evaluation. Higher values of all indicators corresponding to better performance.

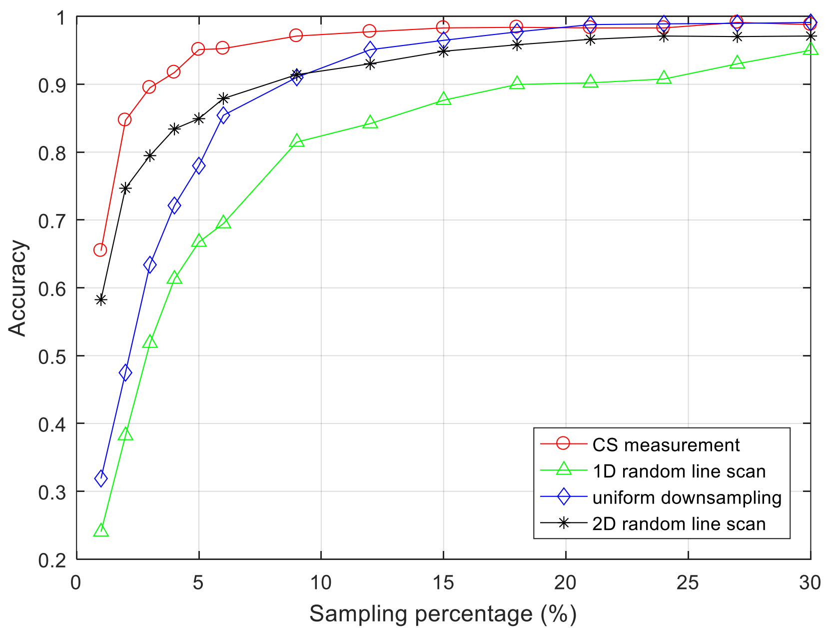

Figure 5.4 Accuracy of qualitative detection from downsampling algorithms

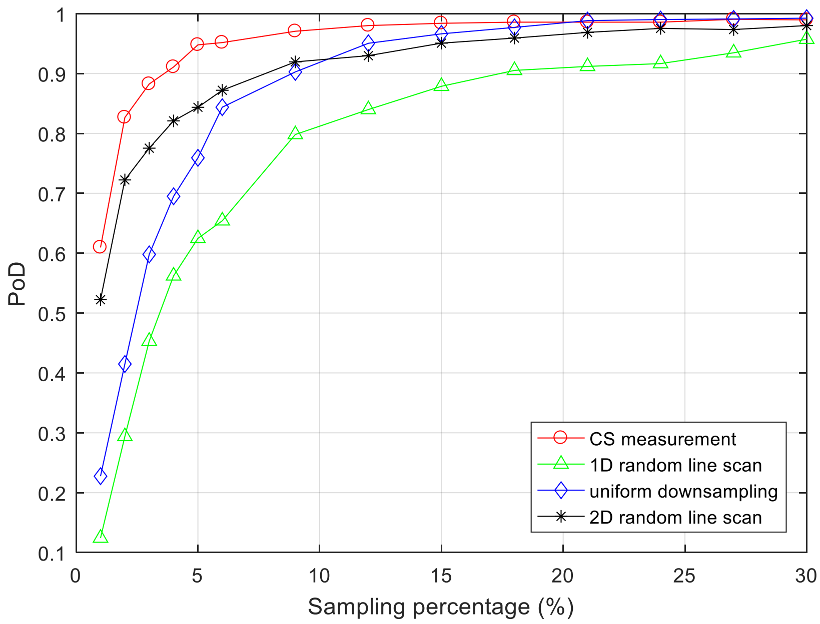

Figure 5.5 Probability of detection of qualitative detection from downsampling algorithms

The average performance results are shown in Figure 5.4 to Figure 5.7. All these figures demonstrate the better performance of the proposed qualitative defect detection from CS measurement. Line scanning has the worst performance in all indicators, because it suffers from picket-fence effect most, the sampling data have large errors to represent the original data. On the contrary, random sampling patterns in CS measurement reserves local information most, which lead to the best performance.

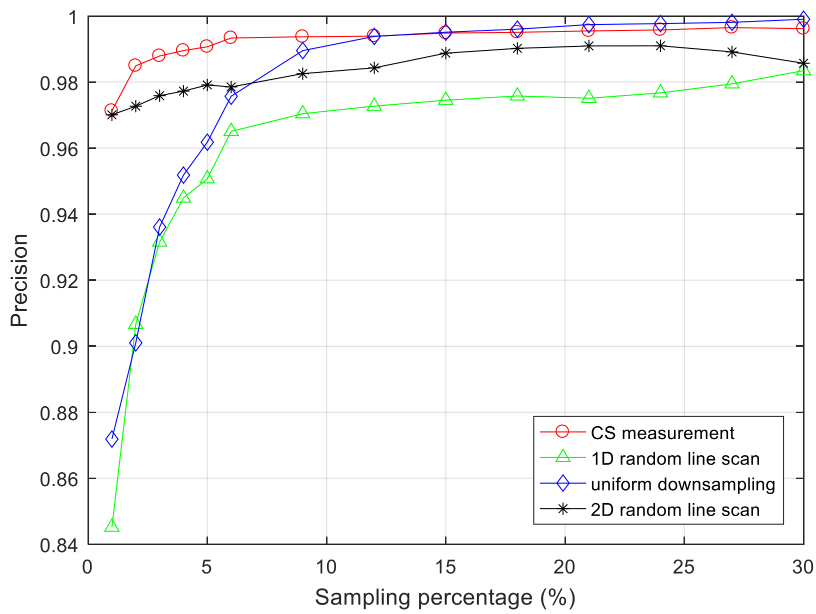

Figure 5.6 Precision of qualitative detection from downsampling algorithms

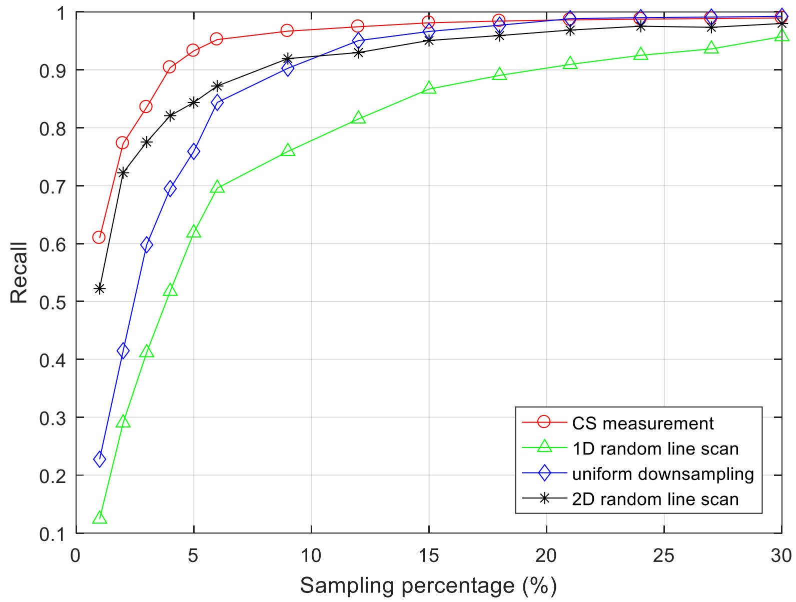

Figure 5.7 Recall of qualitative detection from downsampling algorithms

5.2 Quantitative Detection using a New CS Reconstruction Algorithm

5.2.1 Problem statement & related works

The previous section discussed qualitative defect detection from CS data. For quantitative defection, a HTED algorithm which extracts binary defect pattern from the reconstructed image is presented in Chapter 3. The defect pattern can be extracted only after the CS reconstruction process. The reconstruction process is usually time-consuming and computationally-intensive. These drawbacks prevent its application in time-sensitive and power-limited applications, which calls for more swift feature extraction techniques. Furthermore, from the decision-making point of view, the quantitative defect pattern feature is what needed for decision-making rather than the original spatial image. So the procedure that reconstructing the whole spatial image and extract damage area from it using HTED in the last two chapters is not time-efficient.

For the problem of swift defect detection, one technical route is finding faster reconstruction algorithms which will reduce the feature extraction delay. As introduced in section 2.4, the greedy algorithms have relatively high accuracy and low complexity. As a well-known greedy algorithm, OMP finds another support that has the largest absolute correlation with the residual in each iteration. By subtracting the components of selected support from the measurement results, OMP pursuits the entire support with iteration. The easy implementation of OMP makes it widely used to solve sparse reconstruction problems [176, 177]. However, it is vulnerable to error propagation effect [178, 179]. Because there is no rigid mathematical proof of recovery guarantees for greedy algorithms, the selected support may not be the right support that should be selected in fact.

To address the error propagation effect and improves reconstruction speed, more greedy algorithms have been proposed such as Stage-wise Orthogonal Matching Pursuit (StOMP) [179], iterative hard thresholding (IHT) [78], generalized OMP (gOMP) [180], and Compressive Sampling Matching Pursuit (CoSaMP) [181]. These algorithms select multiple supports in each iteration to improve efficiency. For example, during each iteration, gOMP chooses the supports that in the most significant L absolute correlation with residual. StOMP selects all the supports that the correlation is above the pre-defined threshold. Besides identify multiple supports, some algorithms can screen out the selected historical supports which fail to give larger correlation than the new candidate support. For example, CoSaMP performs a two-stage sparse signal estimation approach which can add or remove new support candidates adaptively. Another category which deals with the error propagation effect is the Bayesian matching pursuit [182-184], these methods regard the sparse signal as random variables. The sparse signal can be estimated by maximum-a-posteriori of their distributions. Bayesian matching pursuit has better recovery accuracy but higher complexity.

These algorithms only improve reconstruction speed and accuracy, how to adapt to the problem of defect pattern extraction is another key issue. Other algorithms cannot deal with the CS data directly because it is transformed and compressed version of the original data. However, the measurement results in former chapters are sampled with 0/1 Bernoulli matrices which leads to one special case, i.e. the measurement results are a downsampling version of the original signal. It is also the foundation for the qualitative defect detection methods in section 5.1. Based on the algorithm in Figure 5.2, the CS data can be converted into binary values (as shown in Figure 5.8) which gives possible application opportunity for some methods like water filling algorithm [185] and the widely-used image smoothing [160, 186]. Water filling algorithm is originally from the communication applications. The basic idea is filling the gaps that are connected just like water always fill the low altitude area. This method is feasible because the measurement matrix defines the dam for water filling. Figure 5.8 shows the sampling location with light blue points. Only gaps between sampling locations can be filled. The idea of image smoothing is the local areas in the binary version of the CS data where have more ‘1’ will have larger average values, thresholding the smoothing results can get the overall binary pattern. However, the water filling algorithm is not robust to noise which leads to a false alarm. The binary defect pattern from the image smoothing method is too sensitive to the smoothing scale and the threshold value that obtaining a binary pattern, which degrades the reliability.

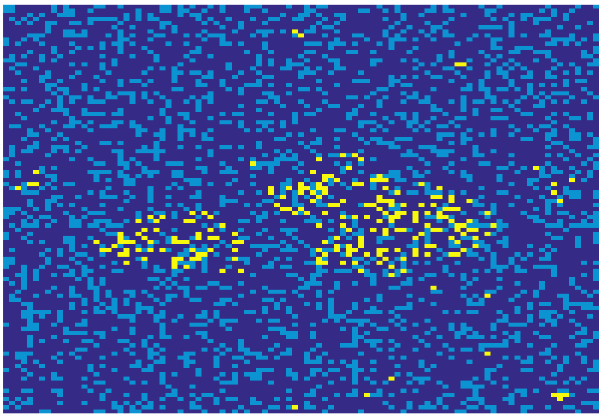

Figure 5.8 The binary version of CS data (The yellow points) and the sampling location (the light blue points)

5.2.2 The proposed spOMP for quantitative impact damage detection

Given the drawbacks of sparse reconstruction methods and non-reconstruction method like water filling in feature extraction. This section proposes quantitative defect detection methods, i.e. to extract the binary defect pattern from the CS data. Compared to the sparse reconstruction algorithms+HTED algorithm method in Chapter 3, the method in this section is much more time-efficient because the damage pattern is reconstructed directly from the CS data rather than post-extraction from the reconstructed data. A sparse OMP (spOMP) is proposed which is far more time-efficient than the OMP algorithm. It is also more time-efficient than the CoSaMP because spOMP do not need to remove the wrong support in each iteration. The overall diagram for these binary defect pattern detection methods is shown in Figure 5.9.

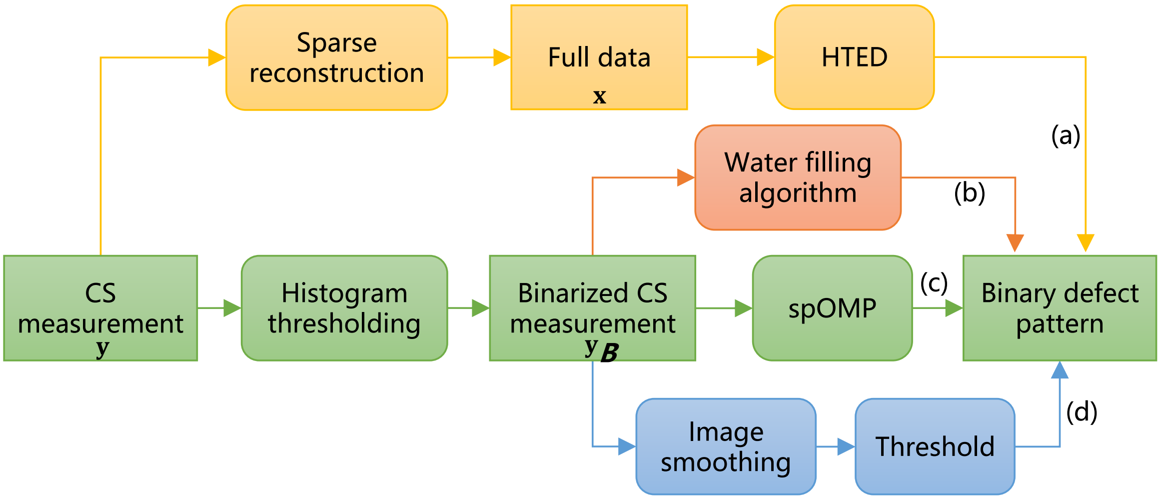

Figure 5.9 Methodology diagram for (a) sparse reconstruction + HTED-based method, (b) water filling algorithm, (c) the proposed spOMP based method, (d) Image smoothing method.

As shown in Figure 5.9, instead of recovery the original data, the proposed method converts the CS data into binary values using a similar method as section 5.1. The data which classified as defect is converted into '1'. Then $\mathbf{y}_{\mathrm{B}}$ are taking as the input for the proposed reconstruction algorithm. Note that this is fundamentally different from the so-called 1-bit compressed sensing or binary CS problem [187-189]. The goal for 1-bit CS is recovering the original float value $\mathbf{x}$ with $\mathbf{y}_{\mathrm{B}}$ while the proposed spOMP algorithm only reconstructs the binary defect.

Figure 5.10 shows the proposed spOMP algorithm. It is a modified version of stOMP and OMP in order to take advantage of the signal characteristic in this system. Firstly, the input measurement results are binary values for spOMP rather than arbitrary values for de-noising purposes. As shown in Figure 5.8, there is some small cluster of 'defect locations' which are false-alarm, because the defect of a low impact energy is usually gathering together around the impact point instead of scattering widely. These wrong defect locations are noise for the true defect location. They are caused by measurement noise or quantisation error when converting to binary. The reason why spOMP has de-noising ability is that the greedy algorithm progressively selects the atom of $\mathbf{A}$ to represent $\mathbf{y}$, and to represent $\mathbf{x}$ as a result. The most related atom will be selected earlier than the less related atom. Noise is in high frequency and small amount compared to the overall image. When using frequency-related matrix (such as DCT and DWT) as the sparse basis, the measurement matrix $\mathbf{A}$ contains the frequency information. So, the low-frequency atom will be selected to represent $\mathbf{x}$ before the high-frequency atom is selected. The noise will not be recovered by properly defined the stop criteria.

Algorithm: Sparse orthogonal matching pursuit (spOMP)

Input: $\mathbf{y} \in \mathbb{B}^{m\times 1}$: Binary measurement results;
$\mathbf{A} \in \mathbb{R}^{n\times 1}$: measurement matrix;
$0 < \gamma < 1$: Threshold value for stop iteration;
$\mathbf{\Psi}$: Sparse basis.

Output: $\mathbf{x} \in \mathbb{B}^{n\times 1}$

Initialization: $\mathbf{r} = \mathbf{y}$, $\Lambda = \emptyset$, $M = 1$, $0 < \{\rho_1, \rho_2\} < 1$;
while $M > \gamma$ **do**
  Orthogonal projection: $\mathbf{C} = \frac{|\langle \mathbf{A}_i, \mathbf{r}\rangle|}{\|\mathbf{A}_i\|_{\ell 2}}, i \in \{1, 2, 3, ..., n\}$
  Identify sparse support:
  $\Lambda_\Delta =$ indices of all $\mathbf{C}_{\tilde{\Lambda}} > \rho_1 \max(\mathbf{C}_{\tilde{\Lambda}})$, $\tilde{\Lambda}$ is the complementary set of Λ;
  S= sort $\frac{\mathbf{C}_{\Lambda_\Delta}}{\max(\mathbf{C}_{\Lambda_\Delta})}$ in ascend order. **I** is the sorted indices
  for $j = 1$ *to* (*length of S*) $- 1$ **do**
    $d_j = S_{j+1} - S_j$;
    Λ_Δ = remove I_j from Λ_Δ;
    if $d_j > \rho_2$ **then**
      break;
    end
  end
  Update:
  $\Lambda = \Lambda \cup \Lambda_\Delta$;
  Perform least square estimation: $\hat{\mathbf{x}} = \left(\mathbf{A}_\Lambda^T \mathbf{A}_\Lambda\right)^{-1} \mathbf{A}_\Lambda^T \mathbf{y}$;
  $\hat{\mathbf{y}} = \mathbf{A}_\Lambda \hat{\mathbf{x}}$;
  $M = \frac{\sum abs(\mathbf{y} - \varepsilon(\hat{\mathbf{y}} - 0.5))}{m}$;
  $\mathbf{r} = \mathbf{y} - \hat{\mathbf{y}}$.
end
$\mathbf{x} = \varepsilon\left(\mathbf{\Psi}\hat{\mathbf{x}} - 0.5\right)$.

Figure 5.10 The proposed spOMP algorithm

Secondly, although conventional greedy algorithms can be used to fulfil the de-noising purpose, their performance is varying with the different signal characteristic. Recovery performance can be improved by taking the signal characteristic into consideration. Figure 5.11 depicts the sorted normalised **C** after four iterations using the conventional stOMP algorithm using the binary measurement matrix as input. The curves show sparse property because there is rapid dropping at the beginning of each curve. Traditional algorithm fails to make use of this property. For example, OMP only selects the atom corresponding to the largest **C**, which is slow. gOMP choose that with the largest *L*, stOMP chooses that when **C** above one threshold. Both improve efficiency. However, the *L* and threshold do not adapt to the sparse level of **C** after each iteration, which easily leads to the wrong atom. Other algorithms which removing the wrong atom in each iteration compromise the efficiency. So, the proposed spOMP algorithm proposed a method of making use of the sparse of $\mathbf{C}$ to adaptively identify the sparse support in each iteration.

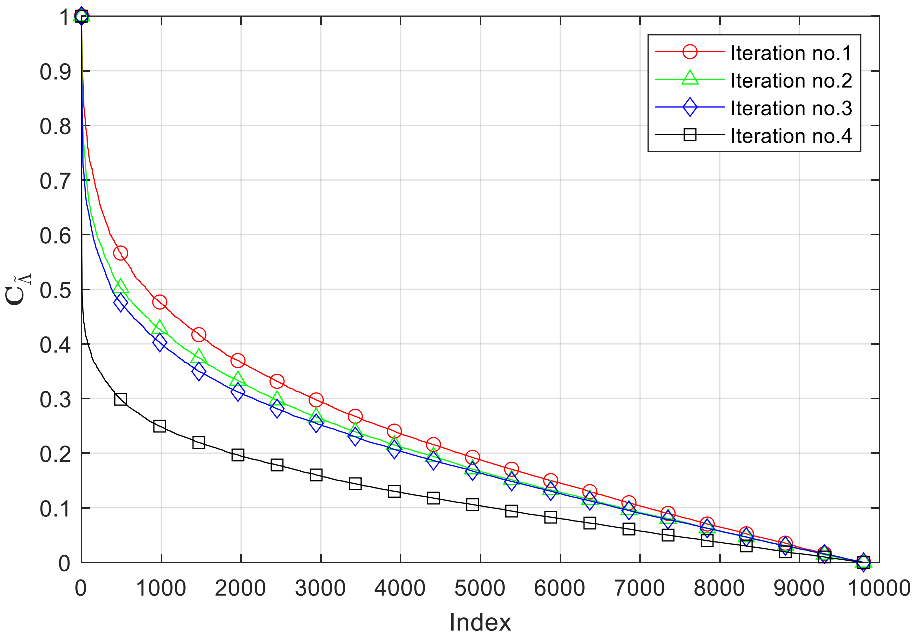

Figure 5.11 Sorted normalised $\mathbf{C}_{\tilde{\Lambda}}$ *after several iterations using stOMP*

The proposed spOMP first selects the atoms which above $\rho_1 \max(\mathbf{C}_{\tilde{\Lambda}})$. Then sort the selected supports in ascending order with normalisation. In the following *For* loop, the differences of neighbour elements are calculated. If the difference is above one threshold ρ_2, jump out the loop so that the tail of selected atoms is cut, i.e., only the sparse atoms are selected. The operation in *For* loop and the ascend order make sure that the difference operation is calculated from the tail side rather than the head side, because the tail is smoother. The *For* loop is imposing on the $\mathbf{C}_{\Lambda_\Delta}$ rather than the whole $\mathbf{C}_{\tilde{\Lambda}}$ to keep a low overhead for *sort* and calculate difference operation. The parameter ρ_1 and ρ_2 will influence the selected support. ρ_1 decides the computation overhead in the *For* loop. When ρ_1 = 1, the support selection method for spOMP is same as OMP, the *For* loop do nothing. When ρ_1 = 0, the For loop need to deal with the whole $\mathbf{C}_{\tilde{\Lambda}}$. Smaller ρ_1 usually leads to higher computation overhead, but too large ρ_1 will decrease the efficiency for the overall algorithm. Given the sparse of $\mathbf{C}_{\tilde{\Lambda}}$, ρ_1 = 0.05~0.1 is recommended configuration. It is the same as the frequent use of 0.9~0.95 for enough confidence. The end of sparse components location is where there is a significant jump in the sorted $\mathbf{C}_{\Lambda_\Delta}$, ρ_2 quantifies how significant the jump is. $\rho_2 = 0.05$ is recommend a configuration for enough confidence.

In addition to the modified input and the support identification methods, the stop criteria are also modified according to the system needs. Traditional greedy algorithms use a pre-defined stop threshold γ to constrain the residual level by $\mathbf{r}^T\mathbf{r} < \gamma$, or limit the iteration number to the signal sparsity *K* if it is a priori information. The latter cannot be applied to this system because *K* is unknown. How to define γ based on the system needs is the key issue. The purpose of this spOMP-based method for quantitative defect detection is to get the binary defect pattern without incurring artefacts. The proposed stOMP measures the similarity between **y** and the sampled **y** in the reconstructed binary pattern by step 18 in Figure 5.10. This similarity is within the scope of 0 to 1, so there is one constraint 0< γ <1 for the algorithm input. 95% of similarity is recommended to prevent incurring significant artefacts. Finally, the defect pattern is obtained easily by thresholding the reconstructed $\boldsymbol{\Psi}\hat{\mathbf{x}}$ with a threshold value of 0.5 due to the binary **y**.

5.2.3 Experimental setup for the proposed spOMP-based quantitative detection

Qualitative and quantitative comparison between the existing method and the proposed methods is carried out for validation. In order to compare with the previous results, the same frequency frame as previous sections is chosen to extract the damage pattern. The raster scan data is used to extract a reference defect pattern with the proposed HTED algorithm in section 3.2.3. To speed up the validation process, equivalent CS sampling data is obtained by randomly sampling the raster scan frame with different 0/1 Bernoulli measurement matrix. Gaussian noise is added to the CS measurement results.

5.2.4 Evaluation results for the proposed spOMP-based quantitative detection

Following the evaluation process in the last subsection, Figure 5.12 presents the sampling location, quantified '1' in the measurement results and the extracted pattern under three different sampling percentage. The yellow stars that apart from the sampling pattern are noise due to the measurement noise and quantification noise. These noise defect points are automatically removed in the final defect pattern, which validates the denoising ability of the proposed methods. Even just 5% of sampling points already shows a general defect pattern, which demonstrates the downsampling ability.

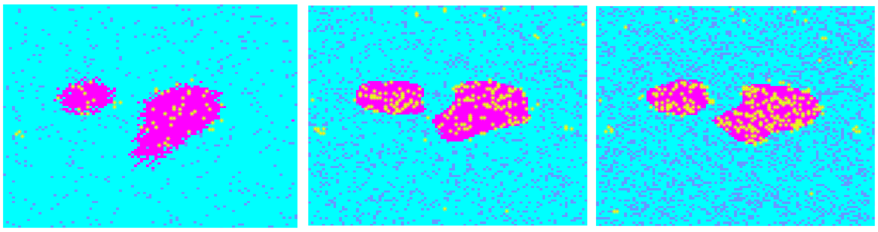

(a) (b) (c)

Figure 5.12 Sampling and recovery results under (a) 5%, (b) 15%, (c) 25% of sampling percentage. The blue points are sampling locations, and the yellow stars are the sampling point which is quantified as '1'. The red pattern is the extracted defect pattern.

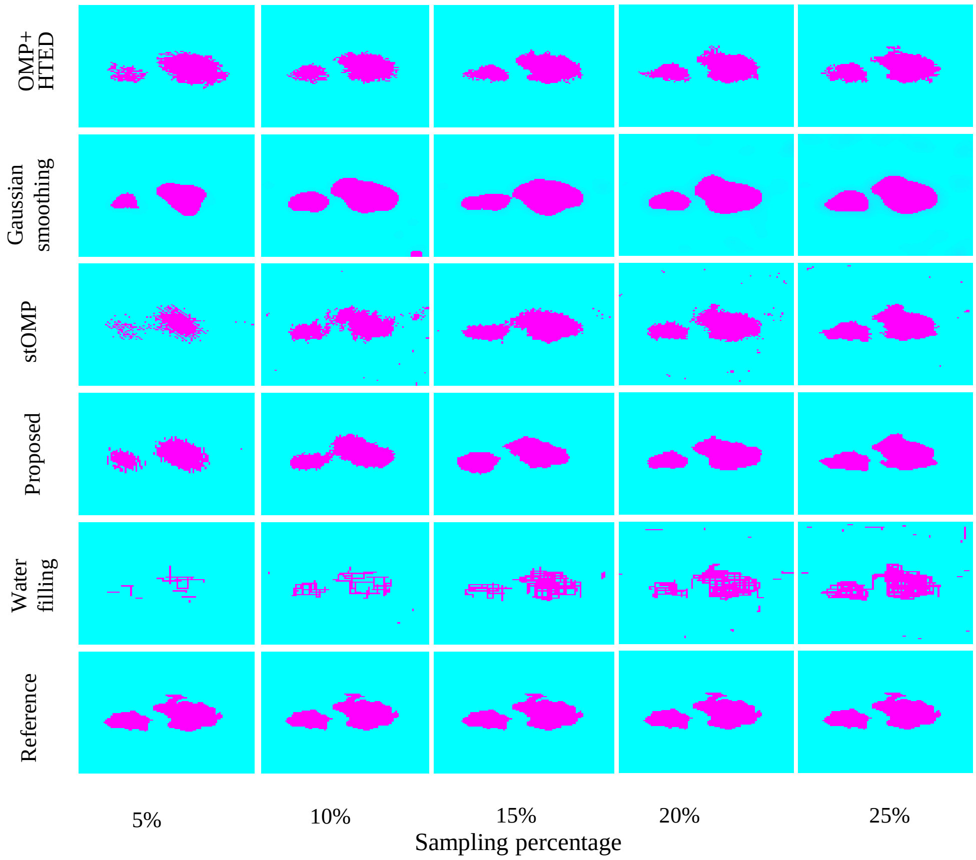

Figure 5.13 Qualitative comparison of extracted defect pattern for the 6J specimen with different methods

The proposed method is compared with the water filling algorithm, image smoothing algorithm, and OMP+ HTED algorithm as shown in Figure 5.9. It is also compared with stOMP algorithm which uses binary measurements as input, and sets the same stop criteria to validate the support selection performance of the proposed spOMP algorithm. The defect pattern extraction results for these methods under 6J specimen are shown in Figure 5.13. The baseline defect pattern is extracted on raster scan data with HTED algorithm. The water filling results are worst among these methods. The Gaussian smoothing results obtain smooth defect patterns even under low sampling percentage. However, the Gaussian smoothing method can only obtain a smooth image, which losses the detail information. stOMP algorithm incurs some artefacts. Both the OMP+HTED algorithm and the proposed spOMP algorithm presents clean defect pattern and more detail methods than others.

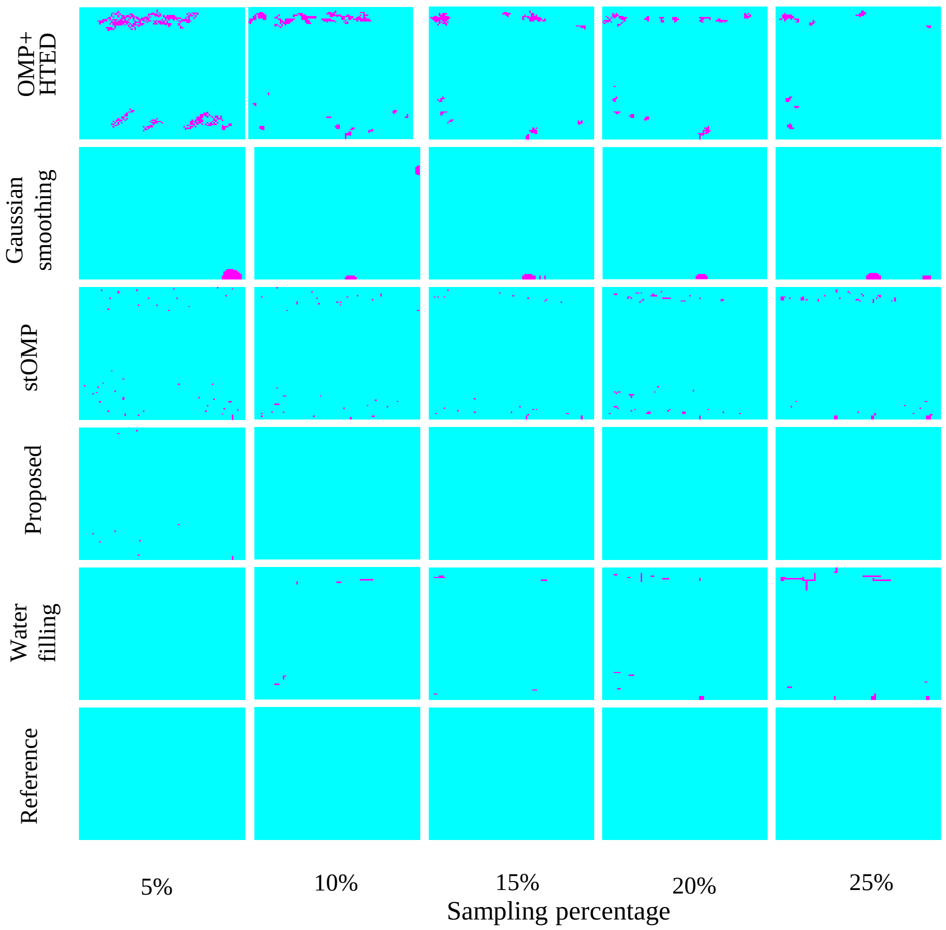

Figure 5.14 Qualitative comparison of extracted defect pattern for a non-defect area with different methods

Another set of comparison in Figure 5.14 is performed on non-defect areas to compare the de-noising ability for various methods. The water filling methods and stOMP algorithm increase the artefacts with more sampling percentage. Because the water filling method only fills the gap within a certain distance from the quantified defect points (the yellow stars in Figure 5.12). Fewer pixels will be filled under a low sampling rate. The stOMP algorithm easily leads to wrong supports with large L, which brings in error propagation. The Gaussian smoothing shows constant artefacts, because when there are few pixels been quantified as ‘1’, the smoothing results around the defect point shows very flat Gaussian distribution. Threshold these results easily leads to a large area of wrong defect pattern.

For quantitative validation, repeated sampling under the same sampling percentage with different sampling locations is carried out to get average performance. The extracted defect pattern for different methods is compared with the baseline. The normalised hamming distance is used as a parameter because they are binary values and there is no spatial shift or rotation for the sampling area. It is defined as the ratio of the number of different values divided by the total signal length. The average comparison results for different defect specimens are shown in Figure 5.15. All methods converge into low hamming distance except the Gaussian smoothing, because the Gaussian smoothing method loss the sharp details. The proposed spOMP algorithm shows lower hamming distance than the stOMP algorithm and has similar performance with the OMP+HTED algorithm.

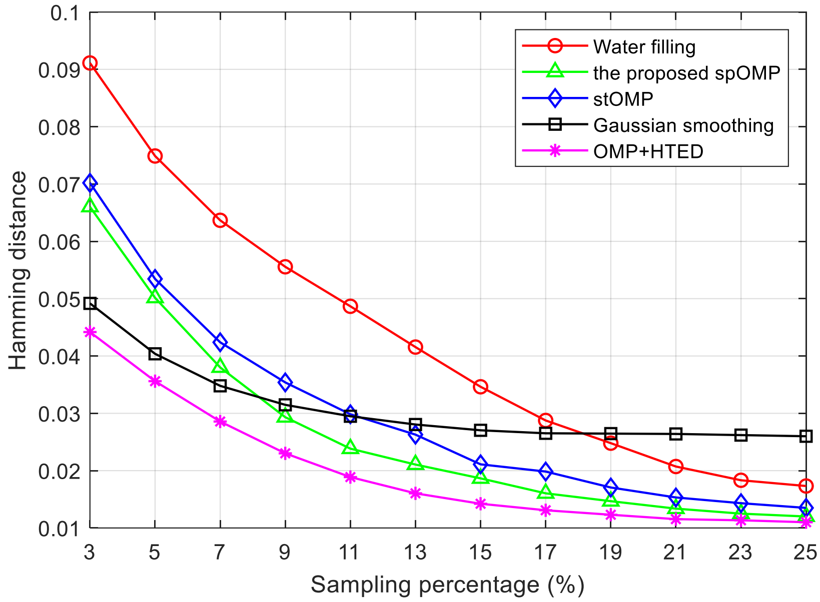

Figure 5.15 Average normalised hamming distance between the defect from various methods and the reference one.

The average hamming distance on non-defect area is shown in Figure 5.16. These results are in line with the results in Figure 5.14. The hamming distance for the water filling and Gaussian smoothing are rising with the sampling percentage. OMP+HTED algorithm shows decrease in the hamming distance, but the Gaussian smoothing keeps a constant error. The proposed stOMP algorithm has the lowest hamming distance, because the specially designed stop criteria and denoising ability with binary input.

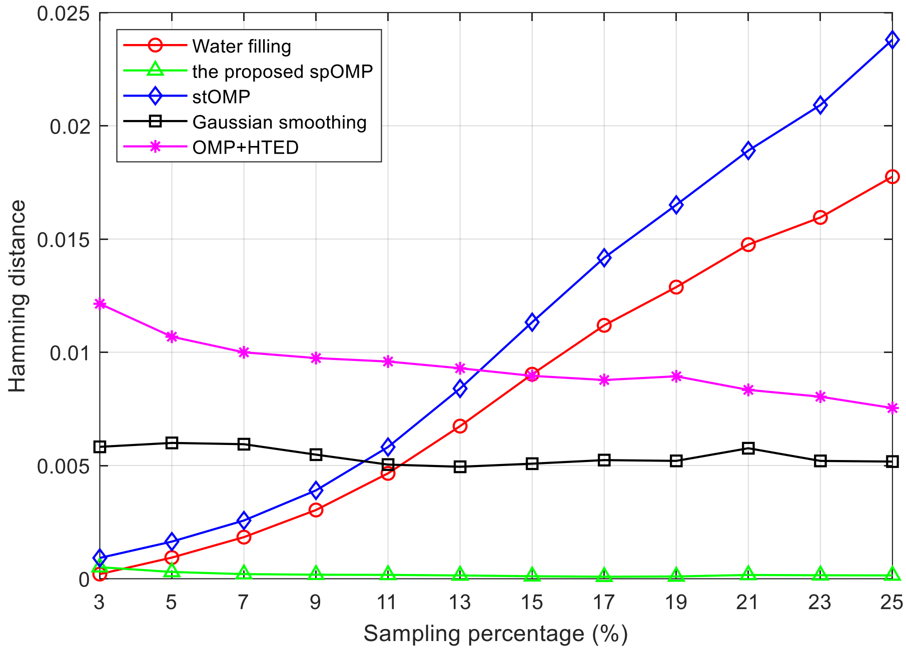

Figure 5.16 Average normalised hamming distance between the defect detection results of the non-defect area from various methods and the reference one.

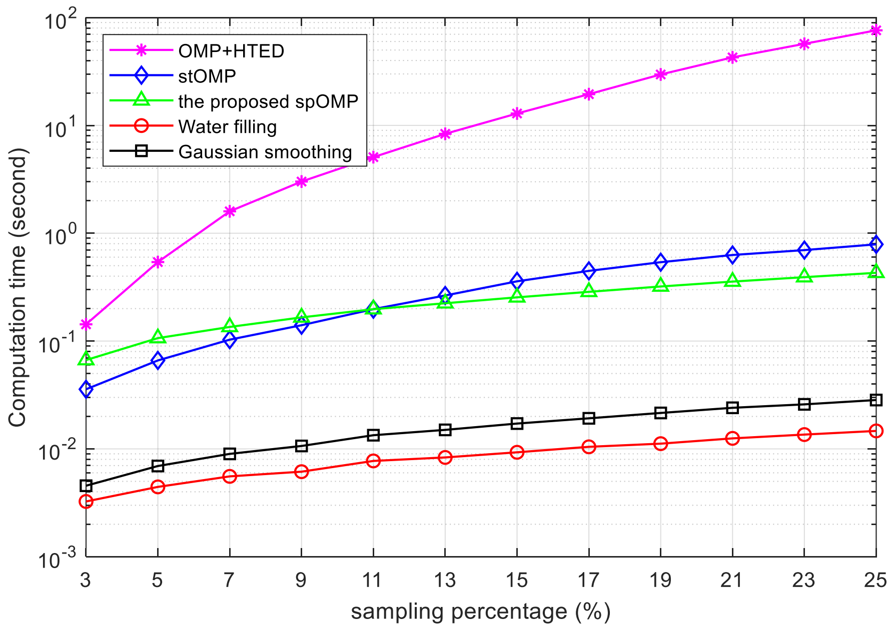

Figure 5.17 Computation time for different algorithms

In terms of time efficiency, the running time on the same PC and same configuration in Matlab are adopted. The computer has Intel Core i7-7500u CPU and 8GB of memory. The running time is logged with the 'tic' and 'toc' command in Matlab for different algorithm section. The average computation time for these algorithms is given in Figure 5.17. The Gaussian smoothing and water filling algorithm have the least computation time. Among the sparse reconstruction algorithms, the proposed spOMP algorithm has the least time. It is reduced by one order of magnitude compared to the stOMP algorithm. OMP takes the most time because it only finds one atom in each iteration.

5.3 Chapter Summary

This chapter presents how CS could help improve feature extraction robustness and efficiency even without reconstruction of CS data. Qualitative and quantitative defect detection from CS measurements is investigated. The qualitative defect detection algorithm uses histogram thresholding to give binary defect information. Since the CS data obtained are a random downsampling version of the complete data with 0/1 Bernoulli matrix, which means the histogram is invariant to the downsampling. The validation results demonstrate the proposed qualitative defect detection methods have better precision, recall, the probability of detection and accuracy than other downsampling methods. A new greedy algorithm of sparse orthogonal matching pursuit (spOMP) for quantitative defect detection which integrates defect pattern extraction with sparse reconstruction is proposed. The spOMP takes binarisation results of the CS measurement data using the histogram thresholding method in qualitative defect detection. The supports are selected based on the sparsity of residual projection results. The stop criteria are specialised by the system needs of defect pattern extraction. The proposed spOMP algorithm has similar feature extraction accuracy as the OMP+HTED algorithm in Chapter 3, and spOMP has significantly higher denoising ability and lower-time consumption.

However, the proposed qualitative detection method is for the proposed CS measurement process. The CS measurement is based on customised 0/1 Bernoulli measurement matrix, which makes the sampled data a subversion of the whole data. If other measurement matrices are used, this direct histogram thresholding method may not useful. More investigation on methods that suitable for other general measurement matrices is a potential improvement. The proposed spOMP algorithm needs the binarized measurement results as input, and the output results are the binary results. This is useful for applications where only binary results are needed, like the defect region and text extraction.

Chapter 6. Conclusions and Future Works

This final chapter summarise the research. The conclusions are drawn on the potentials of compressed sensing as solutions of more time-efficient sensing and robust feature extraction for open-ended waveguide NDT&E. The outlooks on the future works are outlined in terms of improving the CS model in this thesis, real-time data acquisition and high-order feature extraction.

6.1 Conclusions

Traditional open-ended waveguide non-destructive testing and evaluation systems suffer from several critical challenges. Firstly, they have time-consuming data acquisition by raster scan, which prevents on-line detection. Secondly, the traditional OEW NDT&E systems acquire data without considering the needs in the feature extraction process, which leads to a large amount of data and processing overhead for feature extraction. Thirdly, efficient defect region segmentation in the obtained image is also challenging due to the complex the image background like texture. Compressed sensing demonstrates impressive compression ability in various applications using sparse models. It is a potential solution to address these challenges in OEW NDT&E systems with proper sparse representation. This thesis develops CS models for OEW NDT&E that jointly considers sensing & processing regarding fast data acquisition, data compression, and robust feature extraction. For this purpose, the following works are carried out, and the related conclusions are drawn.

A literature review is carried out for the state-of-the-art CS techniques in solving NDT problems. Firstly, a review of CS theory regarding its sparse representation, measurement matrix design and sparse reconstruction is carried out. The review indicates random Bernoulli and Gaussian matrix can work as the universal measurement matrix, because they are uncorrelated with most sparse bases. As for sparse reconstruction, the greedy algorithms such as OMP have good trade-off among the required measurement number, accuracy and time-efficiency. These two observations support designing Bernoulli measurement matrix and reconstructing with greedy algorithms in this thesis. Secondly, a review on NDT systems that use CS in their sensing, feature extraction, and classification stage is carried out in section 2.5. The review indicates that there is no CS design in open-ended waveguide systems for NDT&E, and CS in NDT applications are still in its infancy. For the challenge of reducing scanning time and data amount, CS witnesses few applications in similar NDT systems like laser scanning, and the other hardware designs like rotating masks in THz imaging are expensive and bulky. More importantly, the sensing stage in these literature still disregard the needs of the latter feature extraction. For example, how to optimise the measurement number according to the interested features without knowing the sparsity K? From the feature extraction sides, there are few works in literature using the difference of image from health sample and defect sample for damage localisation; they can be used to segment the damage region in open-ended waveguide systems. However, they are not robust to complex image background such as texture.

The research work started by building the case study system. This part is presented in Chapter 3. An open-ended rectangular waveguide probe is used for low-energy impact damage detection on CFRP materials. The waveguide probe is connected to VNA to get excitation signal and measures the reflection coefficients. The probe is carried by a scanner to scan arbitrary location. The CFRP materials for study have 12 layers of 5H satin balanced carbon fibre woven fabrics, it is manufactured by TenCate Advance Composites, Netherlands. Five specimens are made with an impact energy of 2J, 4J, 6J, 8J, 10J. They have the same size of $100\times130\ mm^2$ and with $3.78\mp0.05\ mm$ of average thickness. The impact energy is generated by a free-falling hammer with different height. Raster scan is performed on each specimen as a baseline, and raster scan data is used for the latter sparse analysis.

Major work of this thesis is detailed with three individual chapters as follows:

A CS-based on-line detection model for open-ended waveguide NDT systems which gives a solution to the challenge of time-consuming data acquisition and the demand for on-line detection is developed. The related contents are given in Chapter 3. The model integrates sampling and evaluation for the first time in CFRP structure integrity evaluation using open-ended waveguide imaging. Compared to traditional raster scan designs which require complete spatial scanning for defect evaluation, this model achieves defect extraction in the data acquisition process without any hardware modification, thus forming an on-line process. A case study in impact damage detection for CFRP structure using open-ended rectangular waveguide probe is carried out for validation. The spatial images for CFRP specimens are sparse in DCT basis in the case study. A customised 0/1 Bernoulli measurement matrix is designed for downsampling under CS scenario based on this sparse condition. This downsampling data and

DCT basis, as well as the designed measurement matrix, is used to reconstruct the missing pixels with orthogonal matching pursuit algorithm. To address the issue of hard to determine the sampling pixel numbers that required for reconstruction, an accumulated sampling process is developed. The measurement number is decided by the quality of the reconstructed image. When the reconstructed image is stable enough, the defect pattern is extracted with the proposed histogram threshold edge detection (HTED) algorithm. The case study shows that HTED algorithm is robust to texture and lift-off distance variation comparing to other image segmentation methods, and the data acquisition time and data amount is reduced to m/n of raster scan while maintaining equivalent image quality and defect region as that of the traditional raster scan. There are additional advantages for the proposed on-line CS model. Firstly, this is a software algorithm, which means no hardware update is needed for open-ended waveguide NDT system while improving scanning efficiency. Secondly, compressed sensing recovers the whole image with only a fraction of sparse samples, which makes this framework also applicable for situations where the sampled data is partially lost using a sparse representation, e.g., data recovery from fault nodes in large-scale sensor networks. This part of the work is published on IEEE Transactions on Industrial Electronics.

A feature-supervised data acquisition model which gives a solution to the challenge of reserving the feature quality while reducing data/computation overhead efficiently for feature extraction is developed. The related contents are given in Chapter 4. FsCS reduces the data amount for feature extraction and improves spatial image reconstruction speed with joint reconstruction. The frequencies which reveal the feature only occupy a small part of the frequency band, this method finds this sparse frequency range firstly to supervise the latter sampling process. Subsequently, based on joint sparsity of neighbour frame, an aligned spatial-spectrum sampling scheme is proposed to only sample interested frequency range for required features by using a customised 0/1 Bernoulli measurement matrix. The interested spectral-spatial data are reconstructed jointly which has much faster speed than frame-by-frame methods. The case study in impact damage detection on CFRP materials with open-ended rectangular waveguide shows that the data amount is reduced greatly without compromising feature quality. The gain in time-efficiency increases almost linearly with the number of sampling points comparing to sequential reconstruction. This part of work is submitted to IEEE Transactions on Instrumentation and Measurement.

Qualitative and quantitative damage detection models that give a solution to the challenge of robust and time-efficient feature extraction are developed. Related contents are given in Chapter 5. The qualitative method which detects damage in CS data directly without reconstructing the whole spatial data is developed. It uses histogram thresholding to give binary defect information. Since the CS data obtained are a random downsampling version of the complete data with 0/1 Bernoulli matrix, which means the histogram is invariant to the downsampling. The validation results demonstrate the proposed qualitative defect detection methods have better precision, recall, the probability of detection and accuracy than other downsampling methods. To directly extract the damage region from CS data rather than from the reconstructed whole spatial data as HTED, the proposed quantitative impact damage detection method first uses the proposed qualitative detection method to binarize the measured data, which achieves denoising ability. Secondly, a CS sparse reconstruction algorithm called sparse orthogonal matching pursuit (spOMP) is proposed to extract the defect region, because the conventional CS reconstruction algorithms cannot properly use the sparse character of residual projection on the measurement matrix. The spOMP takes binarisation results of the CS measurement data as input, and it defines a support identification scheme and stop criteria according to the goal of impact region segmentation. It improves time-efficient by integrating the reconstruction process with the defect region extraction process and selects multiple supports than OMP. Meanwhile, the high denoising ability of spOMP is guaranteed by only selecting atoms that significantly contributes to the measured data, and properly defines the iteration stop criteria with a threshold on the hamming distance between the measurement results and the explained results. The proposed spOMP algorithm has similar feature extraction performance as the OMP+HTED algorithm in Chapter 3 but with significantly higher denoising ability and lower-time consumption. This part of work is presented in the 23rd International Workshop on Electromagnetic Nondestructive Evaluation, Michigan, USA, 2018 and forms one paper for it.

6.2 Future Works

Smart sensing technologies that efficiently support the decision-making in NDT&E is increasingly important. Task-oriented compressed sensing is the future direction for compressed sensing research for the next 10 to 15 year [2], it is a promising solution to efficiently support decision-making by integrating sensing and processing. This thesis only paves a way to compressed sensing that integrates the demand of open-ended waveguide NDT system with sensing. It is impossible to be perfect solutions for current work, which requires more efforts to refine it and dig its potential. For the investigation system in this thesis, some future works that deal with the limitation that mentioned in chapter summaries of the proposed methods are:

(1) For the on-line CS model in Chapter 3, it is worth noting that the image recovery process in the accumulated sampling & recovery block may take a relatively long time, although it is already much faster than raster scan. Developing new sampling model which reduces the reconstruction overhead like the method in chapter 4 is one potential future work. The idea is to reduce the data that need to be reconstructed, and the reduction can be supervised by the final quantitative feature that specific application looks for.

(2) Also for the work in Chapter 3, the proposed stability detection method relies on the reconstructed image for each iteration, and it works as the stop rule for the accumulated sampling process. Investigating one way that can directly use the CS sampled data as input rather than the constructed image is a potential improvement for this method, because repeat the reconstruction is a relatively time-consuming process.

(3) The work in Chapter 4 uses the frequency location of the feature as one supervise condition, this location information is obtained by the result of feature data screening function $f(\cdot)$. The proposed method builds up a compressed sensing model to substitute $f(\cdot)$. To push this idea further, combing the feature extraction process $g(\cdot)$ with $f(\cdot)$, and use the final quantitative feature as a supervision condition for the sensing process are more helpful to the task-oriented sensing vision. In the case study system in this thesis, the final quantitative feature is the location and binary shape of the damage region. Investigating proper modelling and sparse representation to it, and use it as one condition to supervise the sensing will minimise the data redundancy and maximise the storage and time efficiency.

(4) The proposed qualitative detection method in Chapter 5 is for the proposed CS measurement process in this thesis. The CS measurement is based on customised 0/1 Bernoulli measurement matrix, which makes the sampled data a subversion of the whole data. If other measurement matrices are used, this direct histogram thresholding method may not useful. More investigation on methods that suitable for other general measurement matrix is a potential improvement.

For the more broaden filed of CS application in the NDT field, here are some heights for future works.

(1) Develop real-time CS data acquisition for waveguide NDT systems. This thesis improves scanning speed than traditional raster scan with CS downsampling. However, the bulky and power-consuming mechanical scanner systems are difficult to be applied to the practical monitoring applications including real-time acquisition. Developing scan-free waveguide systems is beneficial for real-time and low-cost monitoring applications. One potential solution is to design a focus lens structure using metasurface to project local defect information into the far-field. Some initial simulation already done by the author of this thesis, and the work is presented in the conference 2018 Far East NDT New Technology & Application Forum (FENDT), Xiamen, China. In summary, a meta-surface that consists of ELC resonator [190] is proposed. This kind of metallic structures can be used for NDT applications, which have the same principle for the radio frequency identification (RFID) -based NDT systems [191-194]. These systems use an electromagnetic coupling between the tag antenna (the metallic structure) and the SUT for defect detection. A sensor captures spectrum data with a single snapshot using a wideband excitation signal in nearly real-time in the far-field. CS measurement matrix is obtained by calibration with a standard defect sample. Defect information is extracted directly from the captured data with sparse reconstruction.

(2) Investigate feature-supervise sensing for high-order features. This thesis chooses the impact damage region as damage feature; this feature can be only extracted in some frames in the whole spatial-spectral data. So the proposed FsCS model only samples the part of data that will finally be used for damage region segmentation, thus achieving feature-supervised sensing. However, high-order features are more robust to noise and interfaces for decision-making. For example, PCA can be used on multiple frames of waveguide NDT images to extract more robust features. There is also some literature that use deep learning to learn feature automatically as shown in the review chapter. How to optimise the sensing scheme to obtain these high-order features in a time/storage/processing efficient manner is a remaining issue.

(3) Combining CS with artificial intelligence has the potential to reduce expert work in extracting features and classifying feature. CS and AI already show some intersection. For example, there is some literature that use machine learning to automatically learn features from CS data, and classify features to different defect type. The machine learning helps sparse representation in dictionary learning, and defect classification can be implemented with the idea of sparse representation. Furthermore, some combinatorial algorithms in the machine learning side are used for sparse reconstruction. More investigations in NDT applications that combine sparse models and AI contributes to the future predictive maintenance business model.

(4) Lack of hardware implementation for CS measurement. As is shown in the review section, there only a little hardware implementation for CS measurement in NDT applications, especially for time and frequency domain signal. Without the hardware support for data acquisition, the advantage of data compression in sensing cannot be achieved. This thesis develops CS down-sampling models with customised 0/1 Bernoulli measurement matrix to substitute raster scan, the measurement can be implemented with a scanner. Borrow ideas from medical application side is a potential solution, because CS and many medical sensing are computational sensing in nature. For example, MRI devices measure the Fourier transform coefficients directly, and the MRI image is sparse on the DCT domain.

(5) Lack of hardware support for sparse reconstruction. It is worth noting that the image recovery process may take a relatively long time. For example, recovery whole reflection coefficients using 18% of sampling percentage takes around 2 minutes on a Windows computer with Intel® Core™ i5-4690K CPU with OMP algorithm. This time is far less than raster scanning. This issue can be solved with the development of cloud computing and supercomputer, which is an essential part of the new industrial mode in the Internet of Things vision. More fundamentally, developing hardware processing unit and parallel reconstruction framework that specialised for sparse reconstruction is of great benefit. Just like the hardware unit for machine learning like Neural Processing Unit (NPU) that built in smartphone CPU like Kirin 980 from Huawei, and Google's Tensor Processing Unit (TPU).

References

[1] E. Kallinikidou, H.-B. Yun, S. F. Masri, J. P. Caffrey, and L.-H. Sheng, "Application of Orthogonal Decomposition Approaches to Long-Term Monitoring of Infrastructure Systems," *Journal of Engineering Mechanics,* vol. 139, no. 6, pp. 678-690, 2013.

[2] R. C. G. Sapiro, "Future Directions in Compressed Sensing and the Integration of Sensing and Processing," *Future Direction Workshop,* 2016.

[3] C. A. Tokognon, B. Gao, G. Y. Tian, and Y. Yan, "Structural Health Monitoring Framework Based on Internet of Things: A Survey," *IEEE Internet of Things Journal,* vol. 4, no. 3, pp. 619-635, 2017.

[4] J. Lin, W. Yu, N. Zhang, X. Yang, H. Zhang, and W. Zhao, "A Survey on Internet of Things: Architecture, Enabling Technologies, Security and Privacy, and Applications," *IEEE Internet of Things Journal,* vol. 4, no. 5, pp. 1125-1142, 2017.

[5] S. K. Dwivedi, M. Vishwakarma, and P. A. Soni, "Advances and Researches on Non Destructive Testing: A Review," *Materials Today: Proceedings,* vol. 5, no. 2, Part 1, pp. 3690-3698, 2018.

[6] B. Gao, W. L. Woo, G. Y. Tian, and H. Zhang, "Unsupervised Diagnostic and Monitoring of Defects Using Waveguide Imaging With Adaptive Sparse Representation," *IEEE Transactions on Industrial Informatics,* vol. 12, no. 1, pp. 405-416, 2016.

[7] R. Mirzavand, M. M. Honari, and P. Mousavi, "High-Resolution Balanced Microwave Material Sensor with Extended Dielectric Range," *IEEE Transactions on Industrial Electronics,* vol. 64, no. 2, pp. 1552-1560, 2017.

[8] E. J. Candès, J. Romberg, and T. Tao, "Robust uncertainty principles: Exact signal reconstruction from highly incomplete frequency information," *Information Theory, IEEE Transactions on*, vol. 52, no. 2, pp. 489-509, 2006.

[9] S. Qaisar, R. M. Bilal, W. Iqbal, M. Naureen, and S. Lee, "Compressive sensing: From theory to applications, a survey," *Communications and Networks, Journal of,* vol. 15, no. 5, pp. 443-456, 2013.

[10] M. Rani, S. B. Dhok, and R. B. Deshmukh, "A Systematic Review of Compressive Sensing: Concepts, Implementations and Applications," *IEEE Access,* vol. 6, pp. 4875-4894, 2018.

[11] D. Takhar, J. N. Laska, M. B. Wakin, M. F. Duarte, D. Baron, S. Sarvotham, *et al.*, "A new compressive imaging camera architecture using optical-domain compression," in *Electronic Imaging 2006*, 2006, pp. 606509-606509-10.

[12] M. J. Sun, M. P. Edgar, G. M. Gibson, B. Sun, N. Radwell, R. Lamb, *et al.*, "Single-pixel three-dimensional imaging with time-based depth resolution," *Nature Communications,* vol. 7, p. 12010, 2016.

[13] L. Wang, L. Li, Y. Li, H. C. Zhang, and T. J. Cui, "Single-shot and single-sensor high/super-resolution microwave imaging based on metasurface," *Scientific Reports,* vol. 6, p. 26959, 2016.

[14] Y. Lu and Y. Wang, "Monitoring temperature in additive manufacturing with physics-based compressive sensing," *Journal of Manufacturing Systems,* vol. 48, pp. 60-70, 2018.

[15] Z. Lai, X. Qu, Y. Liu, D. Guo, J. Ye, Z. Zhan, *et al.*, "Image reconstruction of compressed sensing MRI using graph-based redundant wavelet transform," *Medical Image Analysis,* vol. 27, pp. 93-104, 2016.

[16] K. G. Hollingsworth, "Reducing acquisition time in clinical MRI by data undersampling and compressed sensing reconstruction," *Physics in medicine and biology,* vol. 60, no. 21, p. R297, 2015.

[17] M. Cetin, I. Stojanovic, O. Onhon, K. Varshney, S. Samadi, W. C. Karl, *et al.*, "Sparsity-Driven Synthetic Aperture Radar Imaging: Reconstruction, autofocusing, moving targets, and compressed sensing," *IEEE Signal Processing Magazine,* vol. 31, no. 4, pp. 27-40, 2014.

[18] J. Wang, X. Chen, D. Fang, C. Q. Wu, Z. Yang, and T. Xing, "Transferring compressive-sensing-based device-free localization across target diversity," *IEEE Transactions on Industrial Electronics,* vol. 62, no. 4, pp. 2397-2409, 2015.

[19] D. L. Donoho, "Compressed sensing," *IEEE Transactions on Information Theory,* vol. 52, no. 4, pp. 1289-1306, 2006.

[20] E. J. Candes, J. K. Romberg, and T. Tao, "Stable signal recovery from incomplete and inaccurate measurements," *Communications on pure and applied mathematics,* vol. 59, no. 8, pp. 1207-1223, 2006.

[21] T. T. Cai and L. Wang, "Orthogonal matching pursuit for sparse signal recovery with noise," *IEEE Transactions on Information Theory,* vol. 57, no. 7, pp. 4680-4688, 2011.

[22] L. Applebaum, S. D. Howard, S. Searle, and R. Calderbank, "Chirp sensing codes: Deterministic compressed sensing measurements for fast recovery," *Applied and Computational Harmonic Analysis*, vol. 26, no. 2, pp. 283-290, 2009.

[23] D. L. Donoho and X. Huo, "Uncertainty principles and ideal atomic decomposition," *IEEE Transactions on Information Theory*, vol. 47, no. 7, pp. 2845-2862, 2001.

[24] R. Küng and P. Jung, "Robust nonnegative sparse recovery and 0/1-Bernoulli measurements," in *2016 IEEE Information Theory Workshop (ITW)*, 2016, pp. 260-264.

[25] Z. Zhang, Y. Xu, J. Yang, X. Li, and D. Zhang, "A survey of sparse representation: algorithms and applications," *IEEE Access*, vol. 3, pp. 490-530, 2015.

[26] W. Deng, W. Yin, and Y. Zhang, "Group sparse optimization by alternating direction method," in *SPIE Optical Engineering + Applications*, 2013, p. 15.

[27] D. Needell and J. A. Tropp, "CoSaMP: Iterative signal recovery from incomplete and inaccurate samples," *Applied and Computational Harmonic Analysis*, vol. 26, no. 3, pp. 301-321, 2009.

[28] S. Mallat, *A wavelet tour of signal processing: the sparse way*. 3rd Ed., Academic press, 2008.

[29] R. Rubinstein, A. M. Bruckstein, and M. Elad, "Dictionaries for sparse representation modeling," *Proceedings of the IEEE*, vol. 98, no. 6, pp. 1045-1057, 2010.

[30] X. Chen, Z. Du, J. Li, X. Li, and H. Zhang, "Compressed sensing based on dictionary learning for extracting impulse components," *Signal Processing*, vol. 96, pp. 94-109, 2014.

[31] R. Gribonval, R. Jenatton, and F. Bach, "Sparse and spurious: dictionary learning with noise and outliers," *IEEE Transactions on Information Theory*, vol. 61, no. 11, pp. 6298-6319, 2015.

[32] M. Seibert, J. Wormann, R. Gribonval, and M. Kleinsteuber, "Learning co-sparse analysis operators with separable structures," *Signal Processing, IEEE Transactions on*, vol. 64, no. 1, pp. 120-130, 2016.

[33] M. Aharon, M. Elad, and A. Bruckstein, "K-SVD: An algorithm for designing overcomplete dictionaries for sparse representation," *IEEE Transactions on Signal Processing*, vol. 54, no. 11, pp. 4311-4322, 2006.

[34] R. Rubinstein, M. Zibulevsky, and M. Elad, "Double sparsity: Learning sparse dictionaries for sparse signal approximation," *IEEE Transactions on Signal Processing*, vol. 58, no. 3 PART 2, pp. 1553-1564, 2010.

[35] S. Mukherjee, R. Basu, and C. S. Seelamantula, "ℓ1-K-SVD: A robust dictionary learning algorithm with simultaneous update," *Signal Processing*, vol. 123, pp. 42-52, 2016.

[36] J. Mairal, G. Sapiro, and M. Elad, "Learning multiscale sparse representations for image and video restoration," *Multiscale Modeling and Simulation*, vol. 7, no. 1, pp. 214-241, 2008.

[37] B. Ophir, M. Lustig, and M. Elad, "Multi-scale dictionary learning using wavelets," *IEEE Journal on Selected Topics in Signal Processing*, vol. 5, no. 5, pp. 1014-1024, 2011.

[38] J. Mairal, F. Bach, J. Ponce, and G. Sapiro, "Online dictionary learning for sparse coding," in *Proceedings of the 26th annual international conference on machine learning*, 2009, pp. 689-696.

[39] K. Skretting and K. Engan, "Recursive least squares dictionary learning algorithm," *IEEE Transactions on Signal Processing*, vol. 58, no. 4, pp. 2121-2130, 2010.

[40] H. Zhao, H. Ye, and R. Wang, "The construction of measurement matrices based on block weighing matrix in compressed sensing," *Signal Processing*, vol. 123, pp. 64-74, 2016.

[41] K. Li, "Structured Compressed Sensing Using Deterministic Sequences," *PhD Thesis, Imperial College London,* 2013.

[42] M. F. Duarte and Y. C. Eldar, "Structured Compressed Sensing: From Theory to Applications," *IEEE Transactions on Signal Processing*, vol. 59, no. 9, pp. 4053-4085, 2011.

[43] M.-J. Sun, L.-T. Meng, M. P. Edgar, M. J. Padgett, and N. Radwell, "A Russian Dolls ordering of the Hadamard basis for compressive single-pixel imaging," *Scientific reports*, vol. 7, no. 1, p. 3464, 2017.

[44] R. I. Stantchev, B. Sun, S. M. Hornett, P. A. Hobson, G. M. Gibson, M. J. Padgett, *et al.*, "Noninvasive, near-field terahertz imaging of hidden objects using a single-pixel detector," *Science Advances*, vol. 2, no. 6, p. e1600190, 2016.

[45] M. P. Edgar, G. M. Gibson, R. W. Bowman, B. Sun, N. Radwell, K. J. Mitchell, *et al.*, "Simultaneous real-time visible and infrared video with single-pixel detectors," *Scientific Reports*, vol. 5, p. 10669, 2015.

[46] Y. B. Li, L. L. Li, B. B. Xu, W. Wu, R. Y. Wu, X. Wan, *et al.*, "Transmission-type 2-bit programmable metasurface for single-sensor and single-frequency microwave imaging," *Scientific reports*, vol. 6, p. 23731, 2016.

[47] M. F. Duarte, M. A. Davenport, D. Takbar, J. N. Laska, T. Sun, K. F. Kelly, *et al.*, "Single-pixel imaging via compressive sampling," *IEEE signal processing magazine,* vol. 25, no. 2, pp. 83-91, 2008.

[48] J. Hunt, T. Driscoll, A. Mrozack, G. Lipworth, M. Reynolds, D. Brady, *et al.*, "Metamaterial apertures for computational imaging," *Science,* vol. 339, no. 6117, pp. 310-3, 2013.

[49] Y. Xie, X. Fan, Y. Chen, J. D. Wilson, R. N. Simons, and J. Q. Xiao, "A subwavelength resolution microwave/6.3 GHz camera based on a metamaterial absorber," *Scientific Reports,* vol. 7, p. 40490, 2017.

[50] D. Rontani, D. Choi, C. Y. Chang, A. Locquet, and D. S. Citrin, "Compressive Sensing with Optical Chaos," *Scientific Reports,* vol. 6, p. 35206, 2016.

[51] C. L. Holloway, E. F. Kuester, J. A. Gordon, J. O. Hara, J. Booth, and D. R. Smith, "An Overview of the Theory and Applications of Metasurfaces: The Two-Dimensional Equivalents of Metamaterials," *IEEE Antennas and Propagation Magazine,* vol. 54, no. 2, pp. 10-35, 2012.

[52] C. Hou-Tong, J. T. Antoinette, and Y. Nanfang, "A review of metasurfaces: physics and applications," *Reports on Progress in Physics,* vol. 79, no. 7, p. 076401, 2016.

[53] S. Walia, C. M. Shah, P. Gutruf, H. Nili, D. R. Chowdhury, W. Withayachumnankul, *et al.*, "Flexible metasurfaces and metamaterials: A review of materials and fabrication processes at micro- and nano-scales," *Applied Physics Reviews,* vol. 2, no. 1, p. 011303, 2015.

[54] S. B. Glybovski, S. A. Tretyakov, P. A. Belov, Y. S. Kivshar, and C. R. Simovski, "Metasurfaces: From microwaves to visible," *Physics Reports,* vol. 634, pp. 1-72, 2016.

[55] L. Xu, C. A. Curwen, D. Chen, J. L. Reno, T. Itoh, and B. S. Williams, "Terahertz Metasurface Quantum-Cascade VECSELs: Theory and Performance," *IEEE Journal of Selected Topics in Quantum Electronics,* vol. 23, no. 6, pp. 1-12, 2017.

[56] D. Wang, L. Zhang, Y. Gong, L. Jian, T. Venkatesan, C. Qiu, *et al.*, "Multiband Switchable Terahertz Quarter-Wave Plates via Phase-Change Metasurfaces," *IEEE Photonics Journal,* vol. 8, no. 1, pp. 1-8, 2016.

[57] M. Chen, H. Jiang, H. Zhang, D. Li, and Y. Wang, "Design of an acoustic superlens using single-phase metamaterials with a star-shaped lattice structure," *Scientific Reports,* vol. 8, no. 1, p. 1861, 2018.

[58] Z.-L. Deng and G. Li, "Metasurface optical holography," *Materials Today Physics,* vol. 3, pp. 16-32, 2017.

[59] J. Wen, H. Feng, J. Chen, K. Wang, Y. Lv, Y. Zhong, *et al.*, "Plasmonic Holographic Metasurfaces for Generation of Vector Optical Beams," *IEEE Photonics Journal*, vol. 9, no. 1, pp. 1-8, 2017.

[60] G. Zheng, H. Muhlenbernd, M. Kenney, G. Li, T. Zentgraf, and S. Zhang, "Metasurface holograms reaching 80% efficiency," *Nat Nanotechnol*, vol. 10, no. 4, pp. 308-12, 2015.

[61] R. E. Carrillo, A. B. Ramirez, G. R. Arce, K. E. Barner, and B. M. Sadler, "Robust compressive sensing of sparse signals: a review," *EURASIP Journal on Advances in Signal Processing*, vol. 2016, no. 1, p. 108, 2016.

[62] N. Vaswani and J. Zhan, "Recursive Recovery of Sparse Signal Sequences From Compressive Measurements: A Review," *IEEE Transactions on Signal Processing*, vol. 64, no. 13, pp. 3523-3549, 2016.

[63] A. Massa, P. Rocca, and G. Oliveri, "Compressive Sensing in Electromagnetics - A Review," *IEEE Antennas and Propagation Magazine*, vol. 57, no. 1, pp. 224-238, 2015.

[64] L. F. Polanía and K. E. Barner, "Exploiting Restricted Boltzmann Machines and Deep Belief Networks in Compressed Sensing," *IEEE Transactions on Signal Processing*, vol. 65, no. 17, pp. 4538-4550, 2017.

[65] O. Lorintiu, H. Liebgott, and D. Friboulet, "Compressed Sensing Doppler Ultrasound Reconstruction Using Block Sparse Bayesian Learning," *IEEE Transactions on Medical Imaging*, vol. 35, no. 4, pp. 978-987, 2016.

[66] X. Zhang, S. Wang, and X. Yun, "Bidirectional Active Learning: A Two-Way Exploration Into Unlabeled and Labeled Data Set," *IEEE Transactions on Neural Networks and Learning Systems*, vol. 26, no. 12, pp. 3034-3044, 2015.

[67] M. A. Figueiredo, R. D. Nowak, and S. J. Wright, "Gradient projection for sparse reconstruction: Application to compressed sensing and other inverse problems," *Selected Topics in Signal Processing, IEEE Journal of*, vol. 1, no. 4, pp. 586-597, 2007.

[68] S. Kim, K. Koh, M. Lustig, S. Boyd, and D. Gorinevsky, "An Interior-Point Method for Large-Scale L1-Regularized Least Squares," *IEEE Journal of Selected Topics in Signal Processing*, vol. 1, no. 4, pp. 606-617, 2007.

[69] J. Yang and Y. Zhang, "Alternating direction algorithms for L1 problems in compressive sensing.," *SIAM Journal on Scientific Computing*, vol. 33, no. 1, pp. 250-278, 2011.

[70] N. Parikh and S. P. Boyd, "Proximal algorithms," *Foundations and Trends in optimization*, vol. 1, no. 3, pp. 127-239, 2014.

[71] W. Yin, S. Osher, D. Goldfarb, and J. Darbon, "Bregman iterative algorithms for L1-minimization with applications to compressed sensing," *SIAM Journal on Imaging sciences*, vol. 1, no. 1, pp. 143-168, 2008.

[72] J. A. Tropp, "Greed is good: Algorithmic results for sparse approximation," *IEEE Transactions on Information Theory*, vol. 50, no. 10, pp. 2231-2242, 2004.

[73] J. A. Tropp and A. C. Gilbert, "Signal recovery from random measurements via orthogonal matching pursuit," *IEEE Transactions on Information Theory*, vol. 53, no. 12, pp. 4655-4666, 2007.

[74] S. G. Mallat and Z. Zhang, "Matching pursuits with time-frequency dictionaries," *IEEE Transactions on Signal Processing*, vol. 41, no. 12, pp. 3397-3415, 1993.

[75] J. A. Tropp, A. C. Gilbert, and M. J. Strauss, "Algorithms for simultaneous sparse approximation. Part I: Greedy pursuit," *Signal Processing*, vol. 86, no. 3, pp. 572-588, 2006.

[76] S. Foucart, "Hard thresholding pursuit: an algorithm for compressive sensing," *SIAM Journal on Numerical Analysis*, vol. 49, no. 6, pp. 2543-2563, 2011.

[77] W. Dai and O. Milenkovic, "Subspace pursuit for compressive sensing signal reconstruction," *IEEE Transactions on Information Theory*, vol. 55, no. 5, pp. 2230-2249, 2009.

[78] T. Blumensath and M. E. Davies, "Normalized iterative hard thresholding: Guaranteed stability and performance," *IEEE Journal of Selected Topics in Signal Processing*, vol. 4, no. 2, pp. 298-309, 2010.

[79] R. Mendoza-Smith, J. W. Tanner, and F. Wechsung, "A Robust Parallel Algorithm for Combinatorial Compressed Sensing," *IEEE Transactions on Signal Processing*, vol. 66, no. 8, pp. 2167-2177, 2018.

[80] D. Bryant, C. J. Colbourn, D. Horsley, and P. Ó. Catháin, "Compressed Sensing With Combinatorial Designs: Theory and Simulations," *IEEE Transactions on Information Theory*, vol. 63, no. 8, pp. 4850-4859, 2017.

[81] M. Aldridge, L. Baldassini, and O. Johnson, "Group Testing Algorithms: Bounds and Simulations," *IEEE Transactions on Information Theory*, vol. 60, no. 6, pp. 3671-3687, 2014.

[82] P. Schniter, "Belief-propagation-based joint channel estimation and decoding for spectrally efficient communication over unknown sparse channels," *Physical Communication*, vol. 5, no. 2, pp. 91-101, 2012.

[83] D. Baron, S. Sarvotham, and R. G. Baraniuk, "Bayesian compressive sensing via belief propagation," *IEEE Transactions on Signal Processing*, vol. 58, no. 1, pp. 269-280, 2010.

[84] D. Bickson, D. Baron, A. Ihler, H. Avissar, and D. Dolev, "Fault Identification Via Nonparametric Belief Propagation," *IEEE Transactions on Signal Processing*, vol. 59, no. 6, pp. 2602-2613, 2011.

[85] M. Sundin, C. R. Rojas, M. Jansson, and S. Chatterjee, "Relevance Singular Vector Machine for Low-Rank Matrix Reconstruction," *IEEE Transactions on Signal Processing*, vol. 64, no. 20, pp. 5327-5339, 2016.

[86] G. Pilikos and A. C. Faul, "Relevance Vector Machines with Uncertainty Measure for Seismic Bayesian Compressive Sensing and Survey Design," in *2016 15th IEEE International Conference on Machine Learning and Applications (ICMLA)*, 2016, pp. 925-930.

[87] T. Hsu, C. Chiou, J. C. R. Tseng, and G. Hwang, "Development and Evaluation of an Active Learning Support System for Context-Aware Ubiquitous Learning," *IEEE Transactions on Learning Technologies*, vol. 9, no. 1, pp. 37-45, 2016.

[88] S. Chakraborty, V. Balasubramanian, and S. Panchanathan, "Adaptive Batch Mode Active Learning," *IEEE Transactions on Neural Networks and Learning Systems*, vol. 26, no. 8, pp. 1747-1760, 2015.

[89] M. Lustig, D. L. Donoho, J. M. Santos, and J. M. Pauly, "Compressed Sensing MRI," *IEEE Signal Processing Magazine*, vol. 25, no. 2, pp. 72-82, 2008.

[90] T. Moy, L. Huang, W. Rieutort-Louis, C. Wu, P. Cuff, S. Wagner, *et al.*, "An EEG acquisition and biomarker-extraction system using low-noise-amplifier and compressive-sensing circuits based on flexible, thin-film electronics," *IEEE Journal of Solid-State Circuits*, vol. 52, no. 1, pp. 309-321, 2017.

[91] R. Hussein, A. Mohamed, and M. Alghoniemy, "Scalable real-time energy-efficient EEG compression scheme for wireless body area sensor network," *Biomedical Signal Processing and Control*, vol. 19, pp. 122-129, 2015.

[92] M. D. Guay, W. Czaja, M. A. Aronova, and R. D. Leapman, "Compressed Sensing Electron Tomography for Determining Biological Structure," *Scientific Reports*, vol. 6, p. 27614, 2016.

[93] Z. Yang and Y. R. Zheng, "A comparative study of compressed sensing approaches for 3-D synthetic aperture radar image reconstruction," *Digital Signal Processing*, vol. 32, pp. 24-33, 2014.

[94] E. Aguilera, M. Nannini, and A. Reigber, "Multisignal compressed sensing for polarimetric SAR tomography," *IEEE Geoscience and Remote Sensing Letters*, vol. 9, no. 5, pp. 871-875, 2012.

[95] D. Bi, Y. Xie, and Y. R. Zheng, "Synthetic aperture radar imaging using basis selection compressed sensing," *Circuits, Systems, and Signal Processing*, vol. 34, no. 8, pp. 2561-2576, 2015.

[96] M. Becquaert, E. Cristofani, G. Pandey, M. Vandewal, J. Stiens, and N. Deligiannis, "Compressed sensing mm-wave SAR for non-destructive testing applications using side information," in *2016 IEEE Radar Conference (RadarConf)*, 2016, pp. 1-5.

[97] Z. Qin, Y. Liu, Y. Gao, M. Elkashlan, and A. Nallanathan, "Throughput Analysis for Compressive Spectrum Sensing with Wireless Power Transfer," *IEEE Global Communications Conference (GLOBECOM)*, pp. 1-6, 2015.

[98] W. Ding, F. Yang, C. Pan, L. Dai, and J. Song, "Compressive sensing based channel estimation for OFDM systems under long delay channels," *IEEE Transactions on Broadcasting*, vol. 60, no. 2, pp. 313-321, 2014.

[99] P. Cheng, L. Gui, Y. Rui, Y. J. Guo, X. Huang, and W. Zhang, "Compressed sensing based channel estimation for two-way relay networks," *IEEE Wireless Communications Letters*, vol. 1, no. 3, pp. 201-204, 2012.

[100] F. Wen, G. Zhang, and D. Ben, "Estimation of multipath parameters in wireless communications using multi-way compressive sensing," *Journal of Systems Engineering and Electronics*, vol. 26, no. 5, pp. 908-915, 2015.

[101] X. Zhou, Y. Fang, and M. Wang, "Compressed sensing based channel estimation for fast fading OFDM systems," *Journal of Systems Engineering and Electronics*, vol. 21, no. 4, pp. 550-556, 2010.

[102] C. Baohao, C. Qimei, and Y. Fan, "Compressed sensing based channel estimation used in non-sample-spaced multipath channels of OFDM system," *The Journal of China Universities of Posts and Telecommunications*, vol. 22, no. 2, pp. 31-37, 2015.

[103] C. Liu, X. Wu, J. Mao, and X. Liu, "Acoustic emission signal processing for rolling bearing running state assessment using compressive sensing," *Mechanical Systems and Signal Processing*, vol. 91, pp. 395-406, 2017.

[104] Y. K. Esfandabadi, L. D. Marchi, N. Testoni, A. Marzani, and G. Masetti, "Full Wavefield Analysis and Damage Imaging Through Compressive Sensing in Lamb Wave Inspections," *IEEE Transactions on Ultrasonics, Ferroelectrics, and Frequency Control*, vol. 65, no. 2, pp. 269-280, 2018.

[105] A. Perelli, T. D. Ianni, A. Marzani, L. D. Marchi, and G. Masetti, "Model-based compressive sensing for damage localization in lamb wave inspection," *IEEE Transactions on Ultrasonics, Ferroelectrics, and Frequency Control,* vol. 60, no. 10, pp. 2089-2097, 2013.

[106] C. K. H. W. J. R. C. Guehmann, "A Compressed Sensing Feature Extraction Approach for Diagnostics and Prognostics in Electromagnetic Solenoids," *Annual Conference Of The Prognostics And Health Management Society,* 2017.

[107] Y. Wang, J. Xiang, Q. Mo, and S. He, "Compressed sparse time–frequency feature representation via compressive sensing and its applications in fault diagnosis," *Measurement,* vol. 68, pp. 70-81, 2015.

[108] J. Helander, A. Ericsson, M. Gustafsson, T. Martin, D. Sjöberg, and C. Larsson, "Compressive Sensing Techniques for mm-Wave Nondestructive Testing of Composite Panels," *IEEE Transactions on Antennas and Propagation,* vol. 65, no. 10, pp. 5523-5531, 2017.

[109] Z. Du, X. Chen, H. Zhang, and B. Yang, "Compressed-Sensing-Based Periodic Impulsive Feature Detection for Wind Turbine Systems," *IEEE Transactions on Industrial Informatics,* vol. 13, no. 6, pp. 2933-2945, 2017.

[110] D. J. Starling and J. Ranalli, "Compressive sensing for spatial and spectral flame diagnostics," *Scientific Reports,* vol. 8, no. 1, p. 2556, 2018.

[111] G. Tang, W. Hou, H. Wang, G. Luo, and J. Ma, "Compressive Sensing of Roller Bearing Faults via Harmonic Detection from Under-Sampled Vibration Signals," *Sensors (Basel),* vol. 15, no. 10, pp. 25648-62, 2015.

[112] Z. Du, X. Chen, H. Zhang, H. Miao, Y. Guo, and B. Yang, "Feature Identification With Compressive Measurements for Machine Fault Diagnosis," *IEEE Transactions on Instrumentation and Measurement,* vol. 65, no. 5, pp. 977-987, 2016.

[113] J. Sun, C. Yan, and J. Wen, "Intelligent Bearing Fault Diagnosis Method Combining Compressed Data Acquisition and Deep Learning," *IEEE Transactions on Instrumentation and Measurement,* vol. 67, no. 1, pp. 185-195, 2018.

[114] H. O. A. Ahmed, M. L. D. Wong, and A. K. Nandi, "Intelligent condition monitoring method for bearing faults from highly compressed measurements using sparse over-complete features," *Mechanical Systems and Signal Processing,* vol. 99, pp. 459-477, 2018.

[115] H. Shao, H. Jiang, H. Zhang, W. Duan, T. Liang, and S. Wu, "Rolling bearing fault feature learning using improved convolutional deep belief network with compressed sensing," *Mechanical Systems and Signal Processing,* vol. 100, pp. 743-765, 2018.

[116] V. Ganesan, T. Das, N. Rahnavard, and J. L. Kauffman, "Vibration-based monitoring and diagnostics using compressive sensing," *Journal of Sound and Vibration,* vol. 394, pp. 612-630, 2017.

[117] J. Park, M. J. Lee, J. Y. Jeon, H. K. Jung, G. Park, T. Kang, *et al.*, "Compressive Sensing Approaches for Condition Monitoring and Laser-scanning Based Damage Visualization," *Procedia Engineering,* vol. 188, pp. 80-87, 2017.

[118] H. Kajbaf, "Compressive sensing for 3D microwave imaging systems," *PhD Thesis, Missouri University of Sccience and Technology,* 2012.

[119] R. Ma, F. Hu, and Q. Hao, "Active Compressive Sensing via Pyroelectric Infrared Sensor for Human Situation Recognition," *IEEE Transactions on Systems, Man, and Cybernetics: Systems,* vol. 47, no. 12, pp. 3340-3350, 2017.

[120] C. M. Watts, D. Shrekenhamer, J. Montoya, G. Lipworth, J. Hunt, T. Sleasman, *et al.*, "Terahertz compressive imaging with metamaterial spatial light modulators," *Nature Photonics,* vol. 8, no. 8, pp. 605-609, 2014.

[121] J. Winges, L. Cerullo, T. Rylander, T. McKelvey, and M. Viberg, "Compressed Sensing for the Detection and Positioning of Dielectric Objects Inside Metal Enclosures by Means of Microwave Measurements," *IEEE Transactions on Microwave Theory and Techniques,* vol. 66, no. 1, pp. 462-476, 2018.

[122] A. Perelli, T. Di Ianni, A. Marzani, L. De Marchi, and G. Masetti, "Model-based compressive sensing for damage localization in lamb wave inspection," *IEEE transactions on ultrasonics, ferroelectrics, and frequency control,* vol. 60, no. 10, pp. 2089-2097, 2013.

[123] H. Yin, Y. Yan, X. Song, and Y. Yang, "Compressive measurement and feature reconstruction method for autonomous star trackers," *Optics & Laser Technology,* vol. 86, pp. 103-114, 2016.

[124] V. Singhal, A. Majumdar, and R. K. Ward, "Semi-Supervised Deep Blind Compressed Sensing for Analysis and Reconstruction of Biomedical Signals From Compressive Measurements," *IEEE Access,* vol. 6, pp. 545-553, 2018.

[125] G. Oliveri, P. Rocca, and A. Massa, "Reliable diagnosis of large linear arrays—A Bayesian compressive sensing approach," *IEEE Transactions on Antennas and Propagation,* vol. 60, no. 10, pp. 4627-4636, 2012.

[126] M. D. Migliore, "A compressed sensing approach for array diagnosis from a small set of near-field measurements," *IEEE Transactions on Antennas and Propagation*, vol. 59, no. 6, pp. 2127-2133, 2011.

[127] K. Bastani, Z. Kong, W. Huang, and Y. Zhou, "Compressive sensing–based optimal sensor placement and fault diagnosis for multi-station assembly processes," *IIE Transactions*, vol. 48, no. 5, pp. 462-474, 2016.

[128] Z. He, X. Zhao, S. Zhang, T. Ogawa, and M. Haseyama, "Random combination for information extraction in compressed sensing and sparse representation-based pattern recognition," *Neurocomputing*, vol. 145, pp. 160-173, 2014.

[129] F. Yang, G. Sheng, Y. Xu, H. Hou, Y. Qian, and X. Jiang, "Partial discharge pattern recognition of XLPE cables at DC voltage based on the compressed sensing theory," *IEEE Transactions on Dielectrics and Electrical Insulation*, vol. 24, no. 5, pp. 2977-2985, 2017.

[130] L. Ren and W. Lv, "Fault Detection via Sparse Representation for Semiconductor Manufacturing Processes," *IEEE Transactions on Semiconductor Manufacturing*, vol. 27, no. 2, pp. 252-259, 2014.

[131] G. Huang, S. Zhou, T. Chio, and T. Yeo, "Fabrication of a High-Efficiency Waveguide Antenna Array via Direct Metal Laser Sintering," *IEEE Antennas and Wireless Propagation Letters*, vol. 15, pp. 622-625, 2016.

[132] K. Katnam, L. Da Silva, and T. Young, "Bonded repair of composite aircraft structures: A review of scientific challenges and opportunities," *Progress in Aerospace Sciences*, vol. 61, pp. 26-42, 2013.

[133] C. S. Li, C. Vannabouathong, S. Sprague, and M. Bhandari, "The use of Carbon-Fiber-Reinforced (CFR) PEEK material in orthopedic implants: A systematic review," *Clinical medicine insights. Arthritis and musculoskeletal disorders*, vol. 8, p. 33, 2015.

[134] F. Rachidi, M. Rubinstein, J. Montanya, J.-L. Bermudez, R. R. Sola, G. Sola, *et al.*, "A review of current issues in lightning protection of new-generation wind-turbine blades," *IEEE Transactions on Industrial Electronics*, vol. 55, no. 6, pp. 2489-2496, 2008.

[135] S. Agrawal, K. K. Singh, and P. Sarkar, "Impact damage on fibre-reinforced polymer matrix composite–a review," *Journal of Composite Materials*, vol. 48, no. 3, pp. 317-332, 2013.

[136] Y. He, G. Tian, M. Pan, and D. Chen, "Non-destructive testing of low-energy impact in CFRP laminates and interior defects in honeycomb sandwich using scanning pulsed eddy current," *Composites Part B: Engineering*, vol. 59, pp. 196-203, 2014.

[137] L. Cheng, B. Gao, G. Y. Tian, W. L. Woo, and G. Berthiau, "Impact Damage Detection and Identification Using Eddy Current Pulsed Thermography Through Integration of PCA and ICA," *IEEE Sensors Journal,* vol. 14, no. 5, pp. 1655-1663, 2014.

[138] I. Amenabar, A. Mendikute, A. López-Arraiza, M. Lizaranzu, and J. Aurrekoetxea, "Comparison and analysis of non-destructive testing techniques suitable for delamination inspection in wind turbine blades," *Composites Part B: Engineering,* vol. 42, no. 5, pp. 1298-1305, 2011.

[139] J. Lin, F. Gao, Z. Luo, and L. Zeng, "High-resolution Lamb wave inspection in viscoelastic composite laminates," *IEEE Transactions on Industrial Electronics,* vol. 63, no. 11, pp. 6989-6998, 2016.

[140] S. Lu, M. Jiang, Q. Sui, Y. Sai, and L. Jia, "Damage identification system of CFRP using fiber Bragg grating sensors," *Composite Structures,* vol. 125, pp. 400-406, 2015.

[141] M. Muramatsu, Y. Harada, T. Suzuki, and H. Niino, "Infrared stress measurements of thermal damage to laser-processed carbon fiber reinforced plastics," *Composites Part A: Applied Science and Manufacturing,* vol. 68, pp. 242-250, 2015.

[142] Z. Li and Z. Meng, "A Review of the Radio Frequency Non-destructive Testing for Carbon-fibre Composites," *Measurement Science Review,* vol. 16, no. 2, pp. 1-9, 2016.

[143] H. Heuer, M. Schulze, M. Pooch, S. Gäbler, A. Nocke, G. Bardl*, et al.*, "Review on quality assurance along the CFRP value chain – Non-destructive testing of fabrics, preforms and CFRP by HF radio wave techniques," *Composites Part B: Engineering,* vol. 77, pp. 494-501, 2015.

[144] S. Kharkovsky and R. Zoughi, "Microwave and millimeter wave nondestructive testing and evaluation-Overview and recent advances," *IEEE Instrumentation & Measurement Magazine*, vol. 10, no. 2, pp. 26-38, 2007.

[145] S.-H. Yang, K.-B. Kim, H. G. Oh, and J.-S. Kang, "Non-contact detection of impact damage in CFRP composites using millimeter-wave reflection and considering carbon fiber direction," *NDT & E International*, vol. 57, pp. 45-51, 2013.

[146] J. Dong, A. Locquet, N. F. Declercq, and D. S. Citrin, "Polarization-resolved terahertz imaging of intra- and inter-laminar damages in hybrid fiber-reinforced composite laminate subject to low-velocity impact," *Composites Part B: Engineering*, vol. 92, pp. 167-174, 2016.

[147] B. Salski, W. Gwarek, P. Korpas, S. Reszewicz, A. Y. B. Chong, P. Theodorakeas*, et al.*, "Non-destructive testing of carbon-fibre-reinforced polymer materials with a radio-frequency inductive sensor," *Composite Structures*, vol. 122, pp. 104-112, 2015.

[148] S. Yuan, Y. Ren, L. Qiu, and H. Mei, "A Multi-Response-Based Wireless Impact Monitoring Network for Aircraft Composite Structures," *IEEE Transactions on Industrial Electronics,* vol. 63, no. 12, pp. 7712-7722, 2016.

[149] A. Majumdar, R. K. Ward, and T. Aboulnasr, "Compressed sensing based real-time dynamic MRI reconstruction," *IEEE Transactions on Medical Imaging,* vol. 31, no. 12, pp. 2253-2266, 2012.

[150] C. Pal, A. Chakrabarti, and R. Ghosh, "A Brief Survey of Recent Edge-Preserving Smoothing Algorithms on Digital Images," *arXiv preprint arXiv:1503.07297,* 2015.

[151] T. Liang, W. Ren, G. Y. Tian, M. Elradi, and Y. Gao, "Low energy impact damage detection in CFRP using eddy current pulsed thermography," *Composite Structures,* vol. 143, pp. 352-361, 2016.

[152] B. Gao, W. L. Woo, and G. Y. Tian, "Electromagnetic Thermography Nondestructive Evaluation: Physics-based Modeling and Pattern Mining," *Scientific Reports,* vol. 6, p. 25480, 2016.

[153] C.-T. Ng, H. Mohseni, and H.-F. Lam, "Debonding detection in CFRP-retrofitted reinforced concrete structures using nonlinear Rayleigh wave," *Mechanical Systems and Signal Processing,* 2018.

[154] W. Khan, "Image segmentation techniques: A survey," *Journal of Image and Graphics,* vol. 1, no. 4, pp. 166-170, 2013.

[155] J. C. Russ and J. C. Russ, "Automatic discrimination of features in grey‐scale images," *Journal of Microscopy,* vol. 148, no. 3, pp. 263-277, 1987.

[156] R. Sutthaweekul, G. Y. Tian, and M. D. Buhari, "Detection of impact damage and fibre texture on CFRP using open-ended waveguide probe," in *2016 13th International Conference on Electrical Engineering/Electronics, Computer, Telecommunications and Information Technology (ECTI-CON),* 2016, pp. 1-6.

[157] Z. Su, X. Luo, Z. Deng, Y. Liang, and Z. Ji, "Edge-Preserving Texture Suppression Filter Based on Joint Filtering Schemes," *IEEE Transactions on Multimedia,* vol. 15, no. 3, pp. 535-548, 2013.

[158] U. Netzelmann and G. Walle, "Induction thermography as a tool for reliable detection of surface defects in forged components," in *17th World Conference on Nondestructive Testing, Shanghai, China, Oct,* 2008, pp. 25-28.

[159] F. Huang, J. Tao, Y. Xiang, P. Liu, L. Dong, and L. Wang, "Parallel compressive sampling matching pursuit algorithm for compressed sensing signal reconstruction with OpenCL," *Journal of Systems Architecture,* vol. 72, pp. 51-60, 2017.

[160] C. Tang, G. Y. Tian, K. Li, R. Sutthaweekul, and J. Wu, "Smart Compressed Sensing for Online Evaluation of CFRP Structure Integrity," *IEEE Transactions on Industrial Electronics*, vol. 64, no. 12, pp. 9608-9617, 2017.

[161] X. Yang, Y. R. Zheng, M. T. Ghasr, and K. M. Donnell, "Microwave Imaging From Sparse Measurements for Near-Field Synthetic Aperture Radar," *IEEE Transactions on Instrumentation and Measurement*, vol. 66, no. 10, pp. 2680-2692, 2017.

[162] H. Kajbaf, J. T. Case, Z. Yang, and Y. R. Zheng, "Compressed sensing for SAR-based wideband three-dimensional microwave imaging system using non-uniform fast fourier transform," *IET Radar, Sonar & Navigation*, vol. 7, no. 6, pp. 658-670, 2013.

[163] W. Qiu, J. Zhou, H. Zhao, and Q. Fu, "Three-Dimensional Sparse Turntable Microwave Imaging Based on Compressive Sensing," *IEEE Geoscience and Remote Sensing Letters*, vol. 12, no. 4, pp. 826-830, 2015.

[164] M. T. Bevacqua and R. Scapaticci, "A Compressive Sensing Approach for 3D Breast Cancer Microwave Imaging With Magnetic Nanoparticles as Contrast Agent," *IEEE Transactions on Medical Imaging*, vol. 35, no. 2, pp. 665-673, 2016.

[165] S. H. Jung, Y. S. Cho, R. S. Park, J. M. Kim, H. K. Jung, and Y. S. Chung, "High-Resolution Millimeter-Wave Ground-Based SAR Imaging via Compressed Sensing," *IEEE Transactions on Magnetics*, vol. 54, no. 3, pp. 1-10, 2018.

[166] M. N. Stevanović, L. Crocco, A. R. Djordjević, and A. Nehorai, "Higher Order Sparse Microwave Imaging of PEC Scatterers," *IEEE Transactions on Antennas and Propagation*, vol. 64, no. 3, pp. 988-997, 2016.

[167] Z. Du, X. Chen, H. Zhang, R. Yan, and W. Yin, "Learning Collaborative Sparsity Structure via Nonconvex Optimization for Feature Recognition," *IEEE Transactions on Industrial Informatics*, vol. 14, no. 10, pp. 4417-4430, 2017.

[168] L. Wan, G. Han, L. Shu, S. Chan, and N. Feng, "PD Source Diagnosis and Localization in Industrial High-Voltage Insulation System via Multimodal Joint Sparse Representation," *IEEE Transactions on Industrial Electronics*, vol. 63, no. 4, pp. 2506-2516, 2016.

[169] S. Shekhar, V. M. Patel, N. M. Nasrabadi, and R. Chellappa, "Joint Sparse Representation for Robust Multimodal Biometrics Recognition," *IEEE Transactions on Pattern Analysis and Machine Intelligence*, vol. 36, no. 1, pp. 113-126, 2014.

[170] D. Bi, Y. Xie, L. Ma, X. Li, X. Yang, and Y. R. Zheng, "Multifrequency Compressed Sensing for 2-D Near-Field Synthetic Aperture Radar Image Reconstruction," *IEEE Transactions on Instrumentation and Measurement*, vol. 66, no. 4, pp. 777-791, 2017.

[171] G. Xia, H. Sun, X. Niu, G. Zhang, and L. Feng, "Keyframe Extraction for Human Motion Capture Data Based on Joint Kernel Sparse Representation," *IEEE Transactions on Industrial Electronics,* vol. 64, no. 2, pp. 1589-1599, 2017.

[172] X. Zhang, G. Liao, S. Zhu, D. Yang, and W. Du, "Efficient Compressed Sensing Method for Moving-Target Imaging by Exploiting the Geometry Information of the Defocused Results," *IEEE Geoscience and Remote Sensing Letters,* vol. 12, no. 3, pp. 517-521, 2015.

[173] B. H. Chen, S. C. Huang, and S. Y. Kuo, "Error-Optimized Sparse Representation for Single Image Rain Removal," *IEEE Transactions on Industrial Electronics,* vol. 64, no. 8, pp. 6573-6581, 2017.

[174] E. Huang, Q. Ma, and Z. Liu, "Ultrafast Imaging using Spectral Resonance Modulation," *Scientific Reports,* vol. 6, p. 25240, 2016.

[175] C. Yang, C. Peng, Y. Chen, T. Luo, and J. Chu, "Space-filling scan paths and Gaussian process-aided adaptive sampling for efficient surface measurements," *Precision Engineering,* vol. 54, pp. 412-419, 2018.

[176] A. Kulkarni and T. Mohsenin, "Low Overhead Architectures for OMP Compressive Sensing Reconstruction Algorithm," *IEEE Transactions on Circuits and Systems I: Regular Papers,* vol. 64, no. 6, pp. 1468-1480, 2017.

[177] C. Gu, J. Zhao, W. Xu, and D. Sun, "Design of Linear-Phase Notch Filters Based on the OMP Scheme and the Chebyshev Window," *IEEE Transactions on Circuits and Systems II: Express Briefs,* vol. 59, no. 9, pp. 592-596, 2012.

[178] E. Liu and V. N. Temlyakov, "The orthogonal super greedy algorithm and applications in compressed sensing," *IEEE Transactions on Information Theory,* vol. 58, no. 4, p. 2040, 2012.

[179] D. L. Donoho, Y. Tsaig, I. Drori, and J.-L. Starck, "Sparse solution of underdetermined systems of linear equations by stagewise orthogonal matching pursuit," *IEEE Transactions on Information Theory,* vol. 58, no. 2, pp. 1094-1121, 2012.

[180] J. Wang, S. Kwon, and B. Shim, "Generalized orthogonal matching pursuit," *IEEE Transactions on signal processing,* vol. 60, no. 12, p. 6202, 2012.

[181] M. A. Davenport, D. Needell, and M. B. Wakin, "Signal space CoSaMP for sparse recovery with redundant dictionaries," *IEEE Transactions on Information Theory,* vol. 59, no. 10, pp. 6820-6829, 2013.

[182] Q. Wan, H. Duan, J. Fang, H. Li, and Z. Xing, "Robust bayesian compressed sensing with outliers," *Signal Processing,* vol. 140, pp. 104-109, 2017.

[183] J. Pan, J. Tang, L. Wang, and Y. Zhang, "Improved sparse signal recovery method based on matching pursuit revised MAP estimation," *Electronics Letters,* vol. 54, no. 15, pp. 953-955, 2018.

[184] M. Masood and T. Y. Al-Naffouri, "Sparse Reconstruction Using Distribution Agnostic Bayesian Matching Pursuit," *IEEE Transactions on Signal Processing,* vol. 61, no. 21, pp. 5298-5309, 2013.

[185] M. Hong and A. Garcia, "Averaged Iterative Water-Filling Algorithm: Robustness and Convergence," *IEEE Transactions on Signal Processing,* vol. 59, no. 5, pp. 2448-2454, 2011.

[186] C. Cho and S. Lee, "Effective Five Directional Partial Derivatives-Based Image Smoothing and a Parallel Structure Design," *IEEE Transactions on Image Processing,* vol. 25, no. 4, pp. 1617-1625, 2016.

[187] M. Slawski and P. Li, "On the Trade-Off Between Bit Depth and Number of Samples for a Basic Approach to Structured Signal Recovery From b-Bit Quantized Linear Measurements," *IEEE Transactions on Information Theory,* vol. 64, no. 6, pp. 4159-4178, 2018.

[188] Y. Plan and R. Vershynin, "Robust 1-bit Compressed Sensing and Sparse Logistic Regression: A Convex Programming Approach," *IEEE Transactions on Information Theory,* vol. 59, no. 1, pp. 482-494, 2013.

[189] K. Knudson, R. Saab, and R. Ward, "One-Bit Compressive Sensing With Norm Estimation," *IEEE Transactions on Information Theory,* vol. 62, no. 5, pp. 2748-2758, 2016.

[190] D. Schurig, J. J. Mock, and D. R. Smith, "Electric-field-coupled resonators for negative permittivity metamaterials," *Applied Physics Letters,* vol. 88, no. 4, p. 041109, 2006.

[191] A. Zhao, G. Y. Tian, and J. Zhang, "IQ signal based RFID sensors for defect detection and characterisation," *Sensors and Actuators A: Physical,* vol. 269, no. Supplement C, pp. 14-21, 2018.

[192] A. Zhao, J. Zhang, and G. Y. Tian, "Miniaturization of UHF RFID Tag Antenna Sensors for Corrosion Characterization," *IEEE Sensors Journal,* vol. 17, no. 23, pp. 7908-7916, 2017.

[193] H.-J. Chae, M. Salajegheh, D. J. Yeager, J. R. Smith, and K. Fu, "Maximalist cryptography and computation on the WISP UHF RFID tag," in *Wirelessly Powered Sensor Networks and Computational RFID,* ed: Springer, 2013, pp. 175-187.

[194] A. M. J. Marindra and G. Y. Tian, "Chipless RFID Sensor Tag for Metal Crack Detection and Characterization," *IEEE Transactions on Microwave Theory and Techniques*, vol. 66, no. 5, pp. 2452-2462, 2018.